UCLA
UCLA Electronic Theses and Dissertations

Title

In situ TEM Nanomechanical Testing of Ceramics: Room-Temperature Plastic Deformation Mechanisms

Permalink

https://escholarship.org/uc/item/4bb1w1bj

Author

Kiani, Sara

Publication Date

2014

Peer reviewed|Thesis/dissertation

Université of California

Los Angeles

In Situ TEM Nanomechanical Testing of Ceramics: Room-Temperature Plastic Deformation Mechanisms

A dissertation submitted in partial satisfaction

of the requirements for the degree

Doctor of Philosophy in Materials Science and Engineering

by

Sara Kiani

2014

ABSTRACT OF THE DISSERTATION

In Situ TEM Nanomechanical Testing of Ceramics: Room-Temperature Plastic Deformation Mechanisms

by

Sara Kiani

Doctor of Philosophy in Materials Science and Engineering

University of California, Los Angeles, 2014

Professor Jenn-Ming Yang, Chair

This dissertation presents the investigation of the effects of size-scale and crystallographic orientation on room-temperature plastic deformation of ceramics. Using *in situ* electron microscopy based nanomechanical testing, I show that sub-micron-scale single-crystalline refractory carbides exhibit size- and orientation-dependent room-temperature plasticity under uniaxial compression. Refractory carbides such as ZrC, TaC and SiC – chosen as candidate materials – owing to their high hardness ($\geq$ 20 Gpa), high elastic modulus ($\geq$ 350 GPa) and melting point ($\geq$ 3000 K), are widely used in various high temperature/high hardness structural applications. Most of the previous studies conducted on these materials are on bulk samples at temperatures $\geq$ 0.3 T_m. While these studies have helped understand the thermomechanical behavior, relatively little is known concerning their room-temperature mechanical properties. Here, I investigated simultaneous morphological and microstructural changes during mechanical deformation of sub-micron-size cylindrical pillars, identified slip systems and measured yield strength as a function of crystal size. I show that for ZrC pillars, loading along [100] and [111] directions activate $\{1\bar{1}0\}\langle110\rangle$ and $\{001\}\langle110\rangle$ slip systems, respectively. For both the orientations, yield strengths increase with decreasing crystal size. Unexpectedly, ZrC(111) is found to be up to 10$\times$ softer than ZrC(100). For TaC pillars, loading along [100] and [011] directions activate $\{1\bar{1}0\}\langle110\rangle$ and $\{1\bar{1}1\}\langle110\rangle$ slip systems. In contrast to ZrC, I did not observe any size effects on yield strength. In the case of 6H-

SiC, loading along the basal direction $\langle 0001 \rangle$ results in brittle fracture, while loading at 45°
with respect to $\langle 0001 \rangle$ leads to dislocation glide-controlled plasticity at room-temperature.
Molecular dynamics simulations and density functional theory calculations helped in identi-
fication of the most energetically favorable slip systems and the mechanisms governing the
plastic deformation. My results provide important insights into room-temperature plastic
deformation modes operating in refractory carbides.

The dissertation of Sara Kiani is approved.

Abby Kavner

Suneel Kodambaka

Jenn-Ming Yang, Committee Chair

University of California, Los Angeles

2014

This dissertation is dedicated to my loving family

Grandma, Mom, Dad, Samira, Amirreza

Table of Contents

List of Figures

xiii

List of Tables

ACKNOWLEDGMENTS

I would like to take this opportunity to thank many people who helped me along my journey at UCLA and at the Lawrence Berkeley National Laboratory.

First of all, I would like to thank my advisors, Prof. Jenn-Ming Yang and Prof. Suneel Kodambaka for their valuable guidance and support throughout this project; patiently helping me learn and shape into a better scientist. I would also like to acknowledge my committee members, Prof. Abby Kavner and Prof. Richard Kaner for their advices. This project was not possible without the funding from the AFOSR (Dr. Ali Sayir) under Grant # FA9550-10-1-0496. We are thankful for providing us with this research opportunity.

There are certain individuals who gave me great assistance on this research. First, I would like to show my deepest appreciation to Prof. Andrew Minor for accepting me in his research group in Berkeley and giving me the opportunity to conduct my research at the Lawrence Berkeley National Laboratory, Center for Electron Microscope (NCEM) from September 2011 – June 2014. It was a great honor to learn from brilliant scientists at this most prestigious center and get exposed to the leading edge research in the field of electron microscope. During my stay at NCEM, I used a lot of help from Mrs. Marissa Manusco in sample preparation, Mr. John Turner with issues related to SEM/FIB, Mr. Chengyu Song and Dr. Karen Bustillo with TEM related questions. I also got a chance to work with Dr. Burak Ozdul, Dr. Christian Liebscher, Dr. Christoph Gammer, Dr. Hua Gua, Dr. Qian Yu, Dr. Eita Tochigi and Dr. Colin Ophus who kindly helped me with all my questions. For this, I am very thankful to all of them. I also appreciate the help of Dr. Christian Ratsch from Institute for Pure and Applied Mathematics at UCLA, graduate student Mr. Kai Wing Kelvin Leung and Prof. Derek Warner from the School of Civil and Environmental Engineering at Cornel University with DFT calculations and MD simulations as part of the collaboration in this research.

Many thanks goes to my sister Samira Kiani, my brother Amirreza Kiani and my aunt Farnia Amirnia whom their everlasting love and care will always bring warmth to my heart and encouragement in my life. Finally, I wish to dedicate this dissertation to my parents,

1997 – 2001	B.S. (Materials Science and Engineering), Sharif University of Technology, Tehran, Iran.
2003 – 2005	M.S. (Materials Science and Engineering), The University of Texas at Arlington, Texas, United States.
2005 – 2008	Research Engineer , Kennametal Inc., Arkansas, United States.

Publications

S. Kiani, C. Ratsch, A. Minor, S. Kodambaka, and J-M. Yang,"Orientation- and Size-Dependent Room-Temperature Plasticity in ZrC Single Crystals"- Under Review

S. Kiani, K. W. K. Leung, V. Radmilovic, A. M. Minor, J-M. Yang, D.H. Warner, S. Kodambaka,"Dislocation Glide-Controlled Room-Temperature Plasticity in Nano- Scale 6H-SiC Single Crystals"- In preparation

S. Kiani, A. M. Minor, S. Kodambaka and J-M. Yang,"Dislocation Glide-Controlled Room-Temperature Plasticity in Sub-Micron Scale SiC Single Crystals," *TMS 143th Annual Meeting and Exhibition*, San Diego, CA, February, 2014

S. Kiani, A. M. Minor, S. Kodambaka and J-M. Yang,"In Situ Transmission Electron Microscopy Studies of Size-Dependent Plasticity in Ceramic Materials," *TMS 142th Annual Meeting and Exhibition*, San Antonio, TX, March, 2013

S. Kiani, A. Minor, S. Kodambaka, and J-M. Yang,"Insights from In Situ TEM Compression Test of Ceramics," *Gordon Research Conference, Solid State Studies in Ceramics*, Mount Holyoke College, MA, August, 2012.

S. Kiani, A. Minor, S. Kodambaka, and J-M. Yang,"Size Dependence of Mechanical Properties of Refractory Carbides," *TMS 141th Annual Meeting and Exhibition*, Orlando, FL, March, 2012.

S. Kiani, S. Kodambaka, and J-M. Yang,"Influence of Size on Compression Strength of SiC and ZrC Micro and Nano Pillars," *UCLA Engineering Tech Forum*, Los Angeles, CA, March, 2012.

S. Kiani, S. Kodambaka, and J-M. Yang,"Investigation of Compression Strengths of SiC(0001) and ZrC(001) Micropillars," *36th International Conference and Exposition on Advanced Ceramics and Composites*, Daytona Beach, FL, January, 2012.

S. Kiani, S. Kodambaka, and J-M. Yang, "Influence of Size on Compression Strengths of Refractory Carbides", *2nd Annual AFOSR Hypersonics Center Review*, Dayton, OH, August, 2011.

CHAPTER 1

Introduction

1.1 Overview

With the shift towards miniaturization of electronic, MEMS and NEMS devices, the demand for the development of materials at micron and sub-micron length scales with improved mechanical properties increased. Small-scale testing and investigation of the effects of size and crystal orientation on the strength and plasticity of materials received renewed attention since 2004 due to various *ex situ* and *in situ* microscopy testing techniques. However, relatively few studies to date have investigated small-scale mechanical behavior of refractory carbides, borides and nitrides. Although these materials are generally considered to be brittle at room-temperature, reducing the size can shift the behavior from brittle to ductile with enhanced plasticity [1].

Group IV and V transition metal carbides, borides and nitrides (for example, ZrC, TaC, HaC, VC, ZrB_2, TiN), along with SiC and Si_3N_4 commonly referred to as ultra high temperature ceramics (UHTCs), owing to their high melting point, high strength, good oxidation resistance and chemical stability are suitable candidates for various advanced structural and aerospace applications [2, 3].

Realization of room-temperature plasticity in transition metal- carbides and other refractory ceramics would lead to greater improvements in life-time performance of these structural materials at lower temperatures. It could also potentially open up new applications and the possibility of designing hard-yet-ductile ceramic nanocomposites, free-standing thin films, and nanostructures for a variety of structural applications.

Here I focus on three monolithic single-crystalline carbides, ZrC, TaC and 6H-SiC (α-

SiC) and investigate the effects of size and crystallographic orientation on room-temperature compression behavior of sub-micron-scale pillars and the deformation mechanisms inside a transmission electron microscope (TEM). Such *in situ* TEM experiments provide dynamic information through simultaneous observation of morphological and structural changes and correlation to the mechanical response. This study provides a unique insight into intrinsic mechanical behavior of nano-scale ceramics.

1.2 Research Objectives

UHTCs are a family of materials with some of the highest melting points, high hardness, and good chemical stability due to formation of stable oxides. Figure 1.1 compares various candidates as UHTCs based on their melting points. Among this family, group IV and V transition metal- carbides, borides and nitrides (e.x. ZrC, HfC, ZrB_2, VC, TiN) as well as silicon based refractory compounds (e.x. SiC, Si_3N_4) are considered as great candidates for various structural, defense and aerospace applications [4]. They are promising for airframe leading edges and reentry vehicles mainly due to their ultra-high melting temperatures up to $\sim 4000°C$, their excellent high temperature strength, and oxidation resistance [5,6]. As an example, ZrB_2 and HfB_2 are found to be attractive for ultra-high temperature aerospace applications because of their thermomechanical and chemical properties which can be tailored by alloying with other transition metal borides as well as other refractory ceramics [7].

Mechanical response of many bulk UHTCs has been investigated at temperatures $\geq$ 1000 °C, like tensile testing of SiC-SiC composite coupled with micro-CT scan at 1750 °C to monitor any microcrack formation [8], or compressive loading of TaC at temperatures above 1200 °C [9]. Generally these materials show plasticity at T $\geq$ 0.3 T_m and are considered to be brittle at room-temperature. Although UHTCs have a high hardness (> 20 GPa), their low fracture toughness has always been a non-desired property. Many methods including addition of SiC [10–12] or carbon nanotubes [13–15] to for example ZrB_2 are investigated to improve the toughness leading to "hard-yet-tough" ceramics.
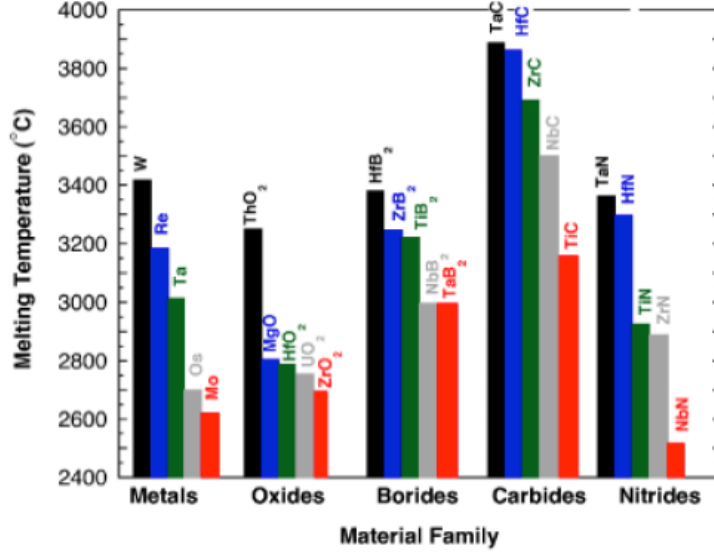
Figure 1.1: Comparison of melting points of transition metal-carbides, borides and nitrides [7]

There is considerable literature on synthesis, processing, mechanical properties, high-temperature oxidation and related changes in morphology and microstructure of bulk UHTC composite materials [16–18]. What is lacking is a detailed understanding of the processes controlling materials behavior at small size-scales essential for developing materials with significantly better properties.

Hence, in this dissertation I focus on understanding the room-temperature behavior of three single-crystalline monolithic carbide; ZrC, TaC and SiC. ZrC and TaC have rocksalt (B1) NaCl crystal structure while, 6H-SiC has a wurtzite crystal structure. All three are important candidates for high temperature/high hardness applications. To simplify the fundamental understanding of the behavior of these materials at small size-scales, single-crystalline samples are first investigated. Similar studies on poly-crystalline materials or composite of such materials are proposed in the future work and are out of the scope of this research. Sub-micron pillars are prepared via Focused Ion Beam (FIB) technique in the size range of 100 nm – 500 nm from a bulk sample with a known crystallographic orientation. Uniaxial compression test is carried out at room-temperature inside a transmission electron microscope (TEM) to simultaneously observe any morphology change and relate it to the mechanical response. Since most refractory ceramics are anisotropic, it is expected that

3

deformation behavior and mechanical properties to vary with crystallographic orientation. Uniaxial compression test results and analysis on deformation mechanism and slip systems on sub-micron pillars (500 nm and below) are presented in Chapter 4 for ZrC, in Chapter 5 for 6H-SiC (α-SiC) and in Chapter 6 for TaC. ZrC(100) *vs.* ZrC(111) nanopillars exhibit strong size-scale and crystallographic orientation dependence of yield stress with plastic deformation mechanism of shear deformation *vs.* dislocation tangling respectively. Size-scale dependence of yield stress is less pronounced in TaC(100) *vs.* TaC(011) nanopillars where shear deformation is the dominant mode of plastic deformation. For 6H-SiC, basal slip and dislocation movement is shown to be dominant when the pillars are loaded along 45° with respect to $\langle 0001 \rangle$; the basal plane normal. While, loading parallel to basal plane normal $\langle 0001 \rangle$ leads to brittle fracture since the "easy" basal plane sliding is suppressed and non-basal slip are not operative.

CHAPTER 2

Literature Survey

2.1 Overview

Most of the current knowledge on dislocation-mediated plasticity in transition metal- carbides and refractory compounds is limited to the high temperature data ($T \geq 0.3\ T_m$). It is shown that decreasing the size, besides increasing temperature, will enhance plasticity in brittle materials [1]. An understanding of strength and plasticity of these materials at small-scales at low temperature is essential for new material development. But before presenting the new findings in this study, an overview of the properties, slip modes and plastic deformation of ZrC, SiC and TaC plus some of the existing literatures on mechanical testing (mainly compression) of micron and sub-micron metallic and non-metallic specimens are presented. Understanding the existing literature is helpful in better interpreting the behavior observed in single-crystalline sub-micron pillars of ZrC, SiC and TaC.

2.2 Material Properties, Slip Modes and Plastic Deformation

2.2.1 Physical and Mechanical Properties of Zirconium Carbide

Zirconium carbide (ZrC) is a group IV transition-metal carbide with a mixture of covalent, ionic and metallic bonds. It has excellent resistance to wear, abrasion, corrosion, and thermal shock with good electrical and thermal conductivities. It is considered among ultra high temperature ceramics (UHTCs) as a candidate for space vehicles and in hypersonic flights. ZrC has a rocksalt (B1) NaCl crystal structure that can be seen as one FCC structure with secondary atoms in octahedral positions. ZrC's high hardness (> 20 GPa), high-modulus

(Young's moduli > 350 GPa), and high-melting ($T_m \geq 3000$ K) point makes it an attractive candidate for aerospace as well as wear/ hard coating applications. Some of the physical and mechanical properties of ZrC are listed in Table 2.1.

Table 2.1: Physical and mechanical properties of zirconium carbide [19]

Density (g/cm^3)	Poisson's ratio (ave.)	Melting point (°C)	Hardness (GPa)	Elastic Modulus (GPa)	Toughness (MPa.m$^{1/2}$)
6.6	0.191	3540	25.5	$350 - 440$	~ 3

2.2.2 Physical and Mechanical Properties of Silicon Carbide

Silicon carbide (SiC) a compound of silicon and carbon has over 200 polytypes caused by a one-dimensional disorder allowing different stacking sequences. Among these polytypes, 3C-SiC has the cubic symmetry (β-SiC) and the others have either hexagonal or rhombohedral structure (α-SiC). Figure 2.1 depicts the crystal structure of common polytypes of SiC. 6H-SiC (a polytype of α-SiC) with wurtzite crystal structure and predominantly covalent
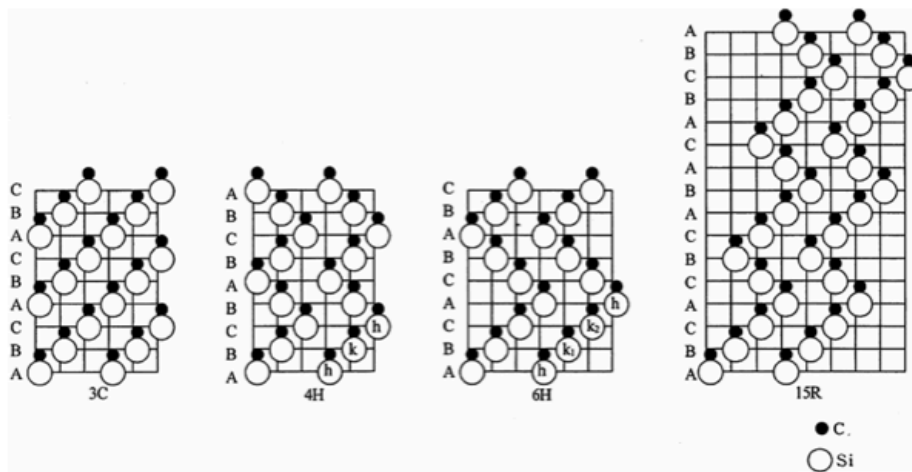
Figure 2.1: Crystal structure of 3C, 4H, 6H and 15R SiC from left to right [20].

bonding is a hard (> 25 GPa) solid with high melting point ($T_m \sim 3000$ K) and high modulus (Young's moduli > 415 GPa) used as wear parts, as reinforcement in metal-matrix

6

composites, in body armor, and as structural components in hypersonic flights. Some of the physical and mechanical properties of 6H-SiC are listed in Table 2.2.

Table 2.2: Physical and mechanical properties of 6H-SiC [19, 21]

Density (g/cm^3)	Poisson's ratio (ave.)	Melting point (°C)	Hardness (GPa)	Elastic Modulus (GPa)	Toughness (MPa.m$^{1/2}$)
3.2	0.142	2450	24.5 − 28.2	475	3.3

As a structural ceramic, both high strength and ductility are desired. Strength is the resistance of the material to failure, while ductility is mostly related to dislocation activity. Oxidation resistance, chemical stability and excelled thermal shock resistance are among the desired properties of these refractory carbides for application in high temperature/high strength fields. SiC is also among the ultra high temperature ceramics (UHTCs) with mostly covalent bonding, unlike metals, exhibit different high-temperature properties. For example, SiC exhibits a good oxidation resistance at temperatures up to $\sim$ 1600 °C due to the formation of a protective SiO_2 scale; and combust at very high oxygen pressures depending on composition, nature of the bonding, and oxygen solubility [22]. It is also shown that the addition of SiC to ZrB_2 and HfB_2 improves the mechanical strength and enhances the oxidation resistance [23, 24].

2.2.3   Physical and Mechanical Properties of Tantalum Carbide

Tantalum carbide (TaC) is a group V transition-metal carbide with a mixture of covalent, ionic and metallic bonds. TaC is the most metallic of the IV and V transition metal mono-carbides with rocksalt (B1) NaCl crystal structure. Its exceptionally high melting point (T_m > 4000 K), high hardness (between 11 to 26 GPa), wear resistance, and high modulus (Young's moduli $\sim$ 537 GPa), good chemical stability, and oxidation resistance suggest that this material could be a suitable candidate in tool steels, wear-resistant parts, diffusion barriers, hard coatings, conducting films, oxidation-resistant coatings, optical coatings, and as a structural ceramics in high-temperature applications such as hypersonic vehicles (leading edges and nose-caps) [25–28]. Some of the physical and mechanical properties of TaC are

summarized in Table 2.3.

Table 2.3: Physical and mechanical properties of TaC [19]

Density (g/cm^3)	Poisson's ratio (ave.)	Melting point (°C)	Hardness (GPa)	Elastic Modulus (GPa)	Toughness (MPa.m$^{1/2}$)
14.5	0.24	3950	16.7	$285 - 560$	12.7

2.2.4 Crystal Structure

ZrC has face centered bravias lattice with space group of Fm3m and space group number 225. It is considered cubic, $\alpha = \beta = \gamma = 90°$ with lattice parameter a = 0.4695 nm. There are total of 8 atoms (4 carbon and 4 zirconium) per unit cell at $C(0,0,0)$ and $Zr(1/2, 1/2, 1/2)$ positions. Like other ionic solids, ZrC can be seen as a closed packed arrangements of zirconium atoms with carbon atoms occupying the octahedral sites. It has a stacking sequence of ABCABC with $\langle 110 \rangle$ being the closed-packed direction (shortest repeat distance). Figure 2.2 shows a 3-D image of ZrC unit cell drawn using CrystalMaker 8.5 data visualization program knowing the space group, and lattice parameter.
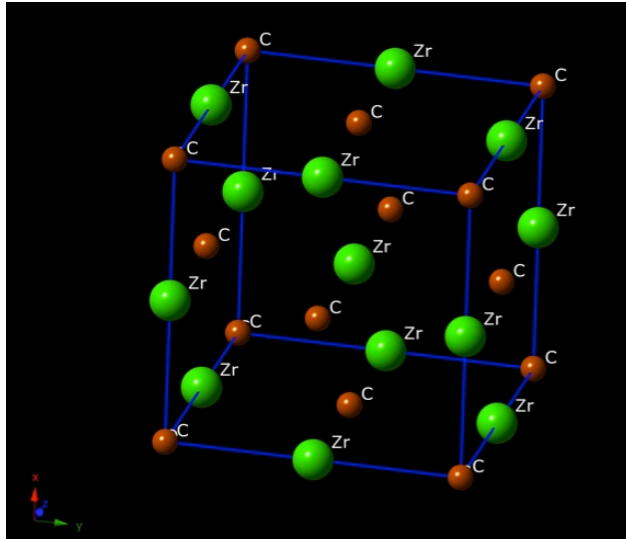
Figure 2.2: 3-D image of ZrC unit cell with space group number 225 and lattice parameter a = 0.4695 nm

On the other hand, 6H-SiC has a wurtzite crystal structure – a member of hexagonal crystal system – with space group of P6₃mc and space group number 186. Since it is considered hexagonal, $\alpha = \beta = 90°$ and $\gamma = 120°$ with lattice constants a = 0.3073 nm and c = 1.511 nm. There are total of 12 atoms (6 carbon and 6 silicon) per unit cell at Si(0,0,0), Si(1/3,2/3,1/6), Si(1/3,2/3,5/6) and C atoms at C→Si +(0,0,1/8) positions. It has a stacking sequence of ABCACB with $\langle 2\overline{1}\overline{1}0 \rangle$ being the closed-packed direction (shortest repeat distance). Each of the two atom types (Si and C) form a sublattice which is "hexagonal close-pack" (HCP). When viewed altogether, each atom is tetrahedrally coordinated (hexagonal diamond). Figure 2.3 depicts wurtzite crystal structure and unit cell.
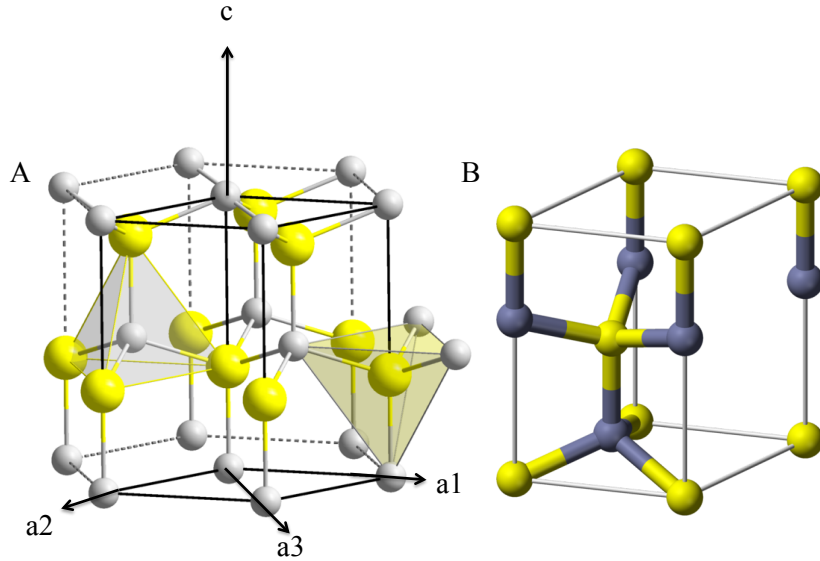
Figure 2.3: A) Wurtzite crystal structure and B) wurtzite unit cell [29]

Despite a more common three-axis Miller indices i.e., (hkl) for planes and (UVW) for direction used for cubic structures, to index the hexagonal structure a four-axis Miller indices is used that is based on vectors a1, a2, a3 and c. In hexagonal system, Miller indices for planes (reciprocal of plane intersects with axes) is represented as (hkil) where i = − (h+k). Direction is expressed as d = ua1 + va2 + ta3 + wc where t = − (u+v). Conversion of (UVW) in three- axis Miller system (cubic) to four-axis Miller system (hexagonal) is u = 1/3 (2U−V), v = 1/3(2V−U), w = W and t = −(u+v). Despite the cubic structure, plane and the corresponding direction normal do not have the same Miller indices. The conversion of

plane (hkil) to the corresponding direction normal is [uvtw] =(hki3/2(c/a)^{2}l) in hexagonal structure. Figure 2.4 shows a 3-D image of 6H-SiC unit cell drawn using CrystalMaker 8.5 data visualization program knowing the space group, and lattice parameter.
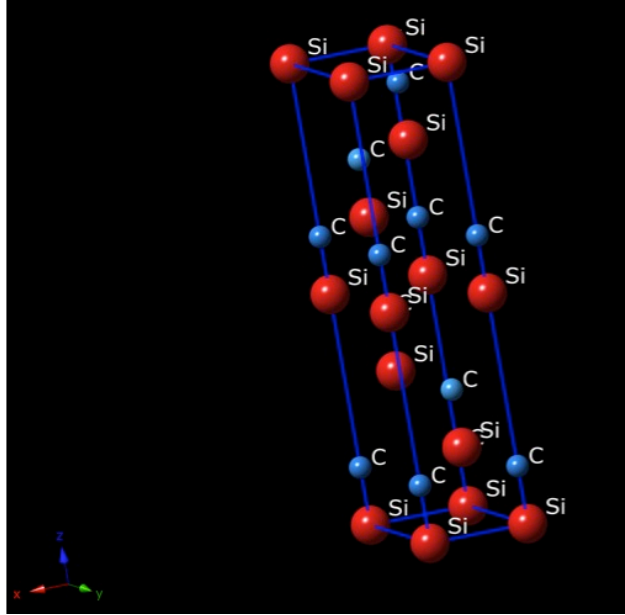
Figure 2.4: 3-D image of 6H-SiC unit cell with space group number 186 and lattice parameters a = 0.3073 nm and c = 1.511 nm

When it comes to TaC, there are a lot of similarities with ZrC. It has face centered bravias lattice with space group of Fm3m and space group number 225. It is considered cubic $\alpha = \beta = \gamma = 90°$ with lattice parameter a = 0.4454 nm. There are total of 8 atoms (4 carbon and 4 zirconium) per unit cell at $C(0,0,0)$ and $Ta(1/2,1/2,1/2)$ positions. Like other ionic solids, TaC can be treated as a closed packed arrangements of tantalum atoms with carbon atoms occupying the octahedral sites. It has a stacking sequence of ABCABC with $\langle 110 \rangle$ being the closed-packed direction (shortest repeat distance). Figure 2.5 shows a 3-D image of TaC unit cell drawn using CrystalMaker 8.5 data visualization program knowing the space group, and lattice parameter.
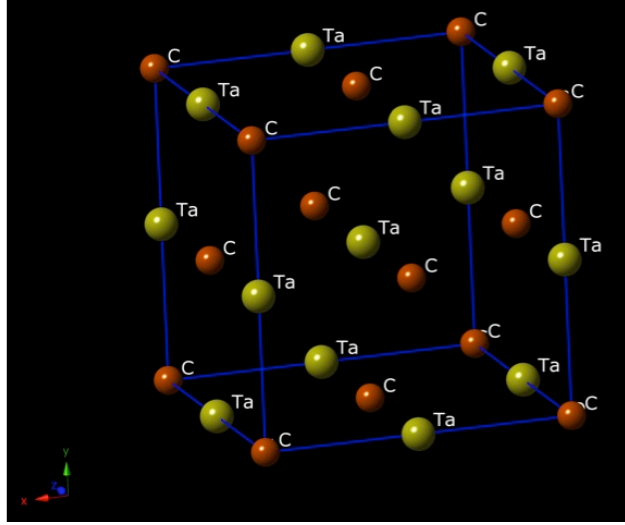
Figure 2.5: 3-D image of TaC unit cell with space group number 225 and lattice parameter a = 0.4454 nm

2.2.5 Slip Modes and Dislocations

2.2.5.1 Cubic Crystal Systems (ZrC, TaC)

Cubic crystal system including face centered cubic (FCC) structure use the three-axis Miller indices system to index the planes and directions. ZrC and TaC both with rocksalt (B1) NaCl crystal structure fall into this category. Planes are shown as (hkl) based on the reciprocal of intersection with each axis and directions are shown as d = Ua1+Va2+Wa3. In cubic system, plane and direction normal have the same Miller indices. Rock salt structure (similar to FCC) follows the cubic crystal system for indexing and finding the slip systems. Slip is a common mode of plastic deformation in FCC structures in which atoms move from their original positions on a close packed plane (slip plane) in a close packed direction (slip direction). Atomic rearrangement normally occurs via movement of dislocations (line defects or extra half–plane of atoms) when material is subjected to shear stress. For FCC system {111} and ⟨110⟩ are the close packed planes and directions respectively as shown in Figure 2.6.

Primary slip direction in ZrC single-crystals like other refractory carbides with rock salt structures (examples are TiC, ZrC, VC, NbC, TaC) is ⟨1$\bar{1}$0⟩ considering the ionic bonding.
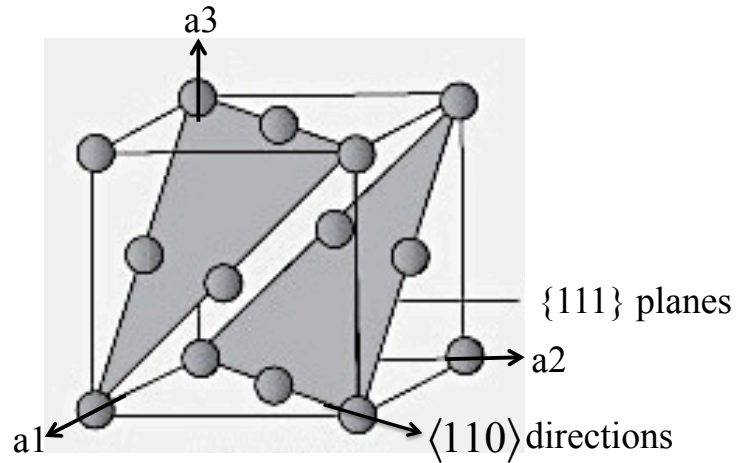
Figure 2.6: Slip plane and direction in FCC system

The shortest repeat distance along $\langle 1\bar{1}0 \rangle$ is $1/2\langle 1\bar{1}0 \rangle$, which is considered the Burgers vector of dislocations. Figure 2.7 contains an image of edge dislocation in NaCl structure.
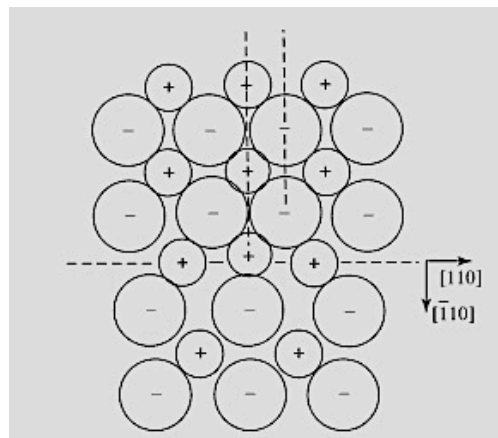
Figure 2.7: Edge dislocation in NaCl structure. Dotted lines are extra half planes of atoms and the slip plane [30]

In ionically bonded compounds with the close-packed NaCl structure, slip cannot occur on the close-packed plane {111} because of electrostatic repulsion forces caused by passing like charged ions near one another. Instead slip occurs primarily on {110} and {100} planes. However, for TiC, ZrC, TaC and similar rocksalt (B1) NaCl crystal structures with mixed metallic-covalent-ionic bonding slip on {111} planes is also possible [31]. Also although $\langle 110 \rangle$

12

or $\langle 1\bar{1}0 \rangle$ are the close-packed direction considering the charge neutrality, since besides ionic bonding these carbides also have dominant metallic (like in TaC) or dominant covalent (like in SiC) bonding, $\langle 100 \rangle$ can also be considered as a possible close-packed or slip direction.

All possible slip systems for rocksalt (B1) NaCl crystal structures and the unit cell of NaCl showing primary slip systems are illustrated in Figure 2.8 and 2.9 respectively.
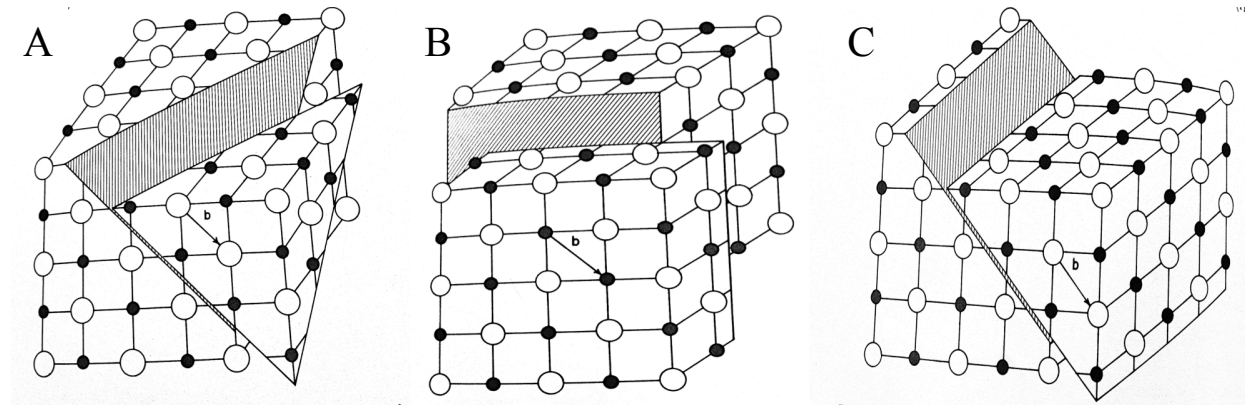
Figure 2.8: Slip systems in B1 NaCl crystal structure, A) $\{111\}\langle 1\bar{1}0 \rangle$, B) $\{001\}\langle 1\bar{1}0 \rangle$ and C) $\{110\}\langle 1\bar{1}0 \rangle$ [32]
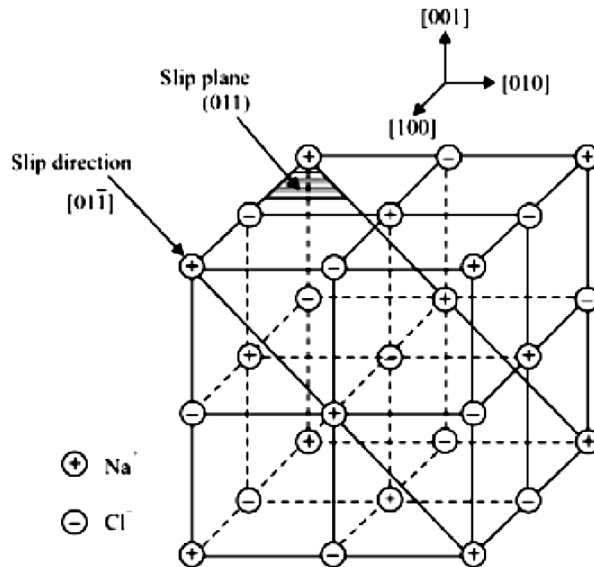
Figure 2.9: The unit cell of NaCl showing the primary slip system [33]

13

Critical resolved shear stress (CRSS) required to initiate slip on a specific plane in a particular orientation is known as $\tau = \sigma \cos\alpha \cos\delta$ where τ is the resolved shear stress, σ is the normal applied stress, and $\cos\alpha \cos\delta$ is the Schmidt factor. α is the angle between the loading direction and normal to the slip plane and δ is the angle between the loading direction and the slip direction. Table 2.4 contains Schmidt factors for single-crystalline ZrC considering three loading directions and [110] as slip direction. Similar is valid for TaC.

Table 2.4: Schmidt factors considering [110] as the direction of slip

Loading direction	Slip plane	Schmidt Factor
[100]	{100}	0
	{111}	0.405
	{110}	0.5
[111]	{100}	0.471
	{111}	0.272
	{110}	0
[011]	{100}	0.353
	{111}	0.408
	{110}	0.25

2.2.5.2 Hexagonal Crystal Systems (SiC)

In a hexagonal crystal system (including wurtzite) two types of dislocations are commonly responsible for plastic deformation; $\langle a \rangle$ type which lies on the basal plane with Burgers vector of $1/3\langle 11\bar{2}0 \rangle$ and $\langle c \rangle$ type that lies perpendicular to the basal plane with Burgers vector of $\langle 0001 \rangle$. Figure 2.10 schematically illustrates these dislocations. Note that lines marked as A, B and C in red are perfect $\langle a \rangle$ type and the line marked as D in blue is perfect $\langle c \rangle$ type dislocations.

In this crystal system plastic deformation is attributed to basal slip, non-basal slip (prismatic slip and pyramidal slip) and/or twinning. Type of dislocations and associated slip
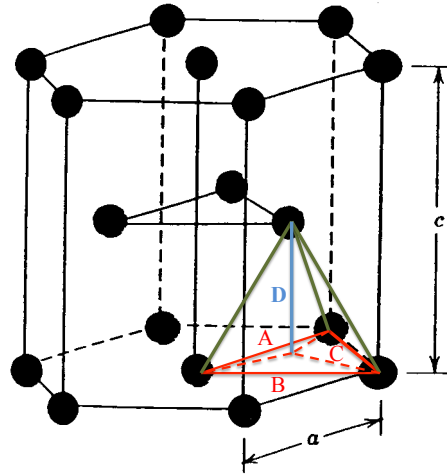
Figure 2.10: $\langle a \rangle$ type (A, B, C) and $\langle c \rangle$ type (D) dislocations in hexagonal system

systems are illustrated in Figure 2.11 and listed in Table 2.5.
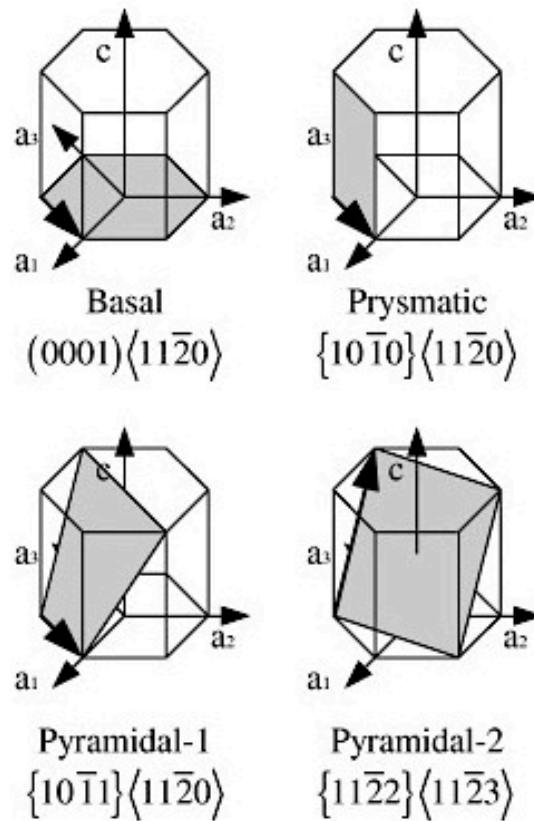
Figure 2.11: Slip systems in hexagonal crystal structure [34]

15

Table 2.5: Slip system, slip plane and slip direction in a hexagonal crystal system

Type of dislocations	Slip system	Slip plane	Slip direction
$\langle a \rangle$	Basal	(0001)	$\langle 11\bar{2}0 \rangle$
$\langle a \rangle$ and $\langle c \rangle$	Prismatic 1st order	$(10\bar{1}0)$ $(10\bar{1}0)$	$\langle 11\bar{2}0 \rangle$ $\langle 0001 \rangle$
$\langle c \rangle$	Prismatic 2nd order	$(11\bar{2}0)$	$\langle 0001 \rangle$
$\langle a \rangle$	Pyramidal 1st order	$(10\bar{1}1)$	$\langle 11\bar{2}0 \rangle$
$\langle a+c \rangle$	Pyramidal 2nd order	$(11\bar{2}2)$	$\langle 11\bar{2}3 \rangle$

2.2.6 Plastic Deformation

Ceramic materials are generally considered to be brittle due to limited motion of dislocations. High hardness and high ductility are desirable yet challenging characteristics to have for ceramic materials used in structural applications. While room-temperature plasticity has been observed, as early as the 1950s in single-crystalline cubic-structured ionic solids [35, 36] and in covalently bonded compounds at smaller length scales [37, 38] progress has been limited in enhancing both ductility and hardness in polycrystalline ceramics due to the lack of fundamental understanding of the mechanisms controlling plastic deformation in this class of materials [39, 40]. Most of the existing literature on this topic is focused on hydrostatic loading (as in micro- or nano-indentation) of these materials or uniaxial loading at high temperatures.

2.2.6.1 (B1) NaCl-Structured ZrC and TaC Deformation Behavior

NaCl-structured ZrC, a group IV transition-metal compound, and TaC, a group V transition-metal compound, due to a mixture of strong ionic and covalent bonds, typically are brittle

at room-temperature and exhibit plasticity at temperatures around 1/3 of their melting point [31]. Previous studies predict that the compressive stress required to induce a fracture in a material increases with decreasing sample size and there exists a critical size below which yielding, rather than brittle fracture, is favored [41]. While in bulk, surface defects could act as stress risers and induce fracture; sub-micron-scale pillars of these compounds could withstand higher stresses because surface defects are minimal. And, at sufficiently high stresses, nucleation and motion of dislocations occur leading to plastic deformation.

Micro-indentation studies on single-crystalline TaC and HfC at room-temperature with orientation of indenter at 0°, 45° and 90° with respect to (100) crystal surface lead to activation of different slips systems. For single crystals of $TaC_{0.96}$ the preferred slip system has been identified as $\{111\}\langle1\bar{1}0\rangle$, even at temperatures as low as 77 K. However, HfC shows preference for $\{110\}\langle1\bar{1}0\rangle$ slip [42,43]. The values of critical shear stress for the (100), (110), and (111) planes of single-crystalline $ZrC_{0.945}$ have been found to be very similar giving rise to operation of all possible slip systems; i.e. $\{111\}\langle1\bar{1}0\rangle$, $\{100\}\langle1\bar{1}0\rangle$ and $\{110\}\langle1\bar{1}0\rangle$ at high temperatures [44]. Hardness anisotropy has been reported for NbC where hardness is governed by crystallographic slip on $\{110\}\langle1\bar{1}0\rangle$ and $\{111\}\langle1\bar{1}0\rangle$ systems [45].

2.2.6.2 Hexagonal SiC deformation Behavior

Observation of plastic deformation and dislocation activity in SiC dates back to 1970 when Stevens [46] showed dislocation generation and slip traces left in β-SiC fractured chips subjected to four-point bending test at room-temperature. Fujita *et al.* [47] experimented compression on single-crystalline 6H-SiC at T $\geq$ 1700 K and observed basal slip, large plastic flow (14%) and dislocation glide motion. Maeda *et al.* [48] in another high temperature compression study related the observed plastic deformation to the movement of basal dislocations and their dissociation into shockley partials. Samant [49] compared the effects of temperature (700 − 1500 K) and strain rate on both 6H- and 4H- SiC specimens with the basal plane inclined by 45° to the compression axis. It is known that when compression loading is along the basal direction [0001], basal slip is suppressed and hence an inclination

is required to motivate the basal slip [50]. In all of these studies, thermally assisted activation over Peierls barrier has been reported as the controlling mechanism for basal slip with {0001} being the dominant slip system. High temperature (1000 − 1500 K) creep behavior of 6H-SiC deformed both parallel to and at 45° to [0001] also showed dislocation glide and pile ups [51].

In hardness studies (micro- and nano- indentation) of 6H-SiC, existence of temperature-dependent hardness anisotropy is reported [52, 53]. Nano-indentation on planes close to {0001} leads to dislocation plasticity and slip at a stress close to the theoretical shear strength, while micro-indentation (Vickers-indentation) results in cracking [21, 54]. Indenter shape and angle of indentation with respect to the surface also effects the stress-strain and work-hardening of 6H-SiC(0001) [55].

When it comes to room-temperature mechanical testing on small-scales, most current literatures are on cubic 3C-SiC. Tensile testing on SiC whiskers with a few microns in diameter dating back to 1970s indicates a high strength of 32 GPa and cleavage rather than plastic deformation [56]. Bending test using an AFM tip revealed a thigh stress of 54 GPa for SiC nanobeams [57]. SiC nanowires subjected to bending test inside a transmission electron microscope and tensile test inside a scanning electron microscope reveal a high strain plastic deformation caused by crystalline to amorphous transition and dislocation nucleation, propagation, amorphization respectively [58, 59].

2.3   Small-Scale Mechanical Testing

2.3.1   *Ex Situ* Versus *In Situ* Microscopy Techniques for Mechanical Testing

Majority of the today's known small-scale mechanical testing dates back to 2004 where compression test of Nickel micron-sized cylindrical shape pillars made via Focused Ion Beam (FIB) is carried out in an MTS Nanoindenter unit. Most indentation units used for nanomechanical characterization of materials use a diamond tip of berkovich, cube-corner or conical shape. They are also equipped with optical microscope (OM) up to 1000X (more commonly

18

400X). The locations of indents are identified prior to indentation through the OM. Analysis of the measured force versus displacement curve (particularly the unloading segment) obtained on a flat surface provides valuable information on reduced modulus and hardness. Figure 2.12 depicts a typical load-displacement curve obtained in indentation experiment. The unloading slope is used for calculation of hardness and modulus.
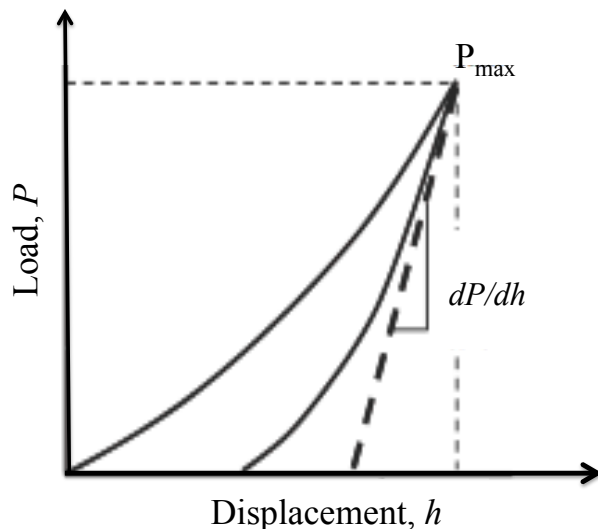
Figure 2.12: Typical indentation plot showing load (P) versus displacement (h)

However, if a flat diamond tip is used, compression instead of indentation can be performed. Instead of a bulk flat surface, cylindrical shape pillars with either circular or rectangular cross-section grown on a surface or milled away via FIB are chosen. This combination of diamond tip and sample geometry gave rise to the small-scale (micron and sub-micron) mechanical testing of materials. However, due to the presence of optical microscope the resolution is limited and post-analysis in an electron microscopy either scanning electron microscope (SEM) or transmission electron microscope (TEM) is required to have a better understanding of possible plastic deformation and its mechanisms. The traditional indentation units used to run compression test on micron-sized pillars are known as *ex situ* testing techniques.

Conventional *ex situ* experiments lack the spatial and time-specific information to investigate the dynamical behavior during plastic deformation. Hence, developments in quantita-

19

tive *in situ* SEM and particularly *in situ* TEM (electron microscope coupled with specifically designed holder) mechanical tests significantly improved our understanding of the deformation mechanisms and mechanical behaviors of materials. Figure 2.13 depicts Hysitron PI85 (*in situ* SEM) and PI95 (*in situ* TEM) employed in this research. The primary feature of *in situ* microscope techniques is to have a time-specific quantitative force-displacement curve and the corresponding electron microscope movie of the stress-induced deformation process.
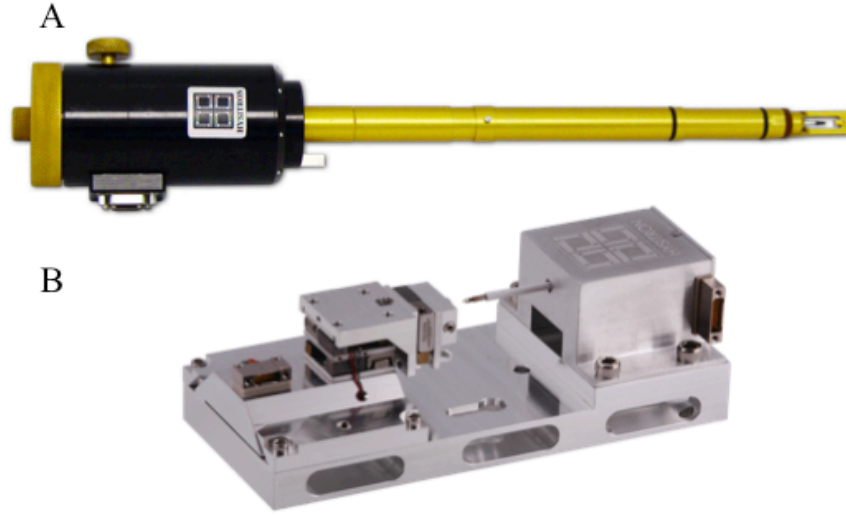
Figure 2.13: Hysitron Inc. A)*in situ* TEM and B)*in situ* SEM holders [60]

2.3.2   Micro and Nano-Compression Test of Metallic Pillars

Sample size and its effect on crystal strength and plasticity dates back to the work by Uchic *et al.* [61]. *Ex situ* compression test on micron-sized cylindrical pillars of single-crystalline nickel and nickel alloys prepared via Focused Ion Beam (FIB) technique is carried out in conventional nanoindentation device (MTS Nanoindenter XP) equipped with flat diamond tip. Since the ability to multiply dislocations or number of dislocation sources are truncated in small volumes, yield strength increases as size decreases. Nickel micropillars after deformation and corresponding engineering stress-strain data are presented in Figure 2.14.

Greer and Nix [62] used both conventional nanoindentation equipment and *in situ* SEM holder to extensively study both FIB- and FIB-less (electroplating) gold micron-sized pillars

20
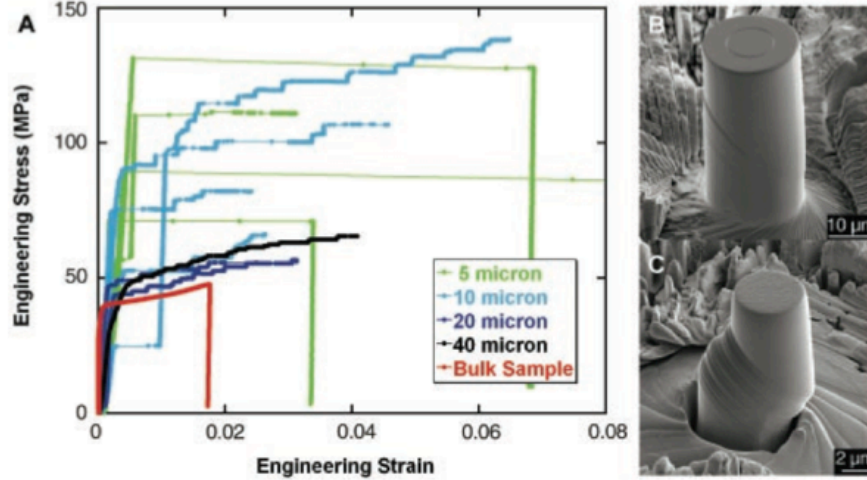
Figure 2.14: A) Plot of engineering stress *vs.* strain of Nickel micropillars with D $= 40~\mu$m - 5 μm. Scanning electron micrograph of B) 20 μm and C) 5 μm pillars after the deformation [61]

applying multiple cycles of loading/unloading to ensure that the unloading data is elastic. Pillars made by both fabrication methods had a yield stress much higher than their bulk counterparts ($\sim$ 30 MPa at 2% strain) with deformation via slip on $\{111\}$ planes. The dominant mechanism responsible for enhanced strength is believed to be dislocation starvation wherein due to confined volume of the pillars, the mobile dislocations have a higher probability of annihilating at a nearby free surface than of multiplying and being pinned by other dislocations. Hence, plasticity is accommodated by the nucleation and motion of new dislocations rather than by motion and interactions of existing dislocations [63, 64].

They also investigated FIB-less single-crystalline copper pillars of $100 - 500$ nm diameter that showed identical size effect to the ones fabricated by FIB. The compressive strengths of copper nanopillars followed a power-law dependence ($\sigma = d^n$) with the slope of n = -0.63 as shown in Figure 2.15. Plasticity at the submicron scale is believed to be a function of microstructure that defines a size effect regardless of the fabrication technique [65, 66].

Face-centered-cubic (FCC) metals show discrete stochastic bursts in the stress-strain curves that are characteristic of small-scale plastic deformation. Studies on aluminum (Al) single-crystals, bi-crystals [67] and poly-crystals [68] show this characteristic clearly. Stress initially increases linearly with strain until the appearance of a small strain burst. The
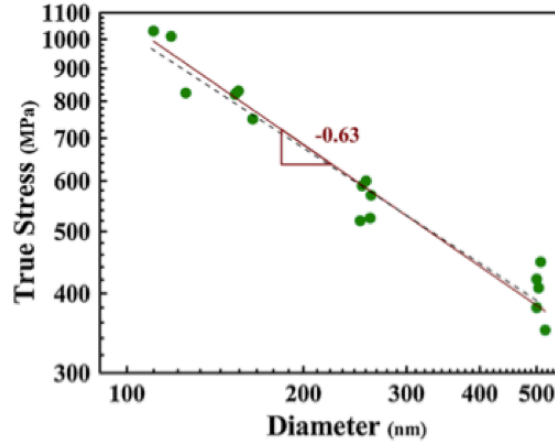
Figure 2.15: Log-log plot of compressive stress versus pillar diameter showing a power-law trend with n = -0.63 [66]

subsequent deformation is serrated with elastic-like behavior in between bursts. Although similar stress-strain behavior and an identical power law "smaller is stronger" size effect is observed in single-crystalline aluminum pillars compared to their bi-crystalline counterparts, but there is little or no dislocation storage in the bi-crystalline pillars suggesting that the grain boundary may act as a dislocation sink. Figure 2.16 depicts the stochastic bursts characteristic of FCC metals for Al[104] pillars.
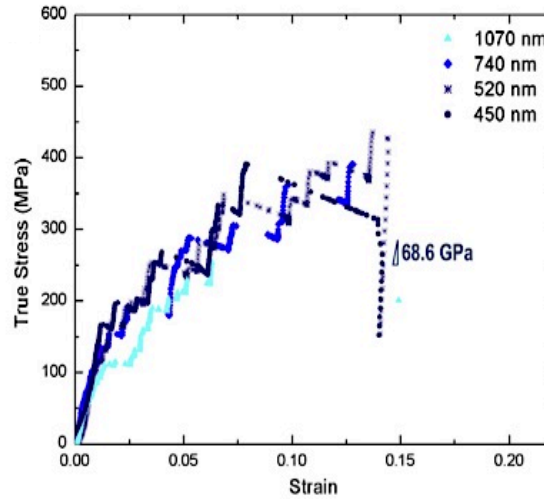
Figure 2.16: Stress-strain curve for Al[104] pillars showing the strain bursts [67]

22

Two main mechanisms for observed plasticity and enhanced strength in FCC metallic pillars as discussed above are known as: 1) dislocation starvation due to escape of the dislocations from the small volume of pillars accompanied by subsequent nucleation of new dislocation (rather than existing dislocations) in order to accommodate further plasticity and 2) dislocation source truncation giving rise to various "strain bursts" through the deformation. To have a burst, a large number of mobile dislocations must be generated, possibly from a source in the pre-existing dislocation debris. During the compression test, although most dislocations tend to leave the small volume of pillar (dislocation starvation), a small fraction of them are obstructed in their pathway and get accumulated inside the pillar. These accumulated dislocations, even though small in number, could be enough to block their own source due to the back stress effects. Once the nucleation process is blocked, further plastic deformation is hindered (i.e. the pillar deforms elastically) until the applied stress is high enough to re-activate the pile-up or to trigger a new source (dislocation source truncation). Overall, dislocation generation is a difficult process, a small addition of resistive stress may hinder the process and further plasticity can proceed only at a raised stress level [63, 68].

Original studies are on nickel, gold, copper, and aluminum, all face-centered-cubic (FCC) metals that due to their multiple slip systems, room-temperature plastic deformation is easy to occur. However, besides FCC metals with multiple slip systems, other metals with hexagonal-closed packed (HCP) and body-centered-cubic (BCC) crystal structures are also investigated.

For Magnesium (Mg) micropillars with HCP structure and orientations favorable for deformation by basal slip and/or extension twinning, plastic deformation mechanism varies from "single slip" for basal slip oriented crystals to "slip + twining" for twin oriented crystals. Twining usually requires higher stress, an order of magnitude higher, than that required for basal plane sliding. It is believed that the interaction between the slip dislocations and twins could be a possible reason for a higher strain hardening behavior in twin-oriented crystals. In addition, micropillars that deform by basal slip exhibit more load drops during plastic deformation [69, 70]. Stress-strain plots and corresponding SEM image of deformed micropillars corresponding to each orientation is compared in Figure 2.17.
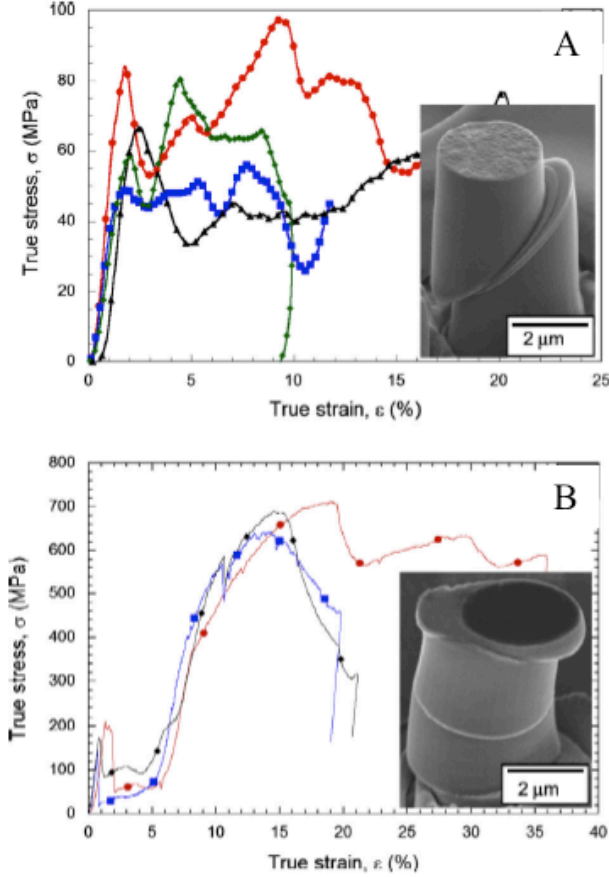
Figure 2.17: Stress-strain curves and post-compression micropillars of Mg crystals oriented for A) single basal slip $(0001)[2\bar{1}\bar{1}0]$ and B) prismatic slip $(10\bar{1}0)[1\bar{2}10]$ and tensile twining [69]

BCC metal pillars due to the higher Peierls stress compared to FCC metals show similar size-scale effect but have different deformation mechanism. For Niobium (Nb) nanopillars the compressive stress-strain curves are comprised of numerous discrete segments with intermittent strain bursts. Formation of dislocation network rather than dislocation starvation contributes to the enhanced plasticity at sub-micron scale [71, 72]. In Molybdenum (Mo) nanopillars, yielding is likely to be governed by a thermally activated process such as kink-pair formation. Plastic deformation show the formation of an entangled dislocation sub-structure where dislocation segments appear to be curved and are likely formed by the cross-slip of screw components in dislocation loops. The flow stress shows strong size effects in both BCC materials [73,74]. The size-dependent behavior of BCC pillars has

been attributed to the competing processes of screw dislocation network formation and their annihilation at the free surface due to image stress [75, 76].

Majority of small-scale testing from 2004 – 2006 and even till now due to various reasons such as cost, specimen constraints, resources (availability of the equipment) are performed either *ex situ* or *in situ* SEM followed by subsequent TEM analysis in some of the studies. However, if equipment is available, *in situ* TEM experiments provide a better insight into the small-scale testing mainly due to the capability of simultaneous testing and observing the plastic deformation at the nano-scale. The first work to employ *in situ* TEM technique to test metallic samples was a work by Minor *et al.* [77] in 2006 to investigate the onset of the plasticity in a single grain of aluminum. They reported that although plasticity in a dislocation-free volume of poly-crystalline aluminum can begin at very small forces, the shear stresses associated with these small forces could approach the theoretical shear strength of aluminum (~ 2.2 GPa). Figure 2.18 shows the generation of dislocations upon *in situ* indentation of an aluminum (Al) grain along with the corresponding mechanical data.
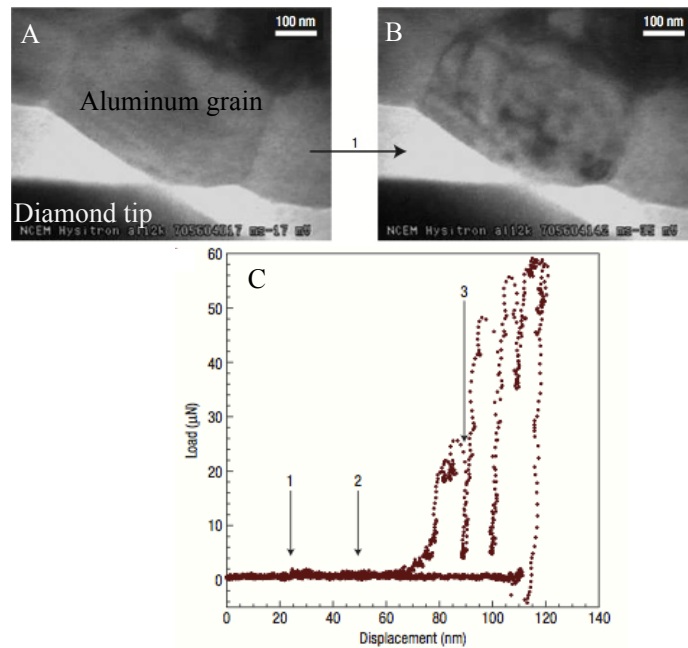
Figure 2.18: A-B) TEM images extracted from the movie showing the generation of dislocations in an Al grain, C) corresponding mechanical behavior [77]

Employing *in situ* TEM mechanical test was adapted by Shan *et al.* [78] later to study deformation behavior of single-crystalline nickel nanopillars as illustrated in Figure 2.19 and continued for other materials. Mechanical annealing followed by strain hardening due to dislocation starvation as well as activation and subsequent exhaustion of dislocation sources are observed.
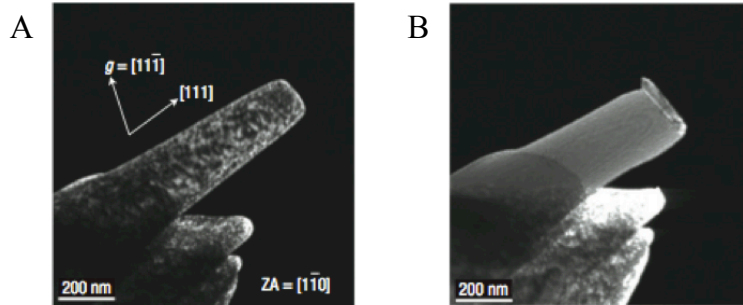
Figure 2.19: Dark-field TEM image of the nickel nanopillar A) before the test showing high initial dislocation density and B) after the first test being free of dislocations as an indication of mechanical annealing [78]

The research on small-scale behavior of materials started using conventional *ex situ* nanoindentation devices equipped with flat diamond punch on micron- sized pillars and then moved to more elaborate *in situ* microscope techniques; *in situ* SEM and *in situ* TEM on sub-micron pillars as discussed above. However, they all had one main goal: better understanding the mechanical response and deformation mechanism at micron and sub-micron scales; a size regime that was not much known.

The interest in the small size-scale mechanical testing is not however limited to metals only. It started with metals with known plasticity and more active slip systems at room-temperature, and moved to non-metallic materials as discussed in the next section.

2.3.3 Micro and Nano-Compression Test of Non-Metallic Pillars

Small-scale mechanical testing on non-metallic materials due their inherent brittle nature at room-temperature didn't start as early as metals. Enhanced plasticity in brittle materials

at room-temperature is generally attributed to three main factors: small volumes are free of stress risers, high stress can nucleate dislocations at free surfaces at low temperatures, and low activation energy is needed for dislocation nucleation at high stress [1].

Studies on silicon [79–81], bulk metallic glass (BMG) [82–85], GaAs [38], intermetallic compounds [86], and MgO [35,87] state the existence of a critical size for enhanced plasticity and brittle-to-ductile transition. Larger pillars have axial cracking, splitting and cleavage and smaller pillars show more homogeneous behavior, plastic flow and formation of slip bands. Ostlund *et al.* [38,80] suggest an increase in the fracture energy and a decrease in the crack driving force for the existence of the critical size in brittle materials.

Brittle-to-ductile transition with cracking *vs.* no cracking is illustrated for silicon micropillars subjected to uniaxial compression in Figure 2.20. Dislocations nucleate on the surface of the silicon pillar and move through the pillar on {111} planes. It is believed that dislocations in silicon are generally dissociated into two partial dislocations separated by a stacking fault. Brittle-to-ductile transition is attributed to the mobility of partial dislocations and the fact that dislocations in the shuffle set are nucleated at very high stress in the small volumes.
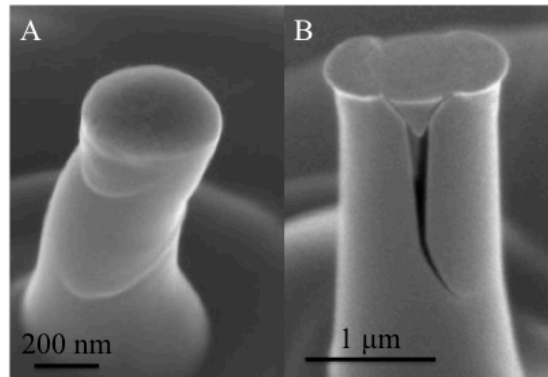
Figure 2.20: HR-SEM image of A) 310 nm and B) 940 nm silicon pillars after *ex situ* compression test showing size-dependent plastic deformation [80]

For GaAs micropillars the effect of pillar diameter on yield stress showing the transition from splitting to plastic flow is illustrated in Figure 2.21. Data is plotted based on $\sigma =$

$\frac{K1c}{0.158\beta\sqrt{d}}$ considering $\beta = 0.79$. To avoid splitting, the micropillar should be no larger than 1μm. The scatter in the yield stress suggests that there is a spread of dislocation link lengths within the pillars and has been invoked as a reason for the increase in the yield stress as the sample volume is decreased. Ductile-brittle transitions, is believed to occur not because plastic flow has become easier, but because decreasing the size has made cracking more difficult [38].
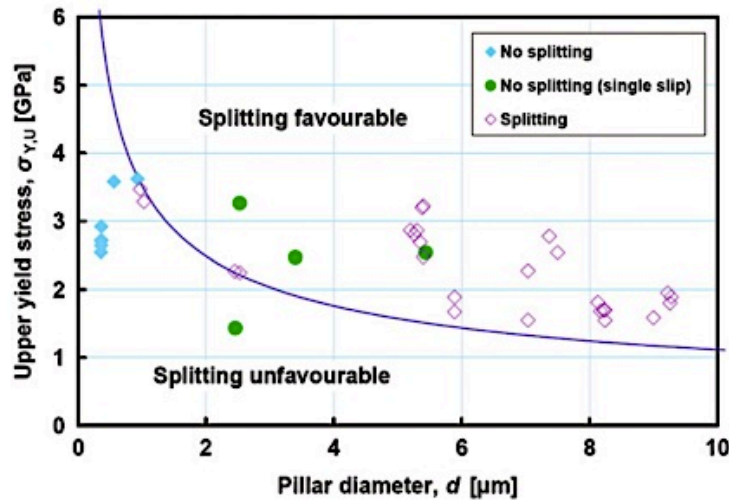
Figure 2.21: Yield stress *vs.* pillar diameter indicating larger pillars are more prone to splitting, while smaller pillars have plastic flow [38].

Compression test on LiF micropillars at two different crystallographic orientations; [001] and [111] reveals that LiF[001] micropillars have a strong size dependence of yield stress, while no size-effect is seen for LiF[111] micropillars. Plastic deformation along "soft" $\{110\}\langle110\rangle$ and "hard" $\{100\}\langle110\rangle$ slip systems are dominant for LiF[001] and LiF[111] respectively [88, 89].

Similar behavior is seen for MgO micropillars compressed along [001] and [111] directions where "soft" $\{110\}\langle1\bar{1}0\rangle$ and "hard" $\{100\}\langle1\bar{1}0\rangle$ slip systems are respectively active. The stress-strain behavior is distinctively different with discrete strain bursts and shear deformation for MgO[001] and more homogeneous stress flow indication of plastic deformation for MgO[111]. Figure 2.22 contains the stress-strain plots for thee different sizes MgO micropil-

28

lars in each crystallographic orientation.
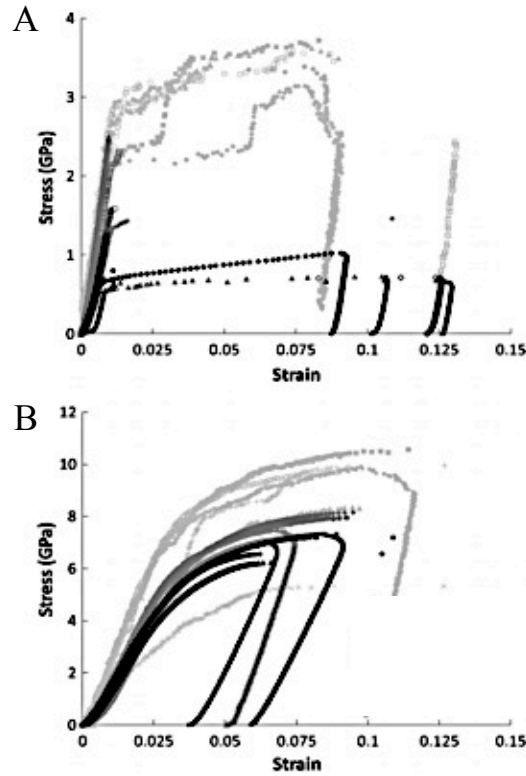
Figure 2.22: Stress-strain plot for A) MgO[001] and B) MgO[111]. Light gray: 0.5 μm, dark gray: 2 μm and black: 5 μm [35]

2.3.4 Alternative Small-Scale Test Methods

Small-scale testing is not limited to only compression test on micron and sub-micron pillars. To name a few, compression test on silicon nanospheres [37, 90, 91], tensile test on molybdenum nanowires [92, 93], copper and aluminum nanobars [94–96] and bending of SiC nanowhiskers [58] have also been the subject of various researches. For silicon nanospheres with diameter in the range of 20 – 50 nm a hardness of 50 GPa almost 4 times the bulk value (12 GPa) is obtained. Based on dislocation hardening due to either the back stress of a dislocation pile-up or a formation of dislocation "forest" of closely spaced dislocations as in Taylor hardening, the strength of silicon nanospheres is inversely proportional to sphere

diameter; $\sigma \approx \dfrac{2\mu N b}{\pi(1-\nu)d}$ where μ is the shear modulus, N is the number of dislocations, b Burgers vector, ν poison's ratio and d is the sphere diameter. It is believed that surface site nucleation is the controlling mechanism with the new surface sites requiring additional stress leading to higher hardness (strength) than bulk.

Kiener *et al.* [94] pioneered a method to investigate tensile behavior of single-crystalline materials at the micro- and nano-scales inside of a scanning electron microscope (SEM) and a transmission electron microscope (TEM). Single-crystalline copper (Cu) tensile samples with diameters ranging from 500 nm to 8 μm and aspect ratios between 1:1 and 13.5:1, fabricated via FIB, are subjected to uniaxial tensile testing as shown in Figure 2.23. A size effect, although less pronounced than in compression, is found to be strongly dependent on the aspect ratio of the sample. Size-dependent hardening is attributed to the formation of dislocation pile-ups due to the constrained glide of the dislocations in the sample caused by the sample geometry and gripping constraints.
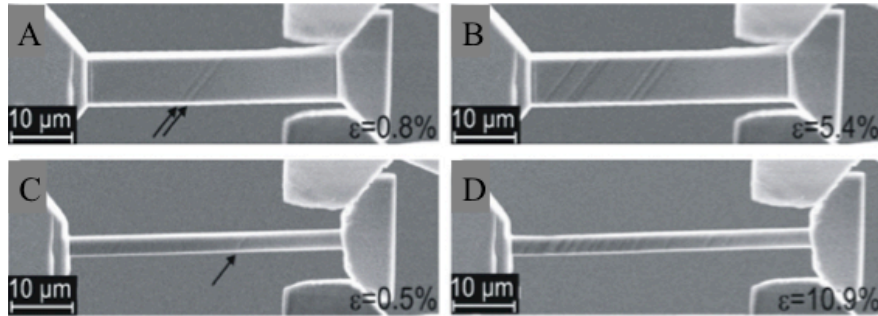
Figure 2.23: Uniaxial tensile test on micron-size copper tensile bars with different aspect ratios showing initiation and progress of slip bands [94]

When Molybdenum (Mo) samples (BCC crystal) are subjected to tension test, a significant tension-compression asymmetry as a function of both crystallographic orientation and size-scale is observed. The amount of strain-hardening in Mo tensile samples is significantly less pronounced than Mo compression samples. It is suggested that the differences in the Peierls stress in twinning *vs.* anti-twinning deformations, a strong dependence of CRSS on the non- glide applied stress tensor components and contribution of the non-planar screw dis-

location cores' motion in response to the applied shear stress are responsible for the observed behavior [92, 93].

All the above-mentioned experiments focus on two main outcomes: **First** to prove the hypothesis of "smaller is stronger". Similar to Hall-Petch formula in poly-crystalline metals where yield stress is proportional to inverse square-root of grain size, yield stress of pillars is proven to be proportional to inverse square-root of pillar diameter under uniaxial compression as discussed by Zhu *et al.* [97] for ceramics and Volkert *et al.* [98] for gold pillars. **Second** to explain the deformation mechanism; dislocation source truncation and dislocation starvation are reported to be responsible for higher strength in confined volumes of metals [99], while less susceptibility to flaws and dislocation nucleation under high stress are accounted for enhanced plasticity in small volumes of brittle materials at room-temperature [1].

CHAPTER 3

Experimental Procedures

Sub-micron pillars of ZrC, TaC and 6H-SiC studied in this research are all prepared via Focused Ion Beam (FIB) technique and subjected to uniaxial compression test using Hysitron PicoIndenter PI95 holder equipped with a flat diamond punch inside a JEOL 3010 transmission electron microscope. Details of sample preparation and experiments are described in this chapter.

3.1 Sample Preparation Using Focused Ion Beam (FIB)

Pillars are prepared via Ga^+ ion milling using FEI 235 FIB/SEM dual beam system. Dual beam FIB/SEM systems are a combination of sample preparation, imaging and analysis in one unit. Sample is mounted at 52° with respect to electron beam, while ion beam is perpendicular to the surface. Gallium (Ga^+) is mostly used as an ion source that based on the accelerating voltage and current impinges on the surface of the sample. When ion hits the sample, secondary electrons, secondary ions and sputtering atoms get generated. Sputtering happens as a result of elastic collision of ions and sample and "mill away" a particular pattern as defined. However, in this process Ga^+ implantation and redeposition of sputtered atoms can occur leading to a formation of amorphous layer that is considered an artifact of FIB ion milling. This effect is less pronounced in ceramics due to their high hardness compared to metals. Schematic of electron beam, ion beam and sample position in FIB/SEM dual beam system is shown in Figure 3.1.
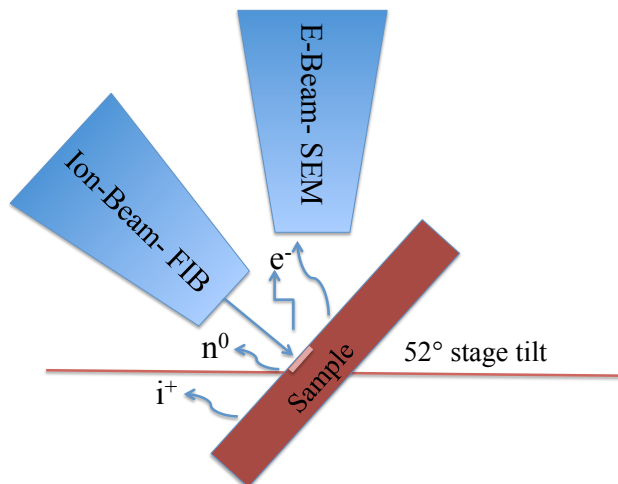
Figure 3.1: Schematic of sample position in the FIB/SEM dual beam system

3.1.1 Single-Crystalline ZrC and TaC

Single-crystalline ZrC(100) and ZrC(111) wafers with dimension 2-mm-thick $\times$ 2 mm diameter are purchased from Applied Physics Technologies. Both wafers are polished on (100) and (111) sides respectively. First, each wafer is cut into two halves and one half of the crystal is mechanically polished to sub-100 μm thickness using Multiprep auto-polisher (Allied High Tech Products, Inc.). Then the sample is mounted on a copper half grid using M-bond 610 adhesive (Micro-Measurement) set at 160 °C for 1.5 hours. Mounting the sample on a half grid enables easy handling for post analysis. Then, the grid sample is placed on a copper sample mount purchased from Hysitron Inc. using Crystalbond$^{\text{TM}}$ 509 adhesive (Ted Pella, Inc.) and transferred to a FEI 235 dual beam FIB system for milling. Figure 3.2 (A-E) schematically illustrates steps of sample preparation prior to FIB. Note that the figures are not to scale.

Pillars of diameters D between 100 and 500 nm with aspect ratios of 1.5 – 3.3, chosen to minimize buckling, are prepared using 30 kV Ga^+ beams. Prior to milling, the whole assembly (sample + copper half grid + copper sample mount) is mounted on a 45-degree stub using Pelco colloidal graphite Paste (Ted Pella, Inc.) to maximize the conductivity and minimize the drift during ion milling. Then the stub is placed inside the FEI 235 dual

33
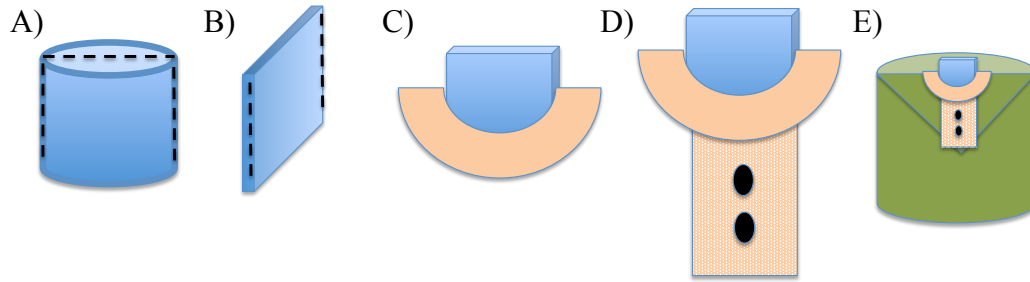
Figure 3.2: Steps of sample preparation prior to FIB, A) cutting the wafer in half, B) mechanically polished to sub-100 μm thickness, C) mounting the sample on a half grid and D) placing the grid sample on a copper sample mount, E) sample on a 45-degree stub when placed inside the FIB/SEM dual beam system

beam system and tilted for another 7°. At this tilt, ion beam is perpendicular to the surface of the sample and electron beam is at 52°. After adjusting the focus and eucentric height, milling starts in three steps. Initial coarse milling is carried out at an ion beam current of 20 nA perpendicular to the sample surface; top view to make a "thin wall". Then the sample is rotated 180° enabling side view of the sample. At this step, medium milling at an ion beam current of 1 nA is used to make individual "islands". For the final step, the sample is rotated 180° one more time to be at the original top view position. Now the fine milling at an ion beam current of 30 pA is used to make cylindrical shape pillars on each "island". This milling procedure yielded pillars with a slightly tapered (less than 3 degrees) geometry. Electron-beam images showing milling steps to prepare sub-micron pillars are shown in Figures 3.3 and 3.4.
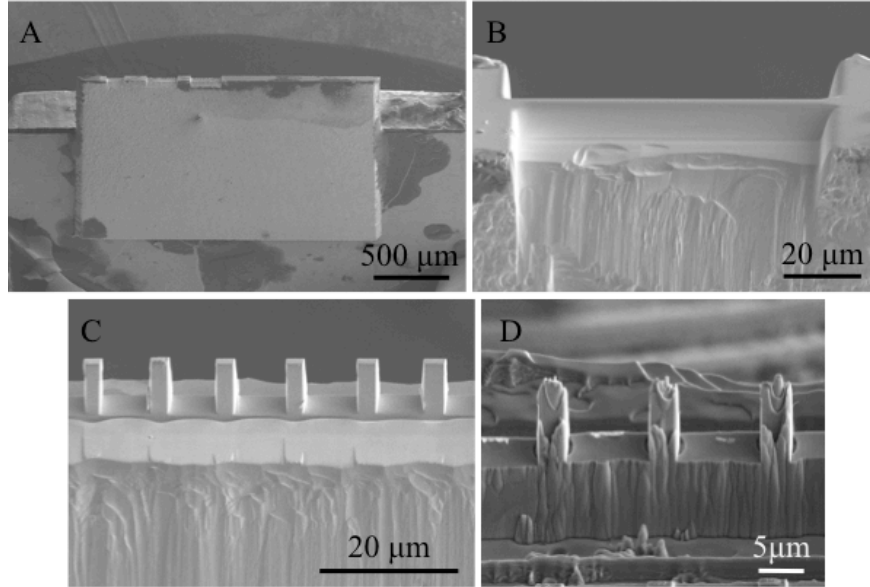
Figure 3.3: Electron-beam images showing A) The entire sample with milled islands on the edge, B) course milling step to mill the "thin wall", C) medium milling step to make individual "islands" and D) fine milling step to make one pillar on each island
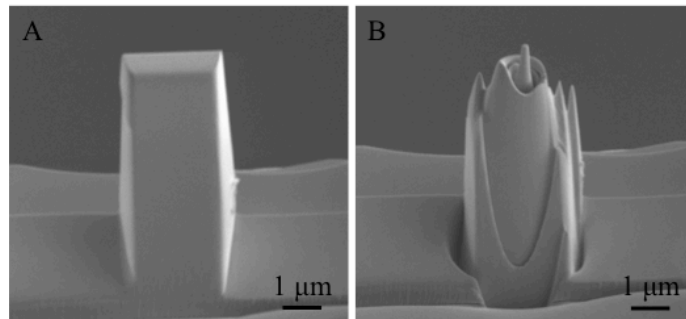
Figure 3.4: Electron-beam images showing A) one island and B) one pillar at the final stage

Similar sample preparation steps as shown in Figures 3.2-3.4 are also applied to TaC samples to prepare sub-micron pillars. Single-crystalline TaC(100) and TaC(011) wafers with dimension 2-mm-thick × 2 mm diameter are purchased from Applied Physics Technologies. Both wafers are polished on (100) and (011) sides respectively. Figure 3.5 compares two finished pillars of TaC(100) after milling and prior to the mechanical testing.
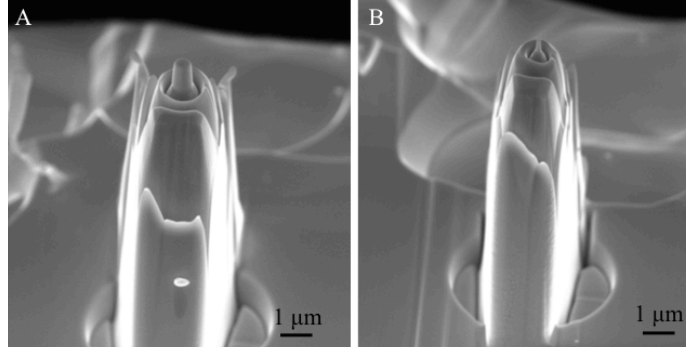
Figure 3.5: Electron-beam images of milled TaC(100) pillars with final diameter of A) 500 nm and B) 100 nm

3.1.2 Single-Crystalline 6H-SiC

Single-crystalline 6H-SiC(0001) wafer with dimension 5mm × 5mm × 0.3 μm and polished on one surface is purchased from MTI Corporation. To prepare pillars two methods are used:

1) To prepare 6H-SiC(0001) pillars - Φ_0 - where loading direction is along $\langle 0001 \rangle$, first a 1 × 1 × 0.33 mm piece is cut out of the larger crystal with a diamond saw and mechanically thinned to sub-100 μm thickness using Multiprep auto-polisher (Allied High Tech Products, Inc.). Then the sample is mounted on a copper half grid using M-bond 610 adhesive (Micro-Measurement) set at 160 °C for 1.5 hours. Mounting the sample on a half grid enables easy handling for post analysis. Then, the grid sample is placed on a copper sample mount purchased from Hysitron Inc. using Crystalbond$^{\text{TM}}$ 509 adhesive (Ted Pella, Inc.) and transferred to a FEI 235 dual beam FIB system for milling. Figure 3.6 (A-D) schematically shows steps of sample preparation prior to FIB. Note that the figures are not to scale.

2) To prepare 6H-SiC - Φ_{45} - pillars where loading direction is at 45° with respect to $\langle 0001 \rangle$, the 1 × 1 × 0.33 mm piece is first mounted on a 45-degree stub and mechanically polished using Multiprep auto-polisher (Allied High Tech Products, Inc.) to make the 45°-cut-surface. Then the piece is remounted on its side and mechanically polished from 0.33 mm thickness to sub-100 μm using Multiprep auto-polisher (Allied High Tech Products, Inc.). All the other pillar fabrication steps are as described in the previous section for Φ_0 pillars.

Figure 3.7 (A-E) schematically illustrates steps of sample preparation prior to FIB. Note that the figures are not to scale.
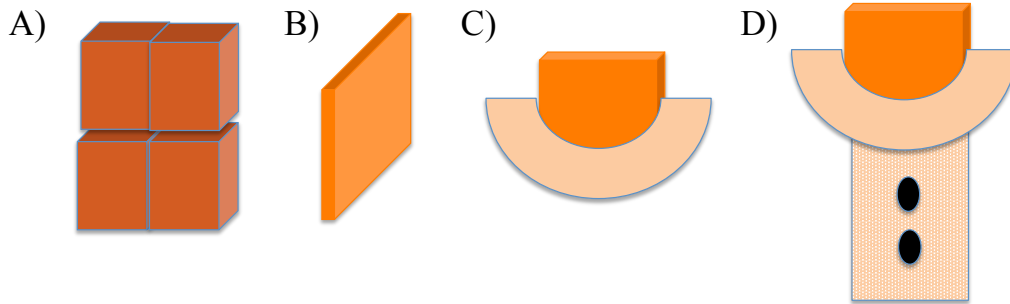
Figure 3.6: Steps of sample preparation prior to FIB, A) cutting the wafer to smaller pieces, B) mechanically polishing to sub-100 μm thickness, C) mounting the sample on a half grid and D) placing the grid sample on a copper sample mount
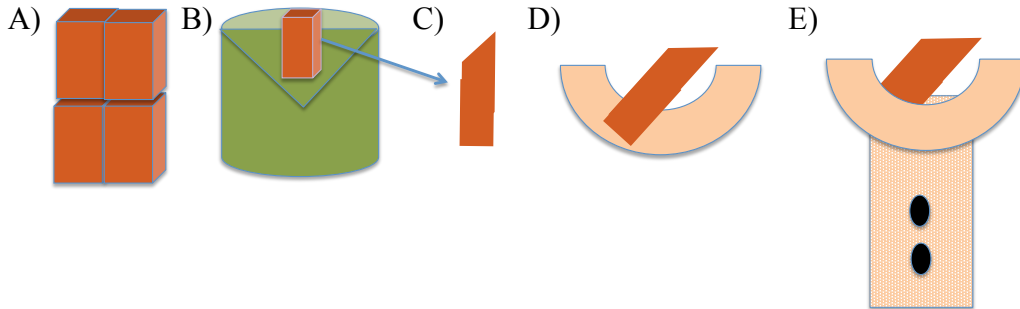
Figure 3.7: Steps of sample preparation prior to FIB, A) cutting the wafer to smaller pieces, B) mounting the piece on a 45° stub to cut the angle, C) remounting on the side and mechanically polishing to sub-100 μm thickness, D) placing the sample on a half grid and E) fixing the grid sample on a copper sample mount

Pillars of diameters D between 170 and 300 nm with aspect ratios of less than 3.3, chosen to minimize buckling, are prepared using 30 kV Ga^+ beams. Prior to milling, the whole assembly (sample + copper half grid + copper sample mount) is mounted on a 45-degree stub using Pelco colloidal graphite Paste (Ted Pella, Inc.) to maximize the conductivity and

minimize the drift during ion milling. Then the stub is placed inside the FEI 235 dual beam system and tilted for another 7°. Figure 3.8 schematically shows the whole assembly as it is put inside the FEI 235 dual beam system for both orientations.
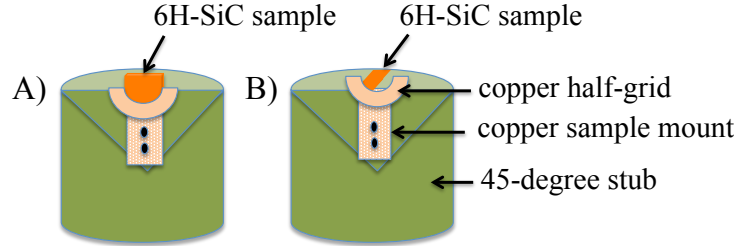
Figure 3.8: Schematic of ready to mill samples A) 6H-Si(Φ_0), B) 6H-SiC(Φ_{45})

At this tilt, ion beam is perpendicular to the surface of the sample and electron beam is at 52°. After adjusting the focus and eucentric height, milling starts in three steps. Initial coarse milling is carried out at an ion beam current of 20 nA perpendicular to the sample surface; top view to make a "thin wall". Then the sample is rotated 180° enabling side view of the sample. At this step, medium milling at an ion beam current of 1 nA is used to make individual "islands". For the final step, the sample is rotated 180° one more time to be at the original top view position. Now the fine milling at an ion beam current of 30 pA is used to make cylindrical shape pillars on each "island". Figure 3.9 shows electron beam image of the 6H-SiC(Φ_{45}) sample when placed inside the FIB/SEM dual beam system.
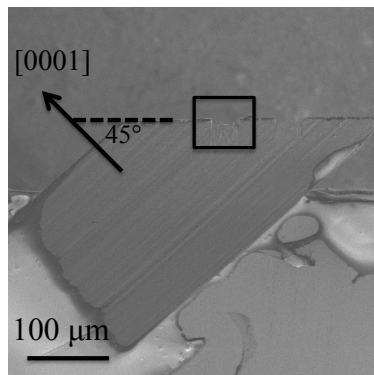
Figure 3.9: 6H-SiC sample cut and polished 45° with respect to $\langle 0001 \rangle$ (Φ_{45}).

Milling steps to achieve sub-micron pillars are similar to ZrC specimen shown in Figures 3.3 and 3.4.

3.2 Uniaxial Compression Using Hysitron PicoIndenter PI95 Inside Transmission Electron Microscope

Transmission electron microscope (TEM) used in the field of materials science and physics particularly from 1930s is a powerful tool for microstructural analysis. It is mainly based on interaction of electron beams with a thin (200 nm and below) sample through elastic, inelastic scattering or no interaction; transmitted beam. Transmitted beam is used in bright-field imaging where intensity of the beam and the sample thickness are inversely proportional. Elastic scattering based on Bragg's law: $2d\sin\theta = n\lambda$ deals with constructive interaction of electrons and atoms with no energy loss where a pattern of spots each representing a specific plane – known as diffraction pattern – can be extracted. Electrons-atoms inelastic scattering is responsible for electron energy loss spectroscopy (EELS) and formation of Kikuchi lines. Each of these interactions provide information on crystal orientation, atomic arrangement, chemical composition, phase contrast, etc. that make TEM a unique material characterization technique [100].

Quantitative *in situ* TEM approach offers more dynamic information and has several advantages compared to *ex situ* techniques. It allows us to extract time-to-time mechanical response of the specimens, while simultaneously recording the microstructure evolution. Exact correlation of mechanical behavior (such as displacement bursts) to time resolved TEM images are crucial for understanding the room-temperature deformation mechanism and mechanical behavior of materials. It also provides better positioning and alignment of the pillar with respect to the diamond tip through live observation of the specimen prior the experiment [77, 78].

Pillars prepared via focused ion milling in this study are transferred to the JEOL 3010 TEM for uniaxial compression. The whole assembly (sample glued to copper half grid and then glued to copper sample mount) needs to be released from the 45-degree stub and

carefully cleaned using acetone. Hysitron PicoIndenter PI95 holder is used for uniaxial compression test inside a JEOL 3010 microscope. Figure 3.10 depicts Hysitron PicoIndenter holder for JEOL microscope.

Figure 3.10: PicoIndenter PI95 holder for *in situ* TEM uniaxial compression test

The PicoIndenter holder employs a piezoelectric actuator for fine scale positioning and a miniature transducer to measure applied load and displacement. All of the *in situ* TEM uniaxial compression experiments are carried out in displacement control mode. Loading rate is first chosen as 10 nm/s for ZrC pillars, but then later in the research it is decreased to 4 nm/s for TaC and SiC pillars. The change is due to the fact that slower loading rate leads to slower deformation that can be better observed and captured with the camera particularly in case of dislocation movement through the pillars. Table 3.1 summarizes specimen orientation, loading direction and loading rate for the tested ceramic pillars. During each test, load-displacement data and corresponding videos (30 frames/s) are acquired using Orius SC200D camera (Gatan Inc.). Also bright-field, dark-field and selected area diffraction patterns (SAED) are recorded prior to and after each experiment to reflect any morphology and microstructural changes.

Since the Hysitron PicoIndenter is a single tilt stage, the samples are transferred to a double tilt holder for post-compression studies.

3.3 Post-Compression Analysis

To gain a better insight into the deformation mechanism, tested pillars are first analyzed using double tilt holder inside JEOL 3010 microscope. Further, the samples are investigated

Table 3.1: Crystal orientation, loading direction and loading rate

Specimen	Crystal orientation	Loading direction	Loading rate
ZrC	[100]	[100]	10 nm/s
	[111]	[111]	10 nm/s
TaC	[100]	[100]	4 nm/s
	[011]	[011]	4 nm/s
6H-SiC	[0001]	$[0001]\Phi_0$	4 nm/s
		$45°$ w.r.t. $[0001]\Phi_{45}$	4 nm/s

using double tilt holder in Titan X microscope operated at 300 kV. Prior to post-compression analysis, to better observe the deformed area, pillars of interest are further thinned to half of their initial diameter using FIB milling operated at 10 kV. Then, the samples are transferred to NanoMill 1040 (Fischione Instruments) in which a 2 kV, 150 μA Ar^+ beams are used to "clean" the pillars and remove Ga^+ damage. This procedure enables higher resolution imaging and better characterization of the microstructure of the pillars. Bright-field, dark-field and selected area diffraction patterns (SAED) are recorded for in-depth investigation of slip systems and modes of plastic deformation in the tested sub-micron pillars. Figure 3.11 depicts electron beam and ion beam images of a post-compression thinned TaC(011) pillar.

In addition for 6H-SiC pillars, high-resolution scanning TEM images are also acquired using abberation-corrected TEAM 0.5 microscope to observe the atomic-level resolution image of the crystal structure and estimate any lattice distortion due to the plastic deformation in the deformed pillars. An extra step of plasma cleaning using for 60 s is recommended prior to placing the sample inside the microscope to eliminate any contamination.

3.3.1 Abberation-Corrected TEAM 0.5

TEAM project based in Lawrence Berkeley National Laboratory employs a series of lenses to correct for spherical and chromatic aberrations. It has a spatial resolution below 0.05 nm and offers great potential for various atomic-level resolution imaging. High-angle annular
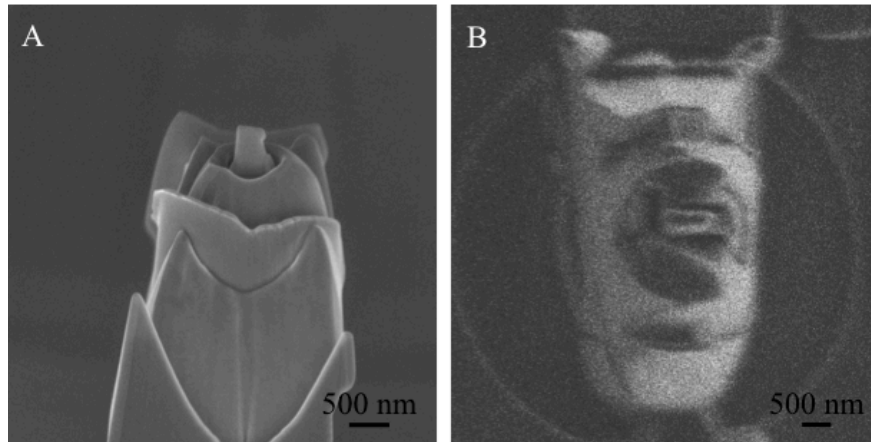
Figure 3.11: A) electron beam image and B) ion beam image of thinned TaC(011) prepared for post-compression analysis

dark-field (HAADF) High-resolution scanning TEM (STEM) images and condensed beam electron diffraction (CBED) patterns from the deformed pillars are acquired at 300 kV.

In order to further investigate the deformation mechanism and to compare with the experimental results, density functional theory (DFT) calculations and molecular dynamics (MD) simulations are performed through a collaborative work.

3.4 Density Functional Theory (DFT) Calculations

1) **DFT calculations for ZrC and TaC**: All the DFT calculations on ZrC and TaC are done in collaboration with Dr. Christian Ratsch from the Department of Mathematics and Institute for Pure and Applied Mathematics, University of California Los Angeles. All of our DFT results presented here are obtained with the FHI-AIMS code using supercells with periodic boundary conditions and GGA-PBE for the exchange-correlation functional. FHI-AIMS is an all-electron full potential DFT code that uses numeric atom-centered orbitals as its basis set. The slab consists of at least 12 layers that are periodic in the x and y directions and separated by at least 30 Å of vacuum along the z-direction. The convergence of our results with respect to the slab and vacuum layer thicknesses, basis set, and the density of the (numerical) integration mesh are carefully tested, and have used parameters as they are

implemented in FHI-AIMS in the default setting "light". The results are essentially the same as those obtained with the default setting "tight". Full details are presented in a paper and only some of the results of this collaborative work are mentioned in this dissertation.

2) DFT calculations for 6H-SiC: All the DFT calculations on 6H-SiC are done in collaboration with graduate student Kai Wing Kelvin Leung and Dr. Derek H. Warner from the school of Civil and Environmental Engineering, Cornell University. The simulation cell is a fully periodic 6H-SiC crystal with both its lateral dimensions equal to one crystallographic period length ($= 0.31 \times 0.53$ nm) and 12 layers of atoms ($= 2.94$ nm) with a 1.75 nm vacuum layer along the vertical dimension. Electronic structure calculations are performed using Kohn-Sham DFT approach with the Vienna *ab initio* simulation package (VASP) [101]. Core electrons of each atom are assumed fixed using an ultrasoft pseudo-potential model. The exchange and correlation interactions of the electrons are approximated with the generalized gradient approximation (GGA). The simulation cell is discretized with a plane wave basis set having a plane wave cutoff energy of 240 eV. A Brillouin zone integration scheme having an $8 \times 8 \times 1$ k-point grid is employed. These parameters as well as the simulation cell height and vacuum layer thickness are tested by using larger height and thickness to ensure energy convergence. The generalized stacking fault (GSF) energies E_{GSF} are calculated as a function of normalized rigid displacement (x/b) by rigidly shifting the atomic layers in the top part of the cell against the fixed bottom layers. The simulation cell is subsequently relaxed perpendicular to the slip plane to attain the minimum energy configuration. Full details are presented in a paper and only some of the results of this collaborative work are mentioned in this dissertation.

3.5 Molecular Dynamics (MD) Simulations

All the MD simulations on 6H-SiC are done in collaboration with graduate student Kai Wing Kelvin Leung and Dr. Derek H. Warner from the school of Civil and Environmental Engineering, Cornell University. The MD simulations are performed using LAMMPS package [102] with Devanathan *et al.* potential [103] for SiC. This potential reliably reproduces

equilibrium properties of the crystal including lattice parameters, elastic constants, cohesive energy, and point defect formation energy. In the simulation, cylindrical, defect-free, 6H-SiC single crystals with diameter D = 8.4 nm and a height of 24 nm, consisting of 133,690 atoms, are oriented such that the direction of the applied load is 45° with respect to the basal plane, i.e. {0001}. The simulation cell is first thermalized for 10 ps at 300 K to release surface stresses in all directions and to initialize atomic positions and velocities. The cell temperature is controlled by a Langevin thermostat. A canonical (NVT) ensemble is employed with an integration time step of 1 fs for the velocity-verlet integration scheme [104]. Uniaxial compression is simulated by imposing deformation on the cell at a strain rate of 5.7×10^9 s^{-1}. Stresses are computed with the virial theorem [105] and strains are computed from the changes in the crystal height. Atomistic visualization is performed with the Atomeye package [106]. Full details are presented in a paper and only some of the results of this collaborative work are mentioned in this dissertation.

3.6 Push-to-Pull (PTP) Device for *In Situ* Tensile Test

Push-to-Pull (PTP) device is an *in situ* tensile apparatus designed to work with Hysitron's commercially available PI series PicoIndenter for TEM and SEM. To make tensile bars a standard lift-out procedure using Ga$^+$ ion milling is followed. The thin lamellas are then transferred to a grid (or in this case PTP device) with the use of omni needle. In case of nanowires, most likely no milling step is needed and the individual wires are picked with the omni needle to be transferred to a grid (or in this case PTP device). The sample, either a tensile bar or a nanowire, is fixed on the PTP device mainly by platinum deposition inside the SEM/FIB dual beam system. Then the PTP device is mounted on PI95 TEM holder. Although this holder is widely used for compression test, the specific design of the PTP device enables tensile loading on the sample. When the diamond tip is in contact with the PTP device, the compressive force at point 1 as shown in Figure 3.12(A) leads to tensile force on the sample labeled 2 in Figure 3.12(B). A uniaxial tensile test is now performed on the nano-tensile sample in which load-displacement data along with any morphology and

44

microstructural change in the sample are recorded simultaneously.
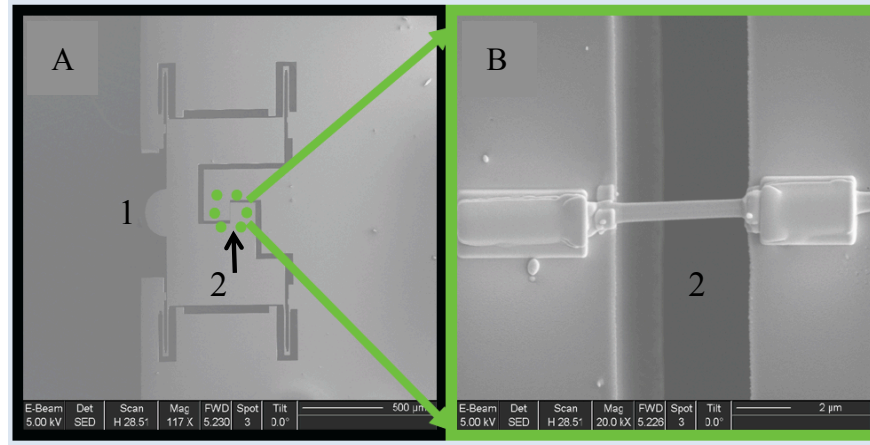
Figure 3.12: A) PTP device for *in situ* TEM tensile testing, B) enlarged location of the sample [107]

CHAPTER 4

Shear *vs.* Dislocation Plasticity
in Single-Crystalline ZrC

In this chapter results of uniaxial compression test on ZrC(100) and ZrC(111) sub-micron pillars, their deformation mechanisms and effects of size-scale and crystallographic orientation on yield strength and their room-temperature plasticity are presented. Similar behavior is expected to occur in other transition-metal carbides and nitrides.

Transition-metal carbides (TMCs) are generally considered to be brittle under uniaxial loading at room-temperature due to limited motion of dislocations [108, 109] and ductile at elevated temperatures (≥ 0.3 T$_m$) [31, 43]. However, as early as 1950s room-temperature plasticity has been reported in bulk single-crystalline B1 – structured ionic solids [35, 36, 89], in poly-crystalline ceramics [39, 40], and more recently in covalently bonded compounds at smaller length scales [37, 58, 110]. For group IV TMCs such as TiC(100) and ZrC(100), microindentation tests indicated that $\{1\bar{1}0\}\langle110\rangle$ slip system is active at room-temperature [111]. High temperature deformation studies of bulk (100), (110), and (111) single-crystals of ZrC revealed that $\{1\bar{1}0\}\langle110\rangle$, $\{1\bar{1}1\}\langle110\rangle$, and $\{001\}\langle110\rangle$ slip systems, respectively are operative with nearly equal critical resolved shear stresses, suggesting the possibility of realizing ductility in poly-crystalline ZrC [31, 44].

In situ uniaxial compression tests carried out inside an electron microscope show that sub-micron-scale ZrC(100) and ZrC(111) crystals deform plastically at room- temperature. I identify $\{1\bar{1}0\}\langle110\rangle$ and $\{001\}\langle110\rangle$ as the active slip systems in ZrC(100) and ZrC(111), respectively. I find that yield strengths of ZrC crystals increase with decreasing size. However, ZrC(111) is found to be softer with a stronger size-dependence than ZrC(100). I also

present calculations via density functional theory (DFT) performed by Dr. Ratsch, and attribute the observed anisotropy to surprisingly facile shear along $\{001\}\langle 110\rangle$ compared to $\{1\bar{1}0\}\langle 110\rangle$.

4.1   ZRC(100) Strength and Plastic Deformation

Sub-micron pillars in the range of $100 - 500$ nm are subjected to uniaxial compression using PicoIndenter 95 holder inside the JEOL 3010 microscope. Regardless of the size, all of the pillars showed shear deformation upon compression. Bright-field TEM images extracted from a video (see Movie "ZrC(100)-S1") recorded during compression of ~ 1-μm-long ZrC(100) pillar with diameter D = 300 nm is presented in Figure 4.1 (A-G). Upon compression of the pillar, yielding occurred via shear. In this experiment, localized deformation and the formation of shear bands near the top of the pillar that is in contact with the diamond punch is evident. In this experiment the pillar is loaded to 100 nm. The first occurrence of shear, labeled 1 in Figure 4.1 (B), at 60 nm is followed by the formation of a surface step (indicated by an arrow in Figure 4.1 (C)) and formation of a second shear plane, labeled 2 in Figure 4.1 (D) at ~ 80 nm. Figure 4.1 (E) shows the post-compression morphology of the pillar. Selected area electron diffraction (SAED) pattern (Figure 4.1 (F)) acquired from the compressed pillar indicates that the pillar retains its single-crystalline B1 (NaCl) structure, i.e. ZrC pillars do not undergo phase transformation and/or twinning due to compression. Figure 4.1 (G) is a representative plot of stress *vs.* displacement measured during *in situ* compression of the ZrC(100) pillar. The points 1 and 2 in the plot (indicated by arrows), correspond to the times at which macroscopic shear events 1 and 2 occurred in the pillar (Figures 4.1 (C-D)). The arrows in (E) and (F) highlight the $\{110\}$ slip planes. In this experiment, the deviation from linearity in the stress-displacement data occurred at an engineering stress of ~ 6.7 GPa. This value corresponding to the point of transition from elastic to plastic deformation is the yield strength, σ_y.
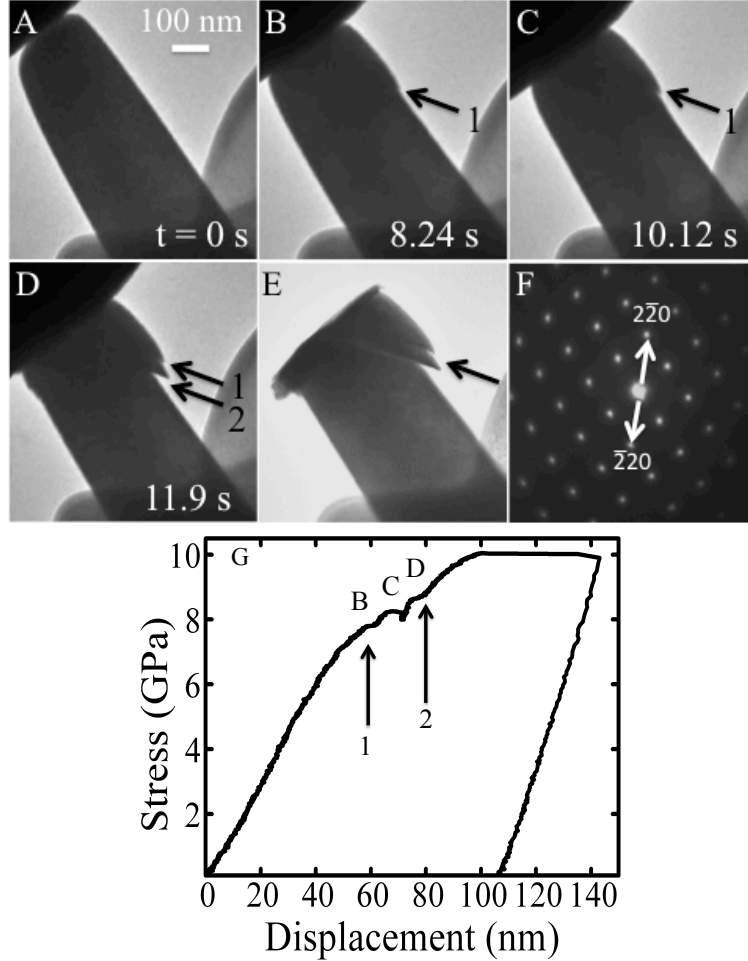
Figure 4.1: A-D) Bright-field TEM images acquired *in situ* during displacement-controlled uniaxial compression of a ZrC(100) pillar with diameter D = 300 nm. E) Bright-field TEM image of the pillar after the compression test. F) Selected area electron diffraction (SAED) pattern acquired along [001] zone axis. G) Plot of engineering stress *vs.* displacement measured during compression of the pillar.

This behavior is typical of all the ZrC(001) pillars that I have tested. Slip system of ZrC(100) is determined to be $\{1\bar{1}0\}\langle 110\rangle$ as shown in Figure 4.2. The solid red and dashed white lines in the TEM image are along the pillar axis, [100], and normal to the slip traces, respectively. The blue line passing through the central (000) spot in the SAED is drawn perpendicular to the red line and hence the diffraction spots lying on this line correspond to the {200} planes. The white dashed line superposed on the SAED pattern, is parallel to the

line in TEM image and intersects, within the experimental uncertainties of $\sim 4°$, the $(2\bar{2}0)$ spot highlighted by a yellow cross. Based upon these results, the slip plane orientation is identified as $\{1\bar{1}0\}$.
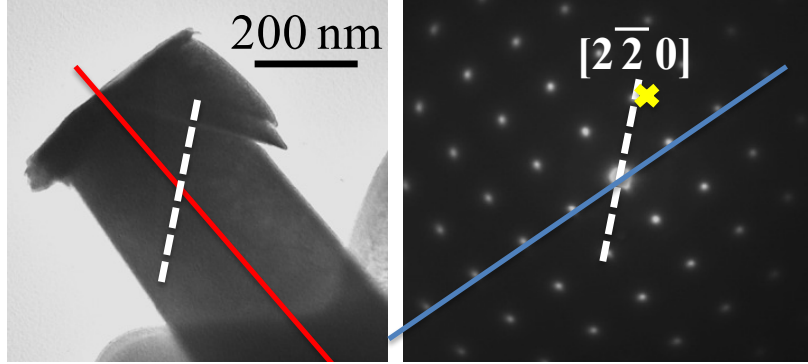
Figure 4.2: Determination of $\{1\bar{1}0\}$ as the orientation of the slip plane

It is likely that $\langle110\rangle$, the direction with the shortest repeat distance in NaCl lattice, is also the slip direction in our experiments. This is plausible since the resolved shear stress during compression along $[100]$ is highest for the $\{1\bar{1}0\}\langle110\rangle$ slip systems and consistent with previous room-temperature microindentation tests conducted on bulk group IV (100)-oriented transition-metal carbide single-crystals [41, 112]. I have not observed any dislocations during post-compression analysis. It is believed that due to the confined volume of the pillars dislocations might have left the pillars upon slip. Slip traces are shown in Figure 4.3 (A-B) after post-compression analysis of a ZrC(100) pillar.
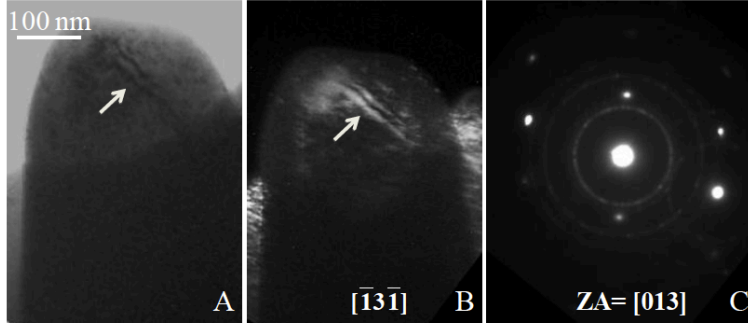
Figure 4.3: A) Bright- and B) dark-field TEM images obtained from a ZrC(100) pillar with D = 280 nm after shear deformation. The dark-field image is obtained using $[13\bar{1}]$ reflection. C) the SAED pattern of the pillar along [013] zone axis, indicating that the pillar retains its single-crystalline structure post-compression. Slip traces (highlighted by the arrows) indicate that the slip plane orientation is {110}.

4.2 ZrC(111) Strength and Plastic Deformation

A completely different behavior is observed for ZrC(111) sub-micron pillars. Pillars do not exhibit slip and deform via dislocation motion and tangling. Figure 4.4 (A-D) are representative bright-field TEM images extracted from a video (see Movie "ZrC(111)-S2") recorded during the compression of $\sim$ 0.55-μm-long ZrC(111) pillar with D = 180 nm. Based on the *in situ* TEM videos, nucleation, motion, and tangling of dislocations within the pillars is evident with no sign of slip traces. Figure 4.4 (E) is a post-compression image of the same pillar, which shows that the pillar length decreased by $\sim$ 60 nm while its diameter increased by $\sim$ 20 nm. The SAED pattern in Figure 4.4 (F), acquired from the ZrC(111) pillar after the test, indicates that both the crystal structure and the crystallinity of the pillar are unaffected by the compression. Figure 4.4 (G) is a plot of the stress *vs.* displacement data acquired during compression of the pillar.

Non-linear variation in displacement with applied load and the absence of any abrupt changes ("pop-ins"), associated with slip, consistent with plastic deformation via dislocation motion is clear rom the plot.
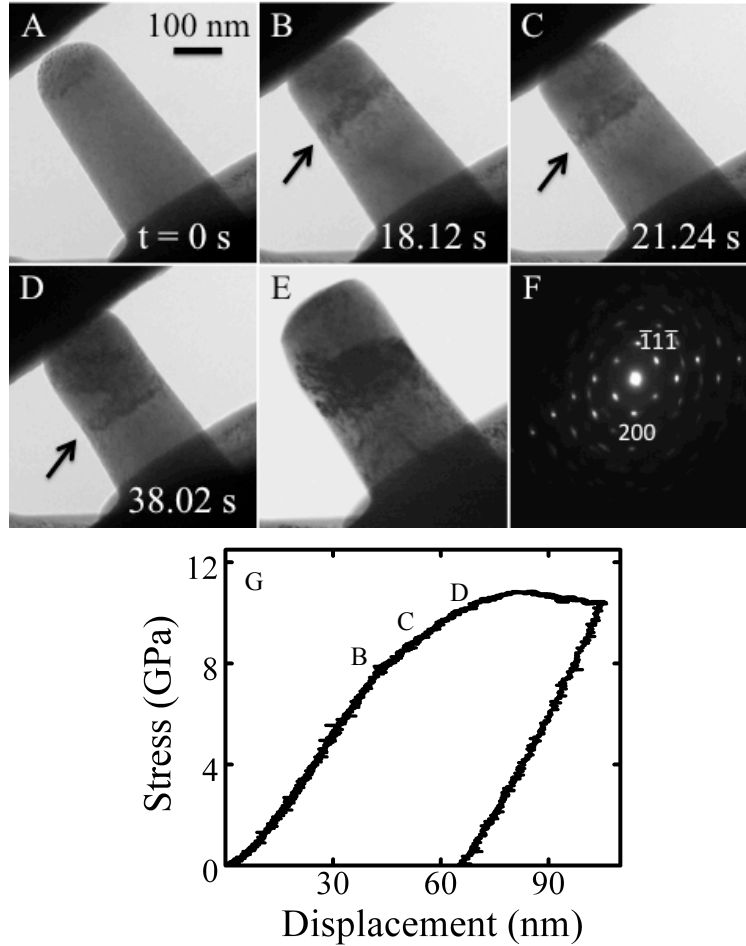
Figure 4.4: A-D) Bright-field TEM images extracted from a video recorded during uniaxial compression of a D = 180 nm ZrC(111) pillar up to 100 nm. The contrast changes visible in the images, highlighted by the arrows, are due to the nucleation and motion of dislocations. E) Post-compression TEM image of the pillar. F) SAED pattern of the compressed pillar in Fig. 1E along [011] zone axis. G) Representative plot of engineering stress *vs.* displacement

This behavior is typical of all the ZrC(111) pillars that tested in this study. To gain a better insight into plastic deformation mechanism and active slip system for ZrC(111), post-compression analysis is conducted. Since the resolved shear stress on $\{1\bar{1}0\}\langle110\rangle$ slip systems is zero during loading along [111], the observed plastic deformation must be due to the operation of other slip systems such as $\{001\}\langle110\rangle$ and/or $\{1\bar{1}1\}\langle110\rangle$. Based on the post-compression TEM analysis (Figure 4.5) it is concluded that $\{001\}\langle110\rangle$ slip systems are

the dominant active system during compression of the ZrC(111) pillars.
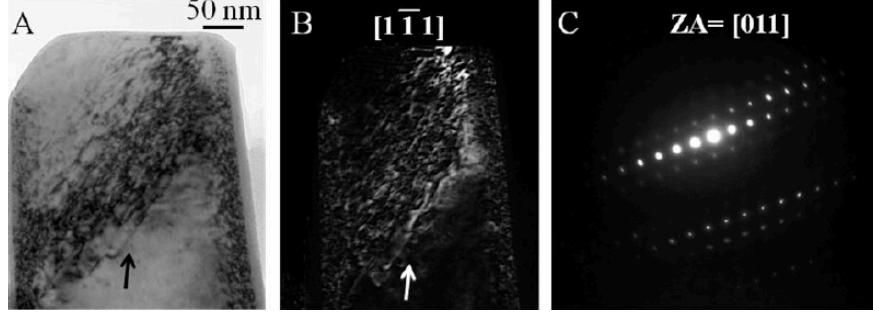
Figure 4.5: A) Bright-and B) dark-field TEM images of a ZrC(111) pillar with D = 260 nm acquired post-compression test. The dark-field image is obtained using $[1\bar{1}1]$ reflection. C) the SAED pattern of the pillar along [011] zone axis. Arrows highlight the dislocation lines.

The darker contrast bands visible in Figure 4.5 (A-B) are oriented along $\sim 55°$ with respect to [111] and are due to dislocations in {001} planes (slip traces shown below). Based on $\vec{g} \bullet \vec{b}$ invisibility criterion and imaging using two known reflections $[1\bar{1}1]$ and $[\bar{1}\bar{1}1]$, I determine the slip direction as [101]. Hence, it can be concluded that the family of slip systems $\{001\}\langle 110\rangle$ is operative at room-temperature in ZrC(111) pillars.

Room-temperature plasticity in ZrC, which is commonly considered to be brittle, can be attributed to the small sizes of the crystals. Studies have shown that the compressive stress required to fracture increases with decreasing size of a brittle material and that there exists a threshold size (compared to the size of the diamond punch) below which yielding, rather than brittle fracture, is favored [41]. In our compression tests, D $\leq$ 500 nm for all the ZrC pillars and they are all smaller than the diamond punch (~ 3 μm). Moreover, the pillars are single-crystals, which at sub-micron-scale compared to bulk are likely to have a lower density of surface and bulk defects that could act as stress risers and induce fracture. Hence, the pillars can withstand higher stresses without failure. At sufficiently high stresses, nucleation and motion of dislocations occur, leading to plastic deformation. Figure 4.6 compare two pillars of ZrC shown above side by side for better observation of the difference in their deformation mechanism; shear deformation *vs.* dislocation tangling.
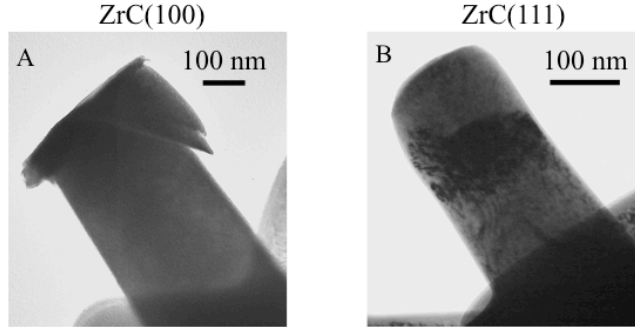
Figure 4.6: A) ZrC(100) and B) ZrC(111) pillars post-compression

4.3 Size-Dependence of Strength

To gain better insights into the plastic deformation behavior in ZrC, uniaxial compression tests on 18 ZrC pillars of D between 100 and 500 nm are carried out. The engineering stress *vs.* strain behavior of different size ZrC pillars is illustrated in Figure 4.7 (A-B). For a given crystallographic orientation, all the pillars exhibit similar deformation behavior. And, for both orientations, the maximum stresses withstood by the pillars before failure increase with decreasing D.
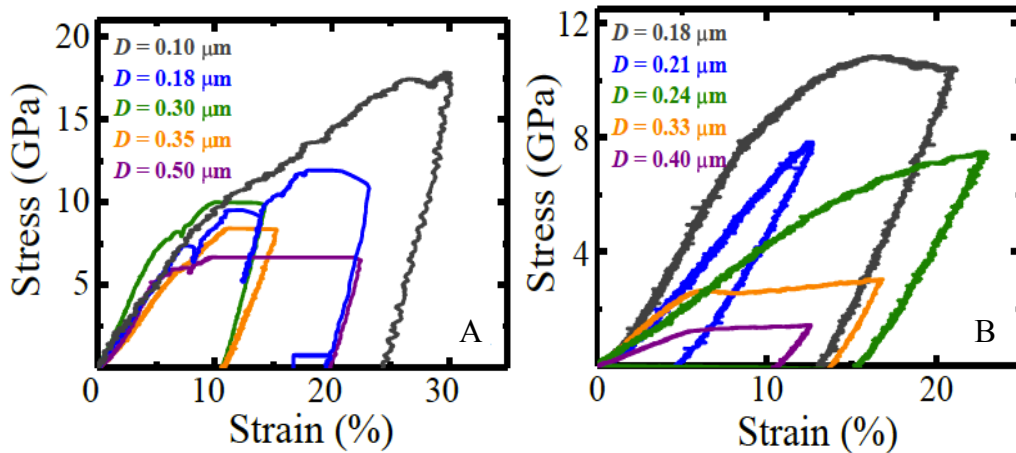
Figure 4.7: Plots of engineering stress *vs.* engineering strain for A) ZrC(100) and B) ZrC(111) pillars in the size range of D = 100 − 500 nm. Experiments are run in displacement-controlled mode and hence, the maximum strain does not correspond to fracture.

To determine the yield points and σ_y values, stress-displacement data of all the pillars in log-log scale is plotted. By using the least-squares fits to the data, the transition point from linearity – elastic to plastic – defined as yield point and its value is extracted. Figure 4.8 shows the process of extracting the σ_y values for one of the pillars. The red and green lines are least-squares fits to the data. Their intersection leads to the yield point (deviation from linearity) and the value of yield strength σ_y. Similar procedure is used to extract σ_y for the rest of the tested pillars.
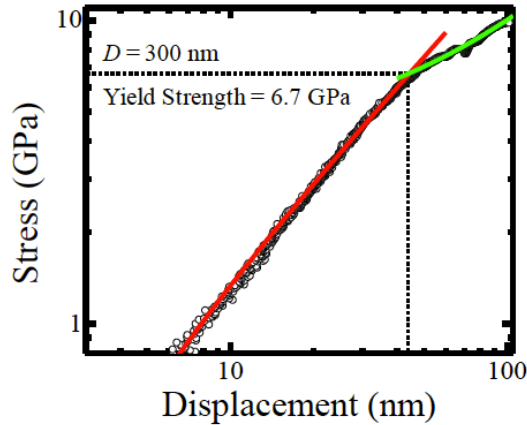
Figure 4.8: Log-log plot of stress *vs.* displacement data for D $=$ 300 nm pillar shown in Figure 4.1(G)

Upon obtaining the σ_y values for all the pillars (values between $\sim$ 0.5 and 9 GPa), log-log plot of σ_y *vs.* D for all the ZrC pillars in both [100] and [111] orientations is illustrated in Figure 4.9. Although there is no data on room-temperature yield strength for ZrC crystals, extrapolation of high-temperature σ_y values to room-temperature suggests that the observed range of σ_y values is plausible. It is indicated that yield strengths of both ZrC(100) and ZrC(111) pillars increase with decreasing D. Similar size-dependences in σ_y(D) have been observed in metals, bulk metallic glasses, covalent and ionic crystals [35, 113] and are commonly attributed to 1) dislocation starvation, a process where defect density decreases with the size of the crystal, and 2) dislocation truncation in small samples leading to increased flow stress. In non-metallic crystals such as Si and LiF, enhanced dislocation nucleation, mobility, shielding, and limited dislocation multiplication rates at small length scales have

also been suggested as contributing factors to variation in σ_y with D [1, 80, 88].
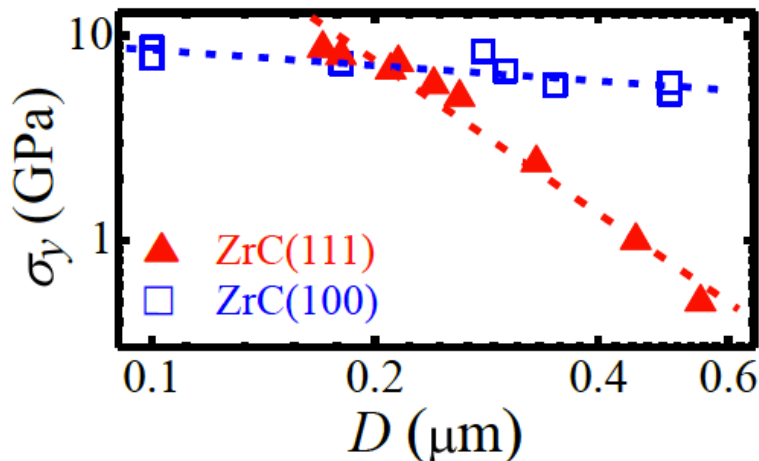
Figure 4.9: Log-log plot of yield strength *vs.* diameter for ZrC(100) ($\square$) and ZrC(111)($\blacktriangle$) pillars. The dashed lines are linear least-squares fit to the data.

Yield strength σ_y for ZrC(111) varies steeply from ~ 0.5 GPa to ~ 9 GPa with D. In comparison, σ_y for ZrC(100) changes from ~ 5 GPa to ~ 9 GPa with D; and ZrC(111) pillars are softer than ZrC(100) pillars. Both these results are opposite to what has been reported for similar-structured ionic crystals such as LiF and MgO, where σ_y in [100] orientation exhibits stronger size-dependence than σ_y for [111] orientation [35, 89]. For a given crystal orientation, σ_y (D) can be attributed to a combination of limited dislocation lengths, densities, and multiplication rates, enhanced flow stress, and higher dislocation mobilities [114]. And, the effect of size on σ_y is more (less) pronounced in crystals with smaller (higher) bulk yield stresses [35].

Furthermore, strain-hardening exponents (n) and strain-hardening coefficients (K), measures of dislocation multiplicity and interactions, for each pillar are extracted. It appears that both n and K scale with D for ZrC(111) but vary little for ZrC(100) pillars. To this purpose, true stress (σ_T) and true strain (ε_T) values are first calculated from the load-displacement data in the range between the yield point and up to 20% engineering strain. Both n and K are then extracted by fitting σ_T *vs.* ε_T data with the equation of the form $\sigma_T = K\varepsilon_T^n$. Figure 4.10 depicts plots of n and K *vs.* diameter for both ZrC(100) and ZrC(111) pillars.
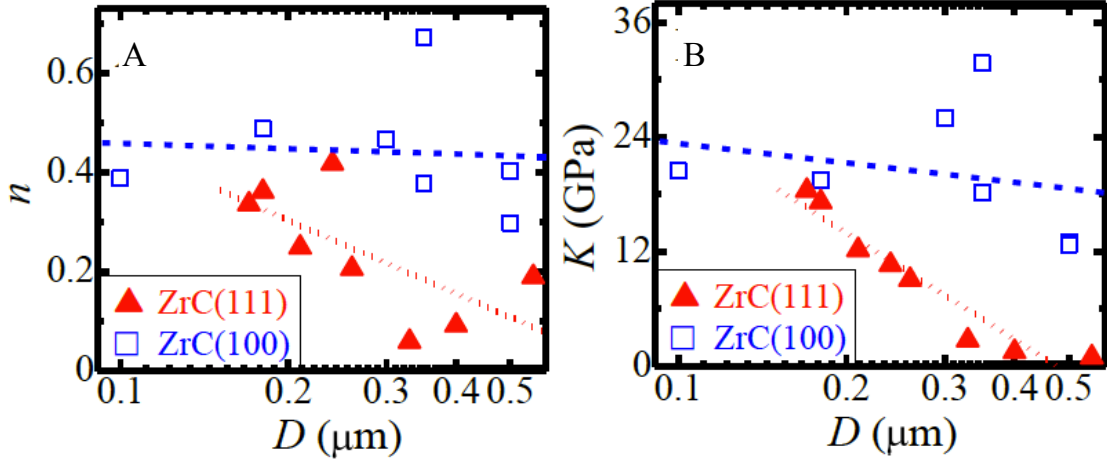
Figure 4.10: Semi-log plots of A) strain-hardening exponent n and B) strain-hardening coefficient K as a function of D for ZrC(100) ($\square$) and ZrC(111) ($\blacktriangle$) pillars. Although data is scattered, but both n and K vary markedly with D for ZrC(111) than for ZrC(100).

In order to understand the origin of this anomalous orientation-dependent plasticity in ZrC, density-functional theory (DFT) calculations measure uniaxial stresses required to deform stoichiometric ZrC single-crystals and energy barriers associated with slip and shear along the primary slip systems.

4.4 DFT Calculations

Ideal strengths of ZrC during uniaxial compression as a function of crystallographic orientation are calculated as follows. The slab is incrementally strained in tension or in compression along the z direction and the total energy E_{total} of the system is determined with DFT at each strain. (In these calculations, the lattice is not relaxed along x- and y- directions). Normal compressive stresses are then calculated as $\sigma_{ij} = \dfrac{1}{\nu} \dfrac{\partial E_{\text{total}}}{\partial \varepsilon_{ij}}$, where ν is the volume of the supercell, and ε is the 3×3 strain tensor. Both analytical as well as numerical evaluation of the stress as implemented in FHI-AIMS are used. The data presented here is obtained from the analytical evaluation. Figure 4.11 shows stress *vs.* strain data calculated for uniaxial compression of ZrC(100) and ZrC(111) crystals. It is found that uniaxial compression of ZrC

56

along [111] is easier compared to compression along [100]. For example, ideal stress required to compress ZrC(111) by 10% is ~ 19 GPa. In comparison, ~ 80 GPa is required to compress ZrC(100) by the same amount. That is, ZrC(111) is softer under uniaxial compression than ZrC(100). The theoretical stresses, although higher in pristine perfect condition, are over $10\times$ higher than the measured values, and shows that the DFT results are in qualitative agreement with the experimental data.
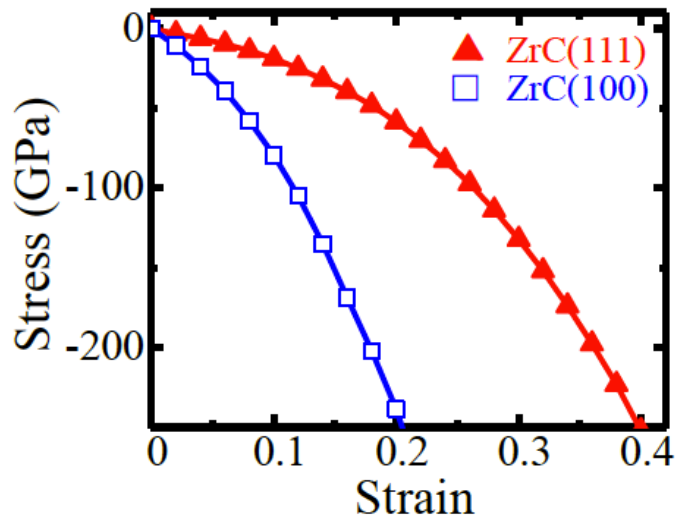
Figure 4.11: DFT calculation of uniaxial compressive stress *vs.* lattice strain for ZrC(100) (□) and ZrC(111) (▲) crystals

4.5   Discussion

In this study I find that sub-micron-scale ZrC crystals undergo plastic deformation and that their orientation- and size- dependent variations in yield strengths is different from what is generally expected for NaCl-structured compounds. In transition-metal carbides and nitrides, a mixture of metallic, ionic, and covalent bonds control their mechanical properties. The nature and relative strengths of metal-metal and metal-carbon (or nitrogen in case of nitrides) bonds, which vary with the valence electron concentration in the lattice [115], covalent radii of the metal cations, and crystallographic orientation determine the most

favorable glide planes, overall ductility and hardness of these compounds [116].

The primary mode of deformation in ZrC(100) pillars is shearing while dislocation tangling leads to more uniform plasticity in ZrC(111) pillars. It is also observed that the mechanical response of ZrC(111) is more sensitive than ZrC(100) to defects (e.g., anion vacancies and dislocations), and hence σ_y for ZrC(111) varies strongly compared to σ_y for ZrC(100). Using DFT calculations, the observed plasticity is attributed to relatively easy deformation along $\{001\}\langle110\rangle$ rather than along the commonly expected $\{1\bar{1}0\}\langle110\rangle$ slip systems. Results on ZrC sub-micron pillars presented here indicate that multiple slip systems can be active at room-temperature and plasticity could be expected in hard, refractory transition-metal carbides. Although DFT offers some insights into the mechanical response of ideal, defect-free, ZrC crystals, but molecular dynamics simulations and multi-scale modeling of dislocation dynamics are required to fully understand the electronic origins of plastic deformations, which is outside the scope of this work.

CHAPTER 5

Dislocation Glide-Controlled Plasticity
in Single-Crystalline 6H-SiC

In this chapter result of room-temperature uniaxial compression test on single-crystalline 6H-SiC sub-micron pillars oriented at 45° with respect to the basal plane normal (Φ_{45}), their deformation mechanisms and effects of size-scale on yield strength are presented. For comparison behavior of Φ_0 pillars where loading is along $\langle 0001 \rangle$ direction are also investigated. High-resolution scanning TEM (STEM) images acquired by abberation-corrected TEAM 0.5 microscope confirming the lattice structure and absence of phase transformation is also included.

The critical load-bearing components of many modern structures are often constructed from metallic alloys having lower strengths than their ceramic counterparts. This design compromise is often driven by a need for component reliability, a trait that is generally superior in metallic alloys due to their ability to deform plastically at room-temperature. The availability of higher strength materials with enhanced ductility would significantly boost the performance of critical load bearing components and enable advanced next-generation technologies. This, however, is a challenge and requires a fundamental understanding of the factors influencing mechanical properties of materials. In case of metals, recent studies have helped identify the role of crystal size and microstructure on their mechanical properties. For higher strength materials such as SiC with great application as a structural ceramic and a semiconductor material, while most studies focused on determination of the thermomechanical properties [47–49,51] or indentation [52,53,55], relatively little is known concerning their plastic deformation at room-temperature [57–59]. Here, I show that small (< 300 nm in diameter) SiC single-crystals deform plastically at room-temperature under a compressive

load, exhibiting a long sought combination of mechanical properties, high yield strength (> 7.8 GPa) and considerable ($\sim 10\%$ strain) plastic flow before failure, indicative of high ductility.

From the mechanical responses of SiC pillars oriented at $45°$ with respect to $\langle 0001 \rangle$ and along $\langle 0001 \rangle$, hereafter referred to as Φ_{45} and Φ_0 respectively, subjected to uniaxial compression, I show that plastic flow in SiC is due to slip on the basal planes. These findings are consistent with *ab initio* theoretical analysis (DFT calculations and MD simulations), which suggests that plastic slip on the basal plane at room-temperature is energetically most favorable and will occur by full dislocation glide on the shuffle set.

5.1 Plastic Deformation of 6H-SiC(Φ_{45}) Pillars

6H-SiC sub-micron pillars in the size range of $170 - 280$ nm at an orientation $45°$ with respect to $\langle 0001 \rangle$ subjected to uniaxial compression test using PicoIndenter 95 inside JEOL 3010 show dislocation mediated plastic deformation. Figures 5.1(A-G) show representative bright-field TEM images (extracted from Movie "6H-SiC(Φ_{45})-S3"), electron diffraction pattern, and stress-displacement data recorded during uniaxial compression of a Φ_{45} oriented, $\sim$ 600 nm long, 6H-SiC pillar with diameter D = 180 nm. In this experiment, the pillar is compressed until a nominal displacement of 100 nm after which the load is released. During compression, the initial stress-displacement response is linear, characteristic of elastic deformation, up to a point beyond which the displacement increases non-linearly with applied stress indicative of plastic flow as shown in Figure 5.1 (G). The change in the unloading slope is most likely due to the adhesion stress effect upon release of the diamond tip. In this experiment, the deviation from linearity occurred at an engineering stress of ~ 7.8 GPa. The TEM images [for example, Figure 5.1 (B)] corresponding to this transition reveal the generation of dislocations from the contact point between the pillar and the indenter tip. After this initial event, additional bursts of dislocations are observed in the specimen. These events, highlighted by arrows labeled 1 and 2 in Figures 5.1 (C, D, and G), result in abrupt changes visible in the stress-displacement curve. Figure 5.1 (E) is the image of the pillar

obtained after compression. Selected area electron diffraction (SAED) pattern (Figure 5.1 (F)) acquired from the pillar indicates that its crystallinity and crystal structure are retained.
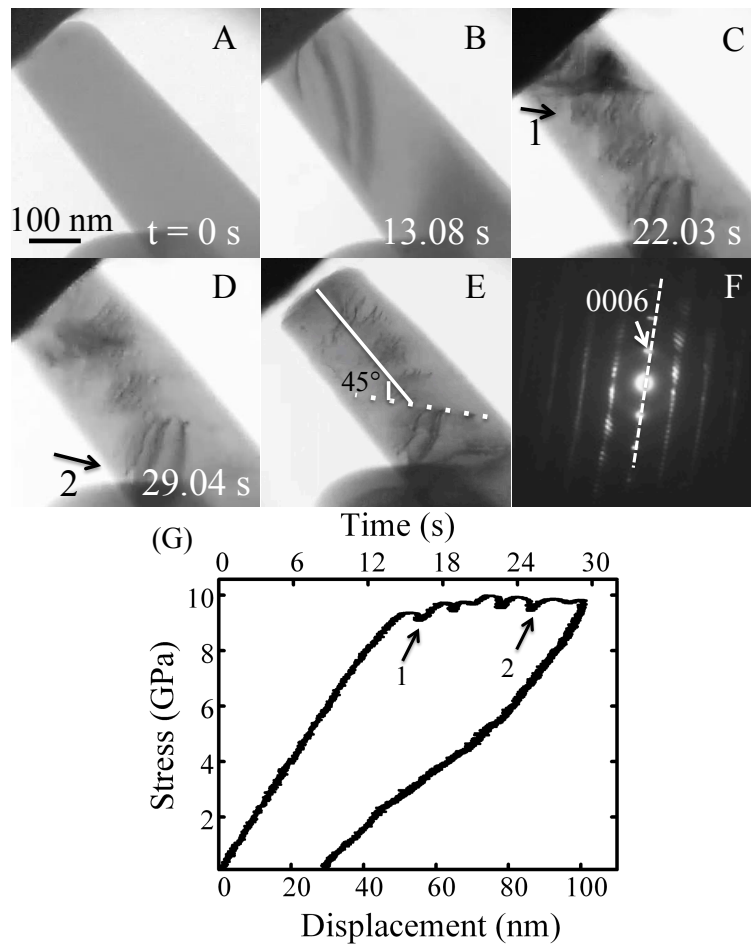
Figure 5.1: A-D) Bright-field TEM images acquired *in situ* during displacement-controlled uniaxial compression of a single-crystalline 6H-SiC pillar oriented at 45° with respect to $\langle 0001 \rangle$ referred to as Φ_{45}. The pillar diameter is D = 180 nm. E) Post-compression morphology of the pillar. F) Selected area electron diffraction pattern obtained from $[11\bar{2}0]$ zone axis. G) Engineering stress *vs.* displacement plot showing multiple displacement bursts, highlighted by arrows 1 and 2, corresponding to slip on {0001} planes.

The dotted line passing through the slip traces on the TEM image and the dashed line passing through {0001} in the reciprocal space in SAED are perpendicular indicating that {0001} is the orientation of the slip plane. Also the angle between the dotted line (slip plane

61

orientation {0001}) and the solid line (orientation of the pillar and the loading direction) is indicated as 45°.

This behavior is a typical of all the pillars tested in this size range. Pillars smaller or larger than this range have not been investigated due to difficulties in pillar preparation via FIB and difficulties in alignment (avoiding bending). Post-compression analysis using a double tilt holder inside JEOL 3010 show slip bands along the basal direction; as an indication that basal slip is the dominant deformation mechanism in the tested pillars. Bright-field and dark-field images acquired post compression shown in Figure 5.2 (A-C) acquired at $[01\bar{1}0]$ zone axis indicate that the basal slip $\{0001\}\langle11\bar{2}0\rangle$ is likely the dominant mode of deformation. Using the $\vec{g}\bullet\vec{b}$ invisibility criteria with two known reflections $[2\bar{1}\bar{1}6]$ and $[0006]$, it is suggested that dislocations have $\vec{b} = [11\bar{2}0]$ expected to operate in 6H-SiC crystal [117]. It should be mentioned that a complete the $\vec{g}\bullet\vec{b}$ analysis which requires tilting to three different zone axes is not achievable given the geometry limitation of the sample (pillar *vs.* plane view sample). Formation of slip bands that extend to the surface of the pillar and create surface steps are highlighted with arrows in Figure 5.2 (A). Diffraction patterns obtained after deformation show some streaks that are most likely due to a deformation-induced misorientation during the mechanical testing.
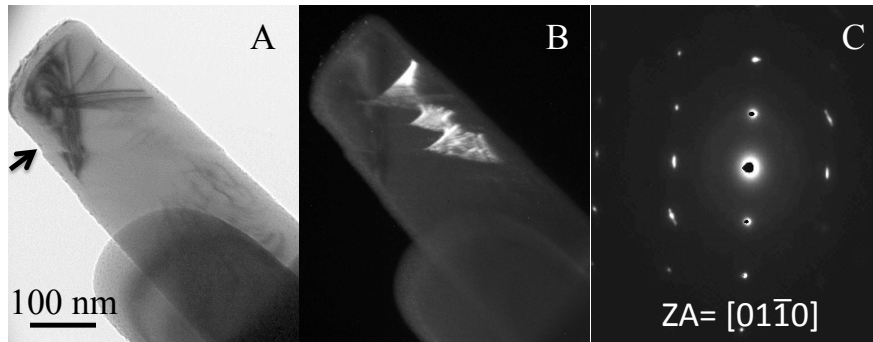
Figure 5.2: A-C) Bright- and dark-field TEM images and SAED patterns acquired post–compression of D = 180 nm pillar. Based on invisibility $\vec{g}\bullet\vec{b}$ criteria and using two known reflections $[2\bar{1}\bar{1}6]$ and $[0006]$, the slip direction is determined as $[11\bar{2}0]$.

It should be noted that the unloading portion of the stress-displacement curve in Figure 5.1 (G) is nonlinear. Such a deviation from linearity in the unloading curve, referred to as knee or elbow, has been observed during indentation of silicon and attributed to reversible pressure-induced phase transformation. Nanoindentation studies on silicon show that the existence of a so-called "elbow" or "pop out" in the unloading curve of the load-displacement plot is due to phase transformation from diamond cubic (Si-I) to metallic body-centered tetragonal structure or β-tin structure (Si-II) under indentation pressure of around 11 GPa. The transformation is known to be reversible back to the diamond structure at pressures below 8 GPa. This pressure induced phase transformation has been captured in the mechanical response during nanoindentation and proved with Raman spectroscopy for crystalline silicon [118–121].

Polytypism caused by a one-dimensional disorder in SiC allows different stacking sequences. Some of the most common polytypes of SiC are (2H), (3C), (6H), and (15R) as discussed in Chapter 2. Polytype transformation can occur in bulk SiC subjected to mechanical loading at temperatures above 800 °C [122–124]. In order to check for any such phase transformations occurring within the 6H-SiC Φ_{45} pillars, detailed high-resolution TEM characterizations of the deformed pillars are carried out.

5.1.1   TEM Images-Titan X

High-resolution images are acquired with Titan X microscope operated at 300 kV after thinning the D = 180 nm pillar with Ga^+ ion in the FEI 235 FIB dual beam system operated at 10 kV and cleaning with Ar^+ in the Nanomill 1040 operated at 2 kV and 150 μA at $[11\bar{2}0]$ and $[01\bar{1}0]$ zone axis around the area marked with arrow (Figure 5.3 (A)) to confirm the crystallinity and 6H symmetry characteristic of 6H-SiC(Φ_{45}) pillar [123, 124].
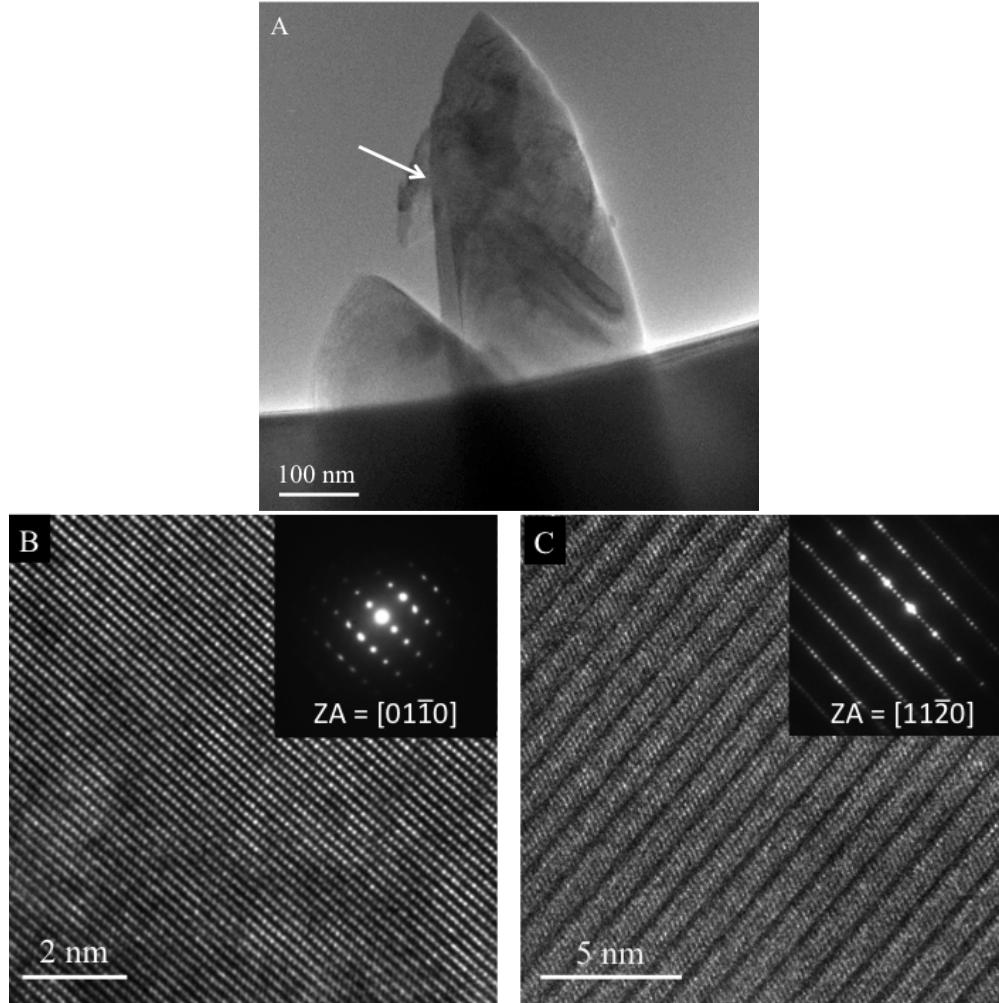
Figure 5.3: A) Bright-field TEM image of the deformed D = 180 nm pillar, B) high-resolution TEM image at zone axis $[01\bar{1}0]$ and C) high-resolution TEM image at zone axis $[11\bar{2}0]$. The insets are corresponding diffraction patterns.

5.1.2 Scanning TEM (STEM) Images-TEAM 0.5

To further investigate any phase transformation, high-angle annular dark-field (HAADF) high-resolution scanning TEM (STEM) images are acquired with TEAM 0.5 microscope operated at 300 kV after thinning the D = 180 nm 6H-SiC (Φ_{45}) pillar with Ga^+ ion in the FEI FIB 230, cleaning with Ar^+ in the Nanomill 1040 operated at 2 kV and 150 μA and plasma cleaning for 60 s.

Alternate zigzag symmetry characteristic of 6H-SiC structure around the slip trace is observed as labeled in Figure 5.2 (A) at $[11\bar{2}0]$ zone axis. However, no sign of structural phase transformation is identified. A lattice distortion around the slip trace (deformed area) is detected as a result of plastic deformation. The lattice rotation phenomenon is expected to occur in single-crystalline materials subjected to mechanical loading [125].
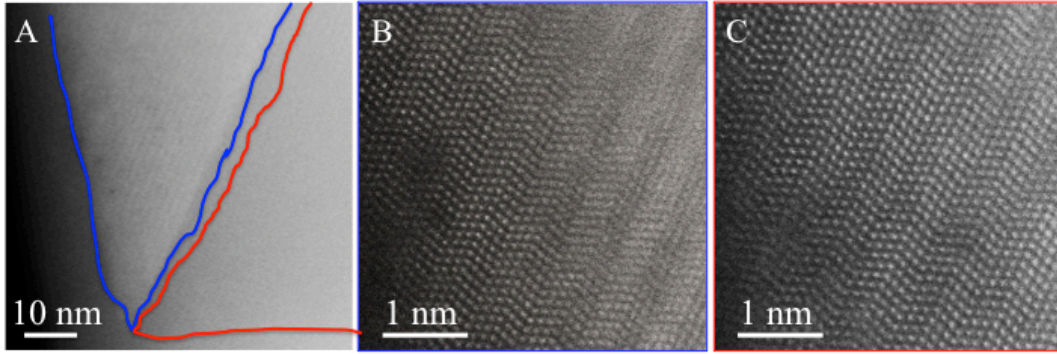
Figure 5.4: A) Higher-magnification scanning TEM images from the area around the slip trace of the deformed D = 180 nm pillar shown in Figure 5.1. High-resolution STEM images of the regions B) above and C) below the slip trace outlined by blue and red, respectively.

In order to determine the extent of lattice distortion in the deformed pillar, a combination of convergent beam electron diffraction (CBED) and high-angle annular dark-field (HAADF) STEM techniques is used. The STEM image shown in Figure 5.4 (B) is from the area above the slip trace and is obtained with the center of the Ewald sphere at a position labeled x_1 in Figure 5.5 (A) and the zone axis along $[11\bar{2}0]$. Under this imaging condition, the area below the slip trace is found to be off the zone axis and the center of the Ewald sphere is shifted in the reciprocal space to a new position labeled x_2 in Figure 5.5 (B); i.e. the regions above and below the slip trace are not on the same plane. By tilting the sample by 43 mrad, the area below the slip trace is brought to the same zone axis and the STEM image shown in Figure 5.4 (C) is obtained. The fact that sample tilting is required to orient the two regions around the slip trace to the same zone axis and to obtain high-resolution STEM images is a direct evidence of distortion in the crystal lattice during uniaxial compression.
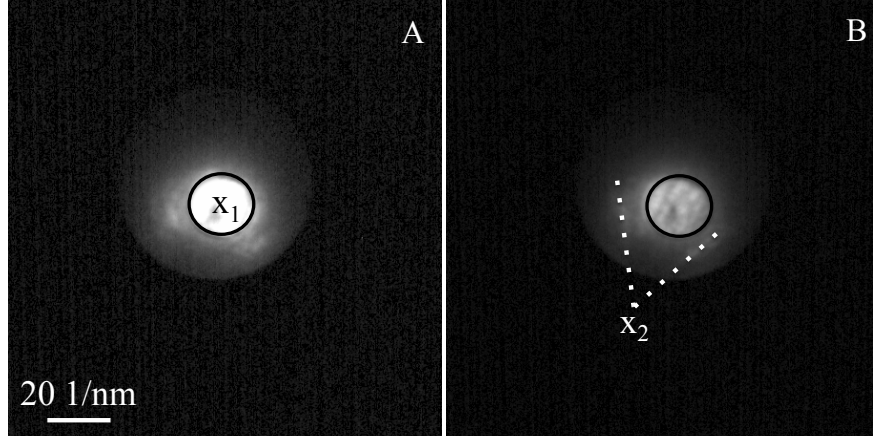
Figure 5.5: Convergent beam electron diffraction patterns acquired to capture high-angle annular dark-field (HAADF) high-resolution STEM images for characterization of plastical-ly-deformed pillar shown in Figure 5.4. Centers of the Ewald spheres are at positions A) x_1 (above) and B) x_2 (below) the slip trace labeled with arrow in Figure 5.2 (A). The zone axis is along $[11\bar{2}0]$.

5.1.3   Effect of Pillar Diameter on Yield Strength

Total of six pillars with D = 170 nm – 280 nm are subjected to uniaxial compression test in this study. Engineering stress *vs.* displacement for all the pillars is shown in Figure 5.6. For the Φ_{45} pillars, σ_y values between 7.8 and 14.3 GPa for the different pillars is achieved, but σ_y did not vary systematically with D. Although the stress-displacement responses of these pillars are qualitatively similar, the extent of plastic hardening, the elastic to plastic transition point (i.e. the yield point, σ_y), and the loading/unloading curve slopes vary from pillar to pillar due to differences in alignment or slight bending of the pillars. By using the least-squares fits to the data, the transition point from linearity – elastic to plastic – defined as yield point and its value is extracted. Figure 4.8 in Chapter 4 explains this in more details.
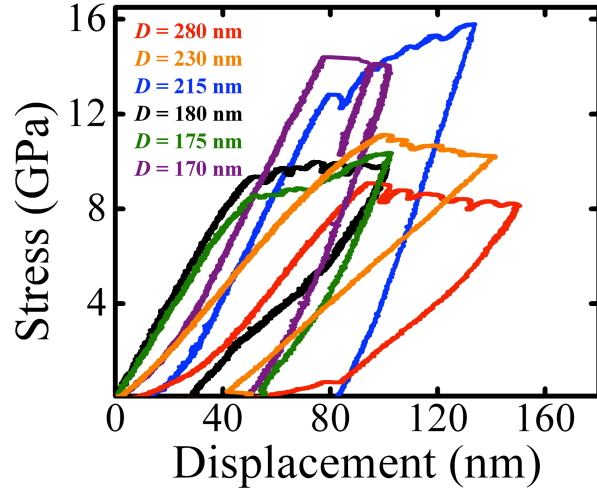
Figure 5.6: Plots of engineering stress *vs.* displacement for a total of six 6H-SiC (Φ_{45}) pillars with D = 170 nm – 280 nm

5.2   Plastic Deformation of 6H-SiC(Φ_0) Pillars

In comparison, Φ_0 pillars, i.e. 6H-SiC(0001) pillars compressed uniaxially along do not undergo plastic deformation but fail catastrophically via brittle fracture. There is a strong effect of crystallographic orientation on the behavior of 6H-SiC pillars. In these Φ_0 pillars, the displacement increases steadily with applied stress up to the point of failure, which occurs abruptly at $\sim$ 15 - 22 GPa. The lack of any contrast changes in the TEM images acquired during the test suggest that structural defects such as dislocations are absent, consistent with the brittle fracture of the sample. Figure 5.7 (A-E) are representative bright-field TEM images extracted from a video (see Movie "6H-SiC(Φ_0)-S4") recorded during uniaxial compression of $\sim$ 800 nm-long 6H-SiC pillar with D = 260 nm. A high compressive strength of $\sim$ 20 GPa is reached prior to brittle fracture.

Here the ductility (brittleness) of Φ_{45} (Φ_0) pillars is attributed to the activation (suppression) of slip on the basal planes at room-temperature. Critical resolved shear stress (CRSS) is zero in this orientation and basal slip is suppressed. Non-basal slip: pyramidal or prismatic is not operative due to much higher needed CRSS. In an attempt to further characterize the
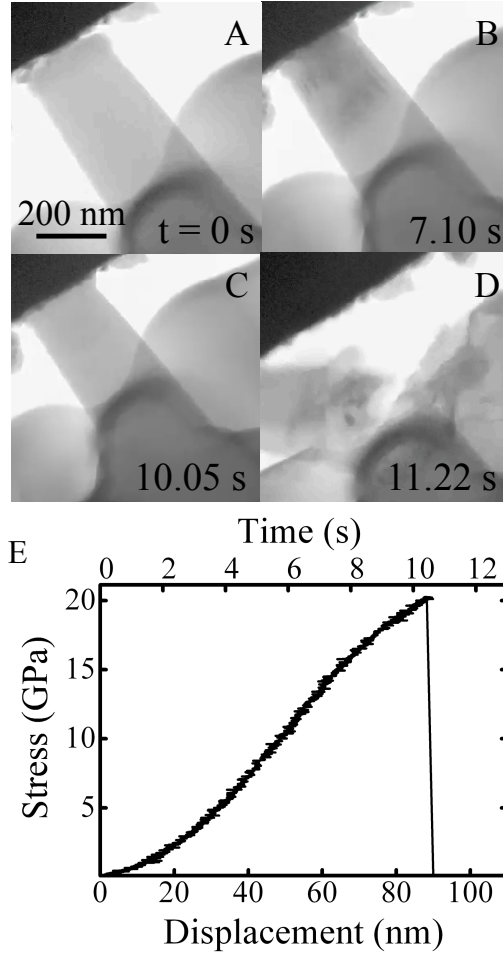
Figure 5.7: A-D) Bright-field TEM images acquired *in situ* during displacement-controlled compression of D = 260 nm pillar loaded parallel to basal plane normal $\langle 0001 \rangle$. In this experiment, the pillar is loaded to 100 nm. No sign of plasticity is observed and brittle fracture occurs at around 20 GPa. E) Engineering stress *vs.* displacement plot obtained during the compression of the pillar.

deformation mechanisms that enable the sustained plastic flow in the 6H-SiC submicron Φ_{45} pillars, atomistic modeling and analysis through collaborative work with Prof. Warner and graduate student Mr. Leung are presented. Specifically, molecular dynamics (MD) simulation of the 6H-SiC submicron pillar under compression is investigated to provide insight into the plastic slip process. Acknowledging the uncertainty in the empirical potential of the MD simulation, the generalized stacking fault (GSF) energy curves associated with the possible

68

slip systems are further computed with electronic structure calculations. This multifaceted approach is able to predict the most probable slip system, and the corresponding critical stress for dislocation nucleation.

5.3 MD Simulations and DFT Calculations

The MD simulations predict that the critical compressive stress required for dislocation nucleation is 31 GPa. Following nucleation, the dislocation eventually glides to the surface and forms an atomic step. The shear deformation occurred in the form of slip bands on the more easily-shearable atomic planes by higher von Mises strain. Based on these results, 6H-SiC Φ_{45} pillars, subjected to uniaxial compression, can undergo plastic deformation via slip by dislocation nucleation and glide on the shuffle set of basal planes.

DFT calculations are used to determine energetically the most favorable pathways for dislocation glide. Both the stacking fault energies (E_{GSF}) and gradient of stacking fault energies (dE_{GSF}/dx) as a function of (x/b), x is the rigid displacement and b is the Burgers vector, are considered to investigate the resistance to dislocation glide. For this purpose, four different possible slip systems involving two sets of basal planes, the shuffle and the glide sets, and two slip directions; $\langle 1120 \rangle$ and $\langle 1100 \rangle$, using a crystal with periodic boundary condition in the in-plane directions and the basal planes as the top and bottom surfaces are examined. For all the four slip systems, the E_{GSF} increased monotonically with x and the maxima is reached at $x = b/2$, whereas the maxima in dE_{GSF}/dx (i.e. τ_0) is observed at $x = b/4$. From the data, it is found that energetically the most favorable (lowest τ_0) and unfavorable (highest τ_0) slip systems are the basal slip on the shuffle set along $\langle 1100 \rangle$ and basal slip along $\langle 1120 \rangle$ on the glide set. The second most favorable slip path, i.e., the path with the second lowest τ_0, is on the shuffle set along $\langle 1120 \rangle$. The third favorable basal slip is on the glide set along $\langle 1100 \rangle$ that involves dissociation of the dislocation into two partials along $1/3[1\bar{1}00] + 1/3[10\bar{1}0]$ separated by a stable stacking fault. DFT calculations of dE_{GSF}/dx vs. (x/b) predict that the ideal shear stress (the lowest τ_0) associated with nucleation of a dislocation on the shuffle set of the basal plane from a surface is ~ 33 GPa.

The uniaxial compressive stress needed to nucleate dislocations from the free surface on the shuffle set along $\langle 1100 \rangle$ is ~ 66 GPa (Schmid factor is $1/2$ for this slip system) and more than twice the stresses obtained from MD simulations. Given that both MD and DFT calculated stresses for dislocation nucleation are up to an order of magnitude higher the experimentally determined σ_y, it is suggested that the observed plastic deformation in 6H-SiC is due to motion of the existing dislocations rather than the nucleation of new dislocations.

5.4   Discussion

In this study I find that in 6H-SiC strong covalent bonding controls the mechanical behavior giving rise to high strength yet no plastic deformation when loading direction is along $\langle 0001 \rangle$ suppressing the easy basal slip at room-temperature; Φ_0 pillars. Changing the loading direction to be at $45°$ with respect to $\langle 0001 \rangle$ (Φ_{45} pillars) leads to activation of basal slip. Using transmission electron microscope along with *ab initio* modeling, the glide of full dislocations on the shuffle set of the basal plane leads to the observed plastic deformation. Our experimental data suggests that the minimum compressive stress required for dislocation glide at room-temperature is 7.8 GPa in sub-micron-scale 6H-SiC crystals. Since defect size scales with the size of the SiC components; a smaller component is expected to encompass flaws with smaller size and thus the fracture stress approaches the ideal tensile stress. Hence, dislocation glide on the slip plane occurs before the fracture stress is reached, resulting in ductile deformation. No sign of pressure-induced phase transformation is observed in the tested Φ_{45} pillars.

CHAPTER 6

Shear Deformation in Single-Crystalline TaC

In this chapter results of uniaxial compression test on TaC(100) and TaC(011) sub-micron pillars, their deformation mechanisms and effects of size-scale and crystallographic orientation on yield strength and their room-temperature plasticity are being presented.

TaC behavior at room-temperature and T > 1800 °C show that the room-temperature deformation is dominated by the short-range movement of dislocations in multiple orientations, nanotwinning, grain rotation, crystallite misorientation with low-angle grain boundary formation, while at high temperature, a single slip system forming a parallel array of dislocations is dominant [126]. Due to the dominant metallic nature of bonding in TaC favorable slip planes can get activated to produce plastic deformation in a significant amount as compared to similar high-temperature ceramics, even at low temperatures [127]. At low temperatures {110} slip is characteristic of the group IV and substoichiometric group V transition metal carbides while stoichiometric group V carbides probably deform preferentially on {111} at all temperatures [128]. The ratio of carbon-to-metal plays an important role in the behavior of group IV and V transition-metal carbides. It is significant to note that TaC at high carbon-to-metal ratio exhibits more plastic flow than any other carbide having the rocksalt structure and it may be somewhat tougher than competitive monoceramics [42, 127].

In situ uniaxial compression tests carried out inside an electron microscope show that sub-micron-scale TaC(100) and TaC(011) crystals have shear deformation at room-temperature. I identify $\{1\bar{1}0\}\langle110\rangle$ and $\{1\bar{1}1\}\langle110\rangle$ as the active slip systems in TaC(100) and TaC(011), respectively. In contrast to the ZrC(100) *vs.* ZrC(111) results presented in Chapter 4, TaC crystals do not exhibit a strong size-dependence of yield strength. It is evident that for group IV or V TMCs such as TiC, ZrC, TaC, crystallographic orientation is a controlling factor

towards the strength and plasticity observed at the small-scale. While dislocation movement in ZrC(111) sub-micron pillars is observed, there is no clear sign of dislocation motion in TaC(100) or TaC(011) pillars, although both have B1 (rock salt) NaCl crystal structure. Stacking fault energy calculations via density functional theory (DFT) for various possible slip systems in TaC is also presented. However, the DFT work on TaC is still in progress and complete results will be presented later.

6.1   TaC(100) Strength and Plastic Deformation

Sub-micron pillars in the range of $100 - 500$ nm are subjected to uniaxial compression using PicoIndenter 95 holder inside the JEOL 3010 microscope. Regardless of the size, all of the pillars show shear deformation upon compression. Bright-field TEM images extracted from a video (see Movie "TaC(100)-S5") recorded during compression of ~ 0.45-μm-long TaC(100) pillar with diameter D $=$ 130 nm is presented in Figure 6.1 (A-G). Upon compression of the pillar, yielding occurs via shear. In this experiment, I observe localized deformation and the formation of shear bands near the top of the pillar that is in contact with the diamond punch. In this experiment the pillar is loaded to 100 nm. The first occurrence of shear, labeled 1 in Figure 6.1 (C), at 35 nm is followed by the formation of a surface and formation of a second shear plane, labeled 2 in Figure 6.1 (D) at ~ 50 nm. Figure 6.1 (E) shows the post-compression morphology of the pillar. Selected area electron diffraction (SAED) pattern (Figure 6.1 (F)) acquired from the compressed pillar indicates that the pillar retains its single-crystalline B1 (NaCl) structure, i.e. TaC pillars do not undergo phase transformation and/or twinning due to compression. Figure 6.1(G) is a representative plot of stress *vs.* displacement measured during *in situ* compression of the TaC(100) pillar. The points 1 and 2 in the plot (indicated by arrows), correspond to the times at which macroscopic shear events 1 and 2 occurred in the pillar (Figures 6.1 (C-D)). In this experiment, the deviation from linearity in the stress-displacement data occurred at an engineering stress of ~ 10 GPa. This value corresponding to the point of transition from elastic to plastic deformation is the yield strength, σ_y.
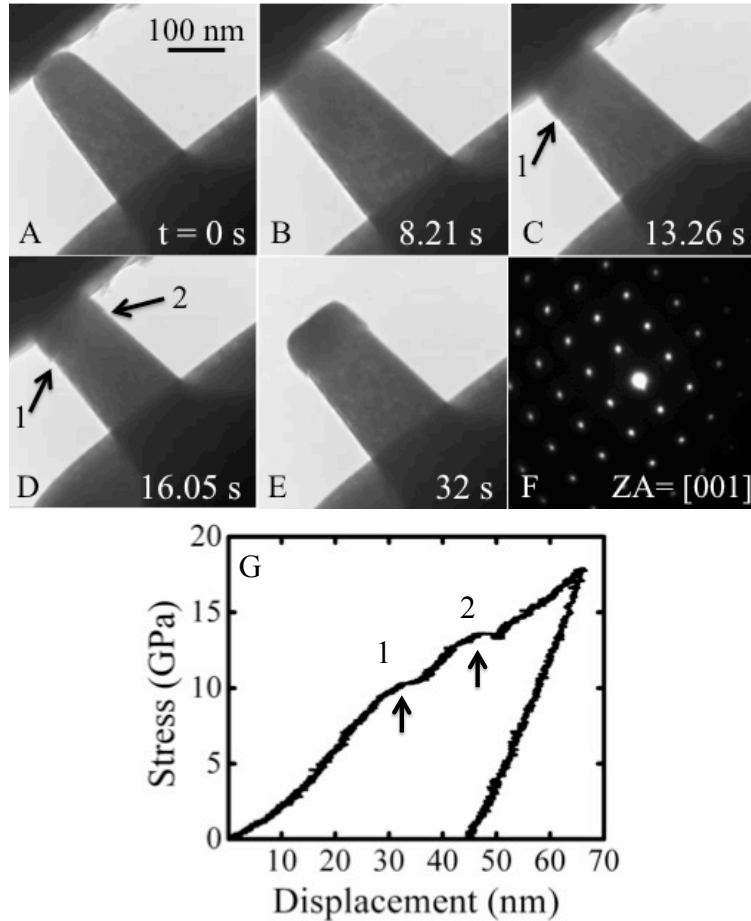
Figure 6.1: A-D) Bright-field TEM images acquired *in situ* during displacement-controlled uniaxial compression of a TaC(100) pillar with diameter D = 130 nm. E) Bright-field TEM image of the pillar after the compression test. F) Selected area electron diffraction (SAED) pattern acquired along [001] zone axis. G) Plot of engineering stress *vs.* displacement measured during compression of the pillar.

This behavior is typical of all the TaC(001) pillars that are tested. Slip system of TaC(100) is determined to be $\{1\bar{1}0\}\langle110\rangle$ following the analysis described in Chapter 4 Figure 4.2. It is likely that $\langle110\rangle$, the direction with the shortest repeat distance in NaCl lattice, is also the slip direction in these experiments. This is plausible since the resolved shear stress during compression along [100] is highest for the $\{110\}\langle1\bar{1}0\rangle$ slip systems and consistent with previous room-temperature microindentation tests conducted on bulk group

73

IV (100)- oriented transition-metal carbide single-crystals [41,112]. There is no clear sign of dislocations during post-compression analysis. It is believed that due to the confined volume of the pillars dislocations might have left the pillars upon slip. Slip traces are shown in Figure 6.2 (A-B) post-compression and after thinning a TaC(100) pillar.
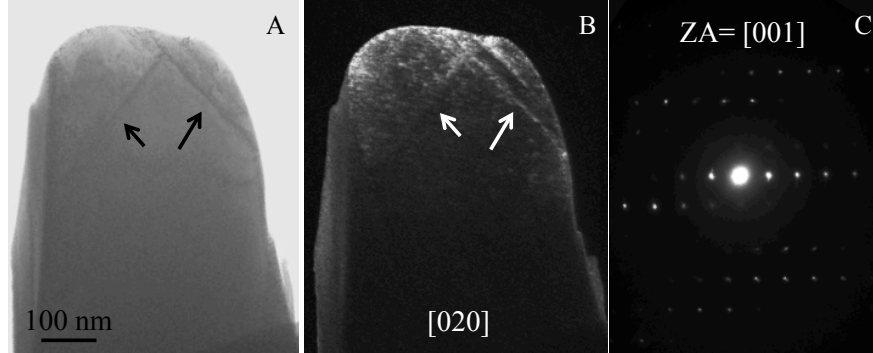
Figure 6.2: A) Bright- and B) dark-field TEM images obtained from a TaC(100) pillar with D = 380 nm after shear deformation. The dark-field image is obtained using [020] reflection. C) SAED pattern of the pillar along [001] zone axis, indicating that the pillar retains its single-crystalline structure post-compression. Slip traces (highlighted by the arrows) indicate that the slip plane orientation is {110}.

6.2   TaC(011) Strength and Plastic Deformation

Similar behavior is observed for TaC(011) sub-micron pillars. Pillars exhibit slip and deform via shear on {111} planes. Figure 6.3 (A-D) are representative bright-field TEM images extracted from a video (see Movie "TaC(011)- S6") recorded during the compression of $\sim$ 0.40-μm-long TaC(011) pillar with D = 115 nm. The major shear event, labeled 1 in Figure 6.3 (D), occurs at $\sim$ 35 nm followed by the formation of a surface step. Figure 6.3 (E) shows the post-compression morphology of the pillar. The SAED pattern in Figure 6.3 (F), acquired from the TaC(011) pillar after the test, indicates that both the crystal structure and the crystallinity of the pillar are unaffected by the compression. Figure 6.3 (G) is a plot of the stress *vs.* displacement data acquired during compression of the pillar. This behavior

is typical of all the TaC(011) pillars that tested in this study.

In both TaC(001) and TaC(011) the abrupt changes ("pop-ins") associated with slip is captured in the videos and observed in the mechanical response.
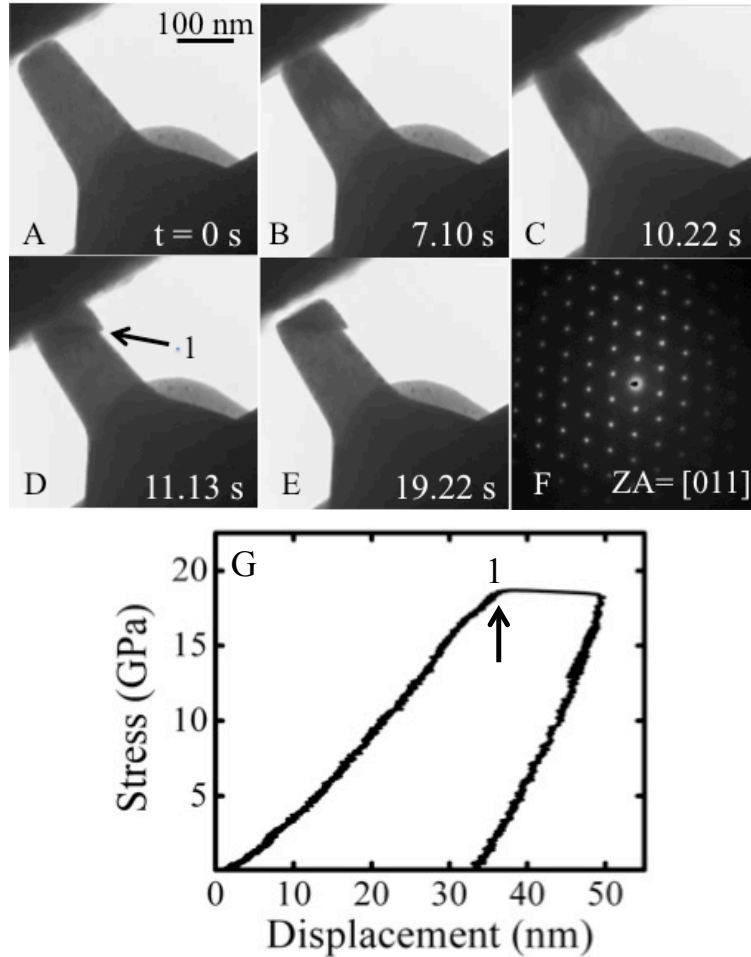
Figure 6.3: A-D) Bright-field TEM images extracted from a video recorded during uniaxial compression of a D = 115 nm TaC(011) pillar up to 100 nm. E) Bright-field TEM image of the pillar after the compression test. F) Selected area electron diffraction (SAED) pattern acquired along [011] zone axis. G) Plot of engineering stress *vs.* displacement measured during compression of the pillar.

To gain a better insight into plastic deformation mechanism and active slip system for TaC(011), post-compression analysis is conducted. The resolved shear stress on $\{1\bar{1}1\}\langle110\rangle$ slip systems is the highest followed by $\{001\}\langle110\rangle$ and $\{\bar{1}10\}\langle110\rangle$ during loading along [011]. Hence $\{1\bar{1}1\}\langle110\rangle$ is the dominant slip system. Similar analysis as Figure 4.2 in Chapter 4 is also applicable here to identify $\{1\bar{1}1\}$ as the slip plane orientation based on the diffraction pattern. Slip traces are shown in Figure 6.4 (A-B) post-compression and after thinning a TaC(011) pillar.
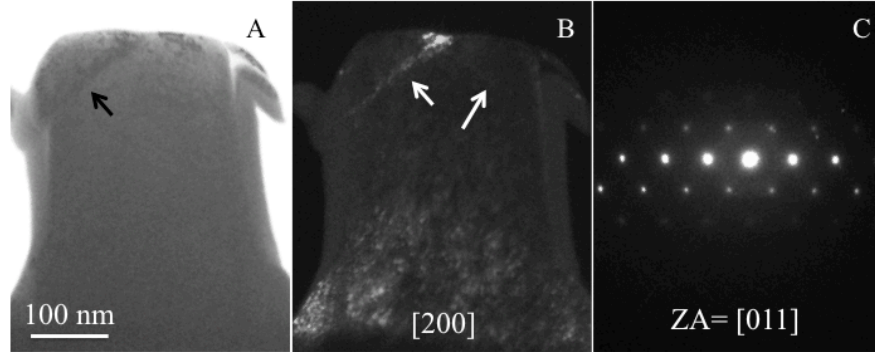
Figure 6.4: A) Bright- and B) dark-field TEM images of a TaC(011) pillar with D = 300 nm acquired post-compression test. The dark-field image is obtained using [200] reflection. C) SAED pattern of the pillar along [011] zone axis. Slip traces (highlighted by the arrows) indicate that the slip plane orientation is $\{111\}$.

6.3   Size-Dependence of Strength

To gain better insights into the plastic deformation behavior in TaC, uniaxial compression tests on 18 TaC pillars of each crystallographic orientation with D between 100 and 500 nm are carried out. The engineering stress *vs.* strain behavior of different size TaC pillars is illustrated in Figure 6.5. For a given crystallographic orientation, all the pillars exhibit similar deformation behavior. And, for both orientations, the maximum stresses withstood by the pillars before failure increase with decreasing D but the change is rather insignificant.
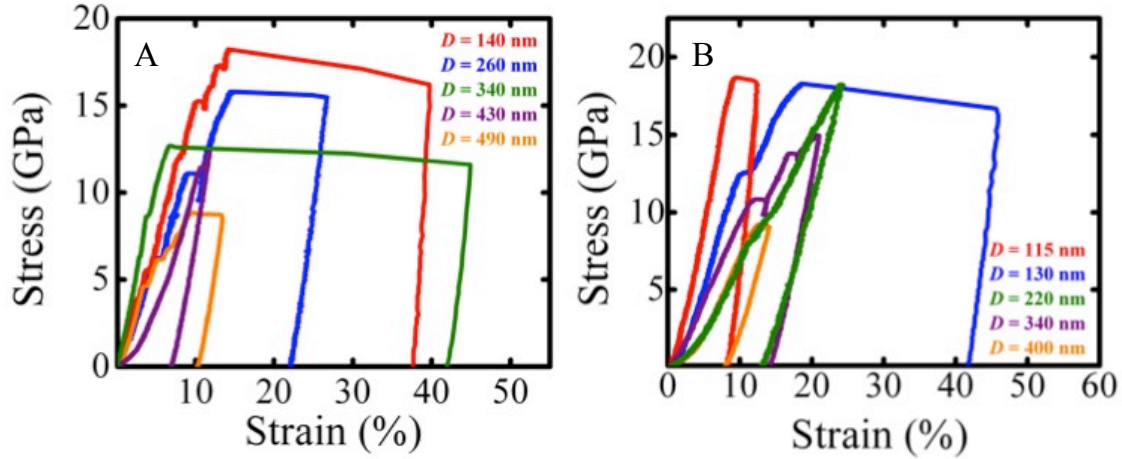
Figure 6.5: Plots of engineering stress *vs.* engineering strain for A) TaC(100) and B) TaC(011) pillars in the size range of D = 100 − 500 nm. Experiments are run in displacement-controlled mode and hence, the maximum strain does not correspond to fracture.

To determine the yield points and σ_y values, stress-displacement data of all the pillars are plotted in log-log scale. By using the least-squares fits to the data similar to what shown in Figure 4.8 in Chapter 4, the transition point from linearity defined as yield point and its value is extracted.

Upon obtaining the σ_y values for all the pillars (values between ∼ 5 and 18 GPa), log-log plot of σ_y *vs.* D for all the TaC pillars in both [100] and [011] orientations is illustrated in Figure 6.6. It is indicated that yield strengths of both TaC(100) and TaC(011) pillars slightly increase with decreasing D. The change is not significant and it can be concluded that for TaC crystals in this study there is no effect of size-scale on the yield strength (σ_y). This result is in contrary to what is observed for similar structured ZrC(100) and ZrC(111) crystals (this research, Chapter 4) and ionic crystal LiF[111] [88] where a strong size-effect has been reported. However it is aligned with what is previously reported for ionic LiF[111] [89], MgO [35] and silicon [129] where almost no size effect on the yield stress has been observed.

Here I find that σ_y for TaC(100) varies from 5 to 12 GPa and for TaC(011) varies from 7 to 18 GPa and although data is scattered but TaC(100) pillars are overall softer than
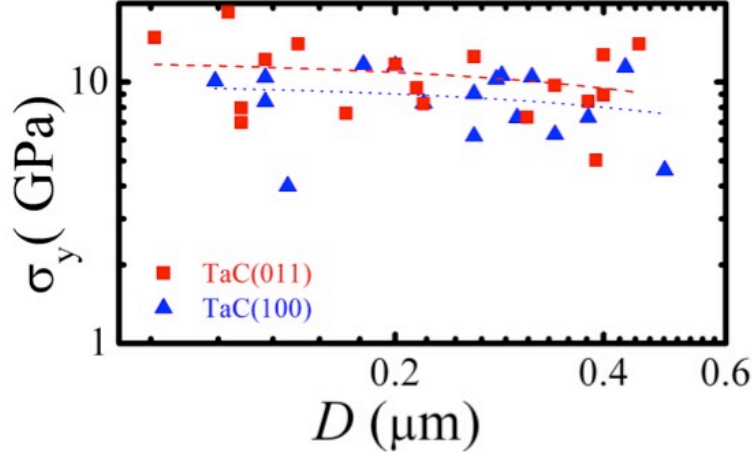
Figure 6.6: Log-log plot of yield strength *vs.* diameter for TaC(100) (□) and TaC(011) (▲) pillars. The dashed lines are linear least-squares fit to the data.

TaC(011) pillars.

Dr. Ratsch performed density-functional theory (DFT) calculations to measure uniaxial stresses required to deform stoichiometric TaC single-crystals and energy barriers associated with slip and shear along the primary slip systems to have a better understanding of the slip systems and deformation mechanism.

6.4 DFT Calculations

The DFT calculation for TaC is still a work in progress. Based on stacking fault energies for various possible slip systems in TaC, $\{1\bar{1}1\}\langle110\rangle$ and $\{110\}\langle110\rangle$ are identified as two active slip systems. However, ideal strengths of TaC during uniaxial compression as a function of crystallographic orientation and the plot of compressive stress *vs.* strain as shown for ZrC in Chapter 4 yet to be completed. Table 6.1 summarizes the results for stacking fault energies.

Table 6.1: Stacking fault energies for various slip systems in TaC

Slip system	Energy(eV/A^2)
$\{110\}\langle110\rangle$	0.103
$\{111\}\langle110\rangle$	0.035
$\{001\}\langle110\rangle$	0.139
$\{110\}\langle100\rangle$	0.309
$\{110\}\langle111\rangle$	0.336
$\{001\}\langle100\rangle$	0.168

6.5 Discussion

In this study, I show that sub-micron-scale TaC crystals undergo plastic deformation. In transition-metal carbides and nitrides, a mixture of metallic, ionic, and covalent bonds control their mechanical properties. In TaC the metallic bond is dominant and the behavior is similar to FCC metals. The primary mode of deformation in both TaC(100) and TaC(011) pillars is shear deformation. It is also observed that TaC crystals in this study do not show a strong size-scale dependence of yield strength. Using DFT calculations, we attribute the observed behavior to deformation along $\{110\}\langle110\rangle$ and $\{1\bar{1}1\}\langle110\rangle$ slip systems based on the stacking fault energy values. Results on TaC sub-micron pillars presented here indicate that multiple slip systems can be active at room-temperature and plasticity could be expected in hard, refractory transition-metal carbides.

CHAPTER 7

Conclusion and Future Work

In this study, nanomechanical properties of single-crystalline transition-metal carbides; ZrC and TaC and silicon-based ceramics; SiC are investigated. The effect of size and crystallographic orientation on plastic deformation and strength of ZrC and TaC with B1 (rock salt) NaCl crystal structure (cubic) and 6H-SiC with wurtzite (hexagonal) crystal structure are compared using *in situ* TEM uniaxial compression testing. Density function theory (DFT) calculations and molecular dynamics (MD) simulations as part of a collaboration work in this research are conducted to better understand the underlying deformation mechanism and the most favorable slip systems in these inherently brittle compounds exhibiting plasticity at small size-scale at room-temperature.

7.1   ZrC and TaC Crystals

In this study I show that crystallographic orientation has a major role in the behavior of the B1(rocksalt) NaCl structure crystals. Both ZrC - a group IV- and TaC - a group V- transition-metal carbides have a combination of ionic-covalent-metallic bonding that controls their mechanical properties. For ZrC(100) *vs.* ZrC(111) pillars with D = 100 – 500 nm subjected to *in situ* TEM uniaxial compression test a very distinct behavior is observed. While ZrC(100) pillars have shear deformation along the {110} planes, ZrC(111) pillars deform via dislocation tangling and movement on {100} planes. For both crystals, yield strength varies with D with more change observed for ZrC(111) from 0.5 to 9 GPa. TaC on the other hand does not follow the same trend. For TaC(100) *vs.* TaC(011) pillars with D = 100 – 500 nm subjected to *in situ* TEM uniaxial compression test a similar deformation

mechanism is observed. Both crystals deform via shear on planes with highest Schmidt factor; {110} for TaC(100) and {111} for TaC(011) pillars. The size-scale effect on the yield stress is insignificant. These findings emphasize the importance of the role of crystallographic orientation: [100], [011], [111] in case of B1(rock salt) NaCl crystal structure on the strength and plasticity at room-temperature.

Using DFT calculations, and calculating the stacking fault energies we attribute the observed plasticity to relatively easy deformation along $\{001\}\langle110\rangle$ rather than along the commonly expected $\{1\bar{1}0\}\langle110\rangle$ slip systems in ZrC crystals. DFT calculations suggest the active slip systems to be $\{1\bar{1}0\}\langle110\rangle$ and $\{1\bar{1}1\}\langle110\rangle$ for TaC pillars loaded along [100] and [011] directions, respectively consistent with experimental results.

7.2 6H-SiC Crystals

This significance of the crystallographic orientation effect is also observed for 6H-SiC crystals with hexagonal crystal structures at room-temperature. While loading along basal direction $\langle0001\rangle$ (Φ_0 pillars) suppresses the plastic deformation and leads to brittle fracture, loading at 45° with respect to (Φ_{45} pillars) results in plastic deformation via basal slip. *In situ* TEM uniaxial compression test along with *ab intio* modeling point towards dislocation glide on basal planes as the controlling mechanism for enhanced plasticity in 6H-SiC (Φ_{45}) pillars. Although similar behavior is seen for all the tested pillars in the size range of 170 – 280 nm, but the effect of size-scale is not significant. Pillars are extremely sensitive to misalignment and aspect ratio. Considering the high ideal shear stress of 33 GPa required for surface dislocation nucleation in SiC based on the simulation outcomes, it is believed that the sustained plastic flow is not governed by surface dislocation nucleation, but by dislocation glide in the material.

Results on ZrC, TaC and 6H-SiC sub-micron pillars presented here indicate that multiple slip systems can be active at room-temperature and plasticity could be expected in hard, refractory transition-metal carbides and ceramics. This will open up new opportunities to consider materials traditionally believed to be brittle for "hard-yet-tough" applications. How-

ever, more in-depth understanding of dislocation dynamics are required to fully understand the origin of plastic deformation which is outside the scope of this research.

7.3   Future Work

Based on my *in situ* TEM compression study on ceramics, it should be mentioned that this combination of nanoscale *in situ* mechanical testing combined with TEM imaging and analysis of nanoscale materials (pillars, nanowires, etc.) is an important field where new instrumentation and techniques can make a large impact. Since most research in the field is on metallic samples, non-metallic materials that are believed to be brittle at room-temperature are less studied. However, as shown in this research, reducing the size to sub-micron range leads to enhanced plasticity in this group of materials. The work presented here is perhaps one of the few works on small-scale testing of ceramics and have a lot of opportunities to expand. Here are some suggestions based on the current research that is worth exploring and will provide valuable information about the intrinsic behavior of ceramics: 1) Most of the previous studies are done at high temperature in bulk looking at thermomechanical properties. However, a quantitative holder that is capable of measuring mechanical response at small size-scale at temperatures ≥ 1000 °C is not commercially available at this point. As the technology progresses having such a holder will allow room-temperature and high temperature comparison of deformation mechanisms and activate slip systems in ceramics at the nanoscale. 2) This study focuses on single-crystalline samples to set a foundation for knowing the behavior of individual crystals at small size-scale. However, in real applications poly-crystalline or composite of such materials (e.x. SiC/ZrB_2 or ZrC/SiC, etc.) are widely used. Having the information on single-crystalline samples, the next step would be looking into poly-crystalline samples or composite of such materials to understand the effect of grain boundaries, dislocation/grain boundary interactions, role of particles *vs.* fibers as reinforcement, etc. on the deformation mechanism and yield strength at the nanoscale. 3) Considering other *in situ* testing methods such as tension or bending. As an example for 6H-SiC, I conducted an *in situ* TEM tensile experiment on a 200 nm-thick foil to evaluate

the behavior of this material under tension (see Figure 7.1. and movie "6H-SiC- tensile-S7"). The tensile sample is prepared in FIB and moved (standard lift-out procedure) to the PTP device inside the FIB/SEM dual beam system as described in Chapter 3 Section 3.4.
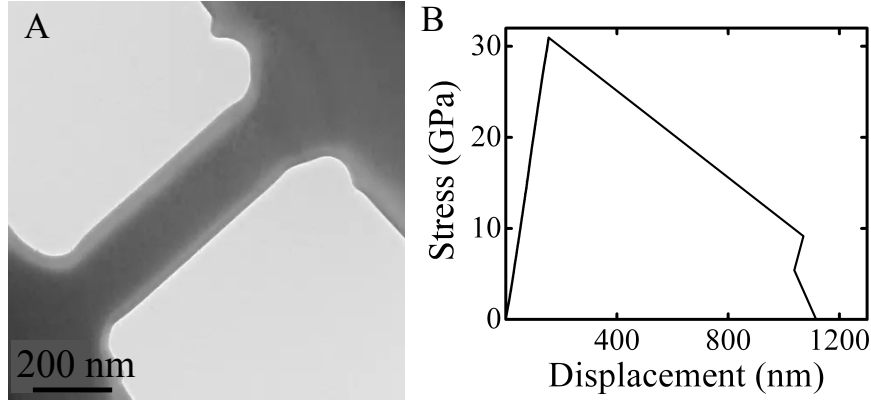
Figure 7.1: A) Bright-field image of the 200 nm-thick tensile bar subjected to *in situ* uni-axial tensile testing with loading rate of 4 nm/s. B) corresponding stress-displacement plot showing an abrupt brittle fracture at 30 GPa.

As it is seen throughout this research both size and crystallographic orientation have strong effect on the material's behavior at the nanoscale. In this study, I show that although there is no sign of plasticity, but a high $\sim$ 30 GPa tensile strength is achieved before the failure. Crystallographic orientation is not clear for this sample due to the location where the FIB lift-out is done. However, a more systematic study with orientation mapping will provide a complete study of the tensile behavior of the SiC samples in the sub-micron size regime as a function of crystallographic orientation.

References

[1] W. Gerberich, J. Michler, W. M. Mook, R. Ghisleni, F. Ostlund, D. D. Stauffer, and R. Ballarini, "Scale effects for strength, ductility, and toughness in 'brittle' materials," *J. Mater. Res*, vol. 24, pp. 898 - 906, 2009.

[2] R. Raj, "Fundamental research in structural ceramics for service near 2000°C," *J. Am. Ceram. Soc.*, vol.76, pp. 2147-2174, 1993.

[3] E. L. Corral and R. E. Loehman, "Ultra-high temperature ceramic coatings for oxidation protection of carbon - carbon composites," *J. Am. Ceram. Soc.*, vol. 91, no. 5, pp. 1495 - 1502, 2008.

[4] Sh. Somya, *Handbook of advanced ceramics: materials, applications, processing, and properties.* Academic Press, 2013, p. 1258.

[5] E. Wuchina, E. Opila, M. Opeka, W. Fahrenholtz, and I. Talmy, "UHTCs: Ultra-high temperature ceramic materials for extreme environment applications," *Elctrochem. soc. Interface*, pp.30 - 36, 2007.

[6] R. Savino, M. D. S. Fumo, L. Silvestroni, and D. Sciti, "Arc-jet testing on HfB_2 and HfC-based ultra-high temperature ceramic materials," *J. Eur. Ceram. Soc.*, vol. 28, no. 9, pp. 1899 - 1907, 2008.

[7] W. G. Fahrenholtz, G. E. Hilmas, I. G. Talmy, and J. A. Zaykoski, "Refractory diborides of zirconium and hafnium," *J. Am. Ceram. Soc.*, vol. 90, no. 5, pp. 1347 - 1364, 2007.

[8] H. A. Bale, A. Haboub, A. A. MacDowell, J. R. Nasiatka, D. Y. Parkinson, B. N. Cox, D. B. Marshall, and R. O. Ritchie, "Real-time quantitative imaging of failure events in materials under load at temperatures above 1600° C"*Nat. Mater.*, vol. 12, no. 1, pp. 40 - 46, 2013.

[9] M. Behaviour and P. F. Becher, "Mechanical behaviour of polycrystalline TaC," *J. Mater. Sci.*, vol. 6, no. 1, pp. 79 - 80, 1971.

[10] F. Monteverde, "Beneficial effects of an ultra-fine α-SiC incorporation on the sinterability and mechanical properties of ZrB_2," *Appl. Phys. A*, vol. 82, no. 2, pp. 329 - 337, 2005.

[11] I. Akin, M. Hotta, F. C. Sahin, O. Yucel, G. Goller, and T. Goto, "Microstructure and densification of ZrB_2-SiC composites prepared by spark plasma sintering," *J. Eur. Ceram. Soc.*, vol. 29, no. 11, pp. 2379 - 2385, 2009.

[12] B. M. Moshtaghioun, A. L. Ortiz, D. Gómez-García, and A. Domínguez-Rodríguez, "Toughening of super-hard ultra-fine grained B_4C densified by spark-plasma sintering via SiC addition," *J. Eur. Ceram. Soc.*, vol. 33, no. 8, pp. 1395 - 1401, 2013.

[13] G. B. Yadhukulakrishnan, A. Rahman, S. Karumuri, M. M. Stackpoole, A. K. Kalkan, R. P. Singh, and S. P. Harimkar, "Spark plasma sintering of silicon carbide and multi-walled carbon nanotube reinforced zirconium diboride ceramic composite," *Mater. Sci. Eng. A*, vol. 552, pp. 125 - 133, 2012.

[14] G. B. Yadhukulakrishnan, S. Karumuri, A. Rahman, R. P. Singh, A. Kaan Kalkan, and S. P. Harimkar, "Spark plasma sintering of graphene reinforced zirconium diboride ultra-high temperature ceramic composites," *Ceram. Int.*, vol. 39, no. 6, pp. 6637 - 6646, 2013.

[15] W.-B. Tian, Y.-M. Kan, G.-J. Zhang, and P.-L. Wang, "Effect of carbon nanotubes on the properties of ZrB_2-SiC ceramics," *Mater. Sci. Eng. A*, vol. 487, pp. 568 - 573, 2008.

[16] W. Li, Y. Zhang, X. Zhang, C. Hong, and W. Han, "Thermal shock behavior of ZrB_2-SiC ultra-high temperature ceramics with addition of zirconia," *J. Alloys Compd.*, vol. 478, pp. 386 - 391, 2009.

[17] J. Marschall, D. A. Pejakovic, W. G. Fahrenholtz, G. E. Hilmas, S. Zhu, J. Ridge, D. G. Fletcher, C. O. Asma, and J. Thoemel, "Oxidation of ZrB_2-SiC ultrahigh-temperature ceramic composites in dissociated air," *J. Thermophys. Heat Transf.*, vol. 23, no. 2, pp. 267 - 278, 2009.

[18] M. Gasch, D. Ellerby, E. Irby, S. Beckman, M. Gusman, and S. Johnson, "Processing, properties and arc jet oxidation of hafnium diboride/silicon carbide ultra high temperature ceramics," *J. Mater. Sci.*, vol. 39, no. 19, pp. 5925 - 5937, 2004.

[19] H. O. Pierson, *Handbook of refractory carbides & nitrides: properties, characteristics, processing and apps.* Noyes Publications, 1996, p. 362.

[20] M. Iwami, "Silicon carbide: fundamentals," *Nucl. Instruments Methods Phys. Res. Sect. A Accel. Spectrometers, Detect. Assoc. Equip.*, vol. 466, no. 2, pp. 406 - 411, 2001.

[21] L. Yin, E. Y. J. Vancoille, K. Ramesh, and H. Huang, "Surface characterization of 6H-SiC (0001) substrates in indentation and abrasive machining," *Int. J. Mach. Tools Manuf.*, vol. 44, no. 6, pp. 607 - 615, 2004.

[22] A. Sayir and F. S. Lowery, "Combustion-resistance of silicon-based ceramics and composites at very high oxygen pressures," *J. Mater. Sci.*, vol. 39, no. 19, pp. 5979 - 5985, 2004.

[23] F. Monteverde, A. Bellosi, and L. Scatteia, "Processing and properties of ultra-high temperature ceramics for space applications," *Mater. Sci. Eng. A*, vol. 485, no. 1-2, pp. 415 - 421, 2008.

[24] W. G. Fahrenholtz, "Thermodynamic analysis of ZrB_2-SiC oxidation: formation of a SiC-depleted region," *J. Am. Ceram. Soc.*, vol. 90, no. 1, pp. 143 - 148, 2007.

[25] B.-R. Kim, K.-D. Woo, J.-M. Doh, J.-K. Yoon, and I.-J. Shon, "Mechanical properties and rapid consolidation of binderless nanostructured tantalum carbide," *Ceram. Int.*, vol. 35, no. 8, pp. 3395 - 3400, 2009.

[26] M. Ma, W. Shen, P. Zhang, J. Zhang, Q. Wang, and C. Ge, "Synthesis of TaC nanopowders by liquid precursor route," *Mater. Lett.*, vol. 65, no. 1, pp. 96 - 99, 2011.

[27] X. Zhang, G. E. Hilmas, W. G. Fahrenholtz, and D. M. Deason, "Hot pressing of tantalum carbide with and without sintering additives," *J. Am. Ceram. Soc.*, vol. 90, no. 2, pp. 393 - 401, 2007.

[28] C. L. Yeh and E. W. Liu, "Combustion synthesis of tantalum carbides TaC and Ta_2C," *J. Alloys Compd.*, vol. 415, no. 1-2, pp. 66 - 72, 2006.

[29] "Wurtzite crystal structure - Wikipedia, the free encyclopedia." [online]. Available: http://en.wikipedia.org/wiki/Wurtzite_crystal_structure.

[30] A. A. Kelly and K. M. Knowles, *Crystallography and crystal defects.* John Wiley & Sons, 2012, p. 521.

[31] D. W. Lee and J. S. Haggerty, "Plasticity and creep in single crystals of zirconium carbide," *J. Am. Ceram. Soc.*, vol. 52, no. 12, pp. 641 - 647, 1969.

[32] L. E. Toth, *Transition metal carbides and nitrides.* Academic Press, 1971, p. 279.

[33] M. N. Shetty, *Dislocations and mechanical behaviour of materials.* PHI Learning Pvt. Ltd., 2013, p. 1000.

[34] T. Mayama, K. Aizawa, Y. Tadano, and M. Kuroda, "Influence of twinning deformation and lattice rotation on strength differential effect in polycrystalline pure magnesium with rolling texture," *Comput. Mater. Sci.*, vol. 47, no. 2, pp. 448 - 455, 2009.

[35] S. Korte and W. J. Clegg, "Discussion of the dependence of the effect of size on the yield stress in hard materials studied by microcompression of MgO," *Philos. Mag.*, vol. 91, no. 7 - 9, pp. 1150 - 1162, 2011.

[36] A. E. Gorum, E. R. Parker, and J. A. Pask, "Effect of surface conditions on room-temperature ductility of ionic crystals," *J. Am. Ceram. Soc.*, vol. 41, no. 5, pp. 161 - 164, 1958.

[37] J. Deneen, W. M. Mook, A. Minor, W. W. Gerberich, and C. Barry Carter, "In situ deformation of silicon nanospheres," *J. Mater. Sci.*, vol. 41, no. 14, pp. 4477 - 4483, 2006.

[38] F. Östlund, P. R. Howie, R. Ghisleni, S. Korte, K. Leifer, W. J. Clegg, and J. Michler, "Ductile - brittle transition in micropillar compression of GaAs at room temperature," *Philos. Mag.*, vol. 91, no. 7 - 9, pp. 1190 - 1199, 2011.

[39] W. J. Clegg, K. Kendall, N. M. Alford, T. W. Button, and J. D. Birchall, "A simple way to make tough ceramics," *Nature*, vol. 347, no. 6292, pp. 455 - 457, 1990.

[40] J. Karch, R. Birringer, and H. Gleiter, "Ceramics ductile at low temperature," *Nature*, vol. 330, no. 6148, pp. 556 - 558, 1987.

[41] K. Kendall, "The impossibility of comminuting small particles by compression," *Nature*, vol. 272, no. 5655, pp. 710 - 711, 1978.

[42] D. J. Rowcliffe and G. E. Hollox, "Plastic flow and fracture of tantalum carbide and hafnium carbide at low temperatures," *J. Mater. Sci.*, vol. 6, no. 10, pp. 1261 - 1269, 1971.

[43] A. Kelly and D. J. Rowcliffe, "Deformation of poly crystalline transition metal carbides," *J. Am. Ceram. Soc.*, vol. 50, no. 5, pp. 253 - 256, 1967.

[44] R. A. Andrievskii, G. A. Rymashevskii, and V. S. Sinel'nikova, "Single crystals of refractory compounds: A review," *Sov. Powder Metall. Met. Ceram.*, vol. 11, no. 10, pp. 796 - 809, 1972.

[45] G. Morgan and M. H. Lewis, "Hardness anisotropy in niobium carbide," *J. Mater. Sci.*, vol. 9, no. 3, pp. 349 - 358, 1974.

[46] R. Stevens, "Dislocation movement and slip systems in β-SiC," *J. Mater. Sci.*, vol. 5, no. 6, pp. 474 - 477, 1970.

[47] P. Taylor, S. Fujita, K. Maeda, and S. Hyodo, "Dislocation glide motion in 6H-SiC single crystals subjected to high-temperature deformation," *Philos. Mag. A*, vol. 55, no. 2, pp. 203 - 215, 1987.

[48] P. Taylor, K. Maeda, K. Suzuki, S. Fujita, M. Ichihara, and S. Hyodo, "Defects in plastically deformed 6H-SiC single crystals studied by transmission electron microscopy," *Philos. Mag. A*, vol. 57, no. 4, pp. 573 - 592, 1988.

[49] A. V. Samant and P. Pirouz, "Activation parameters for dislocation glide in α-SiC," *Int. J. Refract. Met. Hard Mater.*, vol. 16, no. 4 - 6, pp. 277 - 289, 1998.

[50] J. Bill, F. Wakai, and F. Aldinger, *Precursor-derived ceramics: synthesis, structures and high temperature mechanical properties*, Wiley-VCH, 2008, p. 264.

[51] G. S. Corman, "Creep of 6H alpha-Silicon Carbide Single Crystals," *J. Am. Ceram. Soc.*, vol. 75, no. 12, pp. 3421 - 3424, 1992.

[52] M. Science, P. Street, C. Uk, G. R. Sawyer, P. M. Sargent, and T. F. Page, "Microhardness anisotropy of silicon carbide," *J. Mater. Sci.*, vol. 15, no. 4, pp. 1001 - 1013, 1980.

[53] C. R. Eddy, P. Wu, I. Zwieback, B. L. VanMil, R. L. Myers-Ward, J. L. Tedesco, A. E. Souzis, and D. K. Gaskill, "Microhardness of 6H- and 4H-SiC Substrates," *Mater. Sci. Forum*, vol. 615 - 617, pp. 323 - 326, 2009.

[54] T. F. Page, L. Riester, and S. V Hainswortht, "The plasticity response of 6H-SiC and related isostructural materials to nanoindentation: slip *vs.* densification," *Mat. Res. Soc. Proc.*, vol. 522, pp. 113 - 118, 1998.

[55] S. Shim, J. Jang, and G. M. Pharr, "Extraction of flow properties of single-crystal silicon carbide by nanoindentation and finite-element simulation," *Acta Mater.*, vol. 56, no. 15, pp. 3824 - 3832, 2008.

[56] A. J. G. Op Het Veld and J. D. 7B. Veldkamp, "Mechanical and microscopical investigation of SiC whiskers," *Fibre Sci. Technol.*, vol. 2, no. 4, pp. 269 - 281, 1970.

[57] E. W. Wong, P. E. Sheehan, and C. M. Lieber, "Nanobeam mechanics: elasticity, strength, and toughness of nanorods and nanotubes," *Science*, vol. 277, no. 5334, pp. 1971 - 1975, 1997.

[58] X. D. Han, Y. F. Zhang, K. Zheng, X. N. Zhang, Z. Zhang, Y. J. Hao, X. Y. Guo, J. Yuan, and Z. L. Wang, "Low-temperature in situ large strain plasticity of ceramic SiC nanowires and its atomic-scale mechanism.," *Nano Lett.*, vol. 7, no. 2, pp. 452 - 7, 2007.

[59] Y. Zhang, X. Han, K. Zheng, Z. Zhang, X. Zhang, J. Fu, Y. Ji, Y. Hao, X. Guo, and Z. L. Wang, "Direct observation of super-plasticity of beta-SiC nanowires at low temperature," Adv. Funct. Mater., vol. 17, no. 17, pp. 3435 - 3440, 2007.

[60] "PI Series PicoIndenters | In-Situ Nanomechanics in the TEM or SEM | Hysitron." [Online]. Available: http://www.hysitron.com/products/pi-series.

[61] M. D. Uchic, D. M. Dimiduk, J. N. Florando, and W. D. Nix, "Sample dimensions influence strength and crystal plasticity.," *Science*, vol. 305, no. 5686, pp. 986 - 9, 2004.

[62] J. R. Greer, W. C. Oliver, and W. D. Nix, "Size dependence of mechanical properties of gold at the micron scale in the absence of strain gradients," *Acta Mater.*, vol. 53, no. 6, pp. 1821 - 1830, 2005.

[63] J. Greer and W. Nix, "Nanoscale gold pillars strengthened through dislocation starvation," *Phys. Rev. B*, vol. 73, no. 24, pp. 1 - 6, 2006.

[64] J. R. Greer and W. D. Nix, "Size dependence of mechanical properties of gold at the sub-micron scale," *Appl. Phys. A*, vol. 80, no. 8, pp. 1625 - 1629, 2005.

[65] V. Sriram, J.-M. Yang, J. Ye, and A. M. Minor, "In-situ metrology and testing of nanotwinned copper pillars for potential air gap applications," *Microelectron. Eng.*, vol. 87, no. 11, pp. 2046 - 2049, 2010.

[66] A. T. Jennings, M. J. Burek, and J. R. Greer, "Microstructure versus size: mechanical properties of electroplated single crystalline Cu nanopillars," *Phys. Rev. Lett.*, vol. 104, no. 13, pp. 1 - 4, 2010.

[67] A. Kunz, S. Pathak, and J. R. Greer, "Size effects in Al nanopillars: Single crystalline vs. bicrystalline," *Acta Mater.*, vol. 59, no. 11, pp. 4416 - 4424, 2011.

[68] K. S. Ng and A. H. W. Ngan, "Stochastic nature of plasticity of aluminum micro-pillars," *Acta Mater.*, vol. 56, no. 8, pp. 1712 - 1720, 2008.

[69] K. E. Prasad, K. Rajesh, and U. Ramamurty, "Micropillar and macropillar compression responses of magnesium single crystals oriented for single slip or extension twinning," *Acta Mater.*, vol. 65, pp. 316 - 325, 2014.

[70] J. Ye, R. K. Mishra, A. K. Sachdev, and A. M. Minor, "In situ TEM compression testing of Mg and Mg - 0.2wt.% Ce single crystals," *Scr. Mater.*, vol. 64, no. 3, pp. 292 - 295, 2011.

[71] J.-Y. Kim, D. Jang, and J. R. Greer, "Insight into the deformation behavior of niobium single crystals under uniaxial compression and tension at the nanoscale," *Scr. Mater.*, vol. 61, no. 3, pp. 300 - 303, 2009.

[72] J.-Y. Kim, D. Jang, and J. R. Greer, "Tensile and compressive behavior of tungsten, molybdenum, tantalum and niobium at the nanoscale," *Acta Mater.*, vol. 58, no. 7, pp. 2355 - 2363, 2010.

[73] H. Bei, S. Shim, E. P. George, M. K. Miller, E. G. Herbert, and G. M. Pharr, "Compressive strengths of molybdenum alloy micro-pillars prepared using a new technique," *Scr. Mater.*, vol. 57, no. 5, pp. 397 - 400, 2007.

[74] J.-Y. Kim and J. R. Greer, "Size-dependent mechanical properties of molybdenum nanopillars," *Appl. Phys. Lett.*, vol. 93, no. 10, p. 101916, 2008.

[75] A. Schneider, D. Kaufmann, B. Clark, C. Frick, P. Gruber, R. Mönig, O. Kraft, and E. Arzt, "Correlation between critical temperature and strength of small-scale bcc pillars," *Phys. Rev. Lett.*, vol. 103, no. 10, pp. 1 - 4, 2009.

[76] J.-Y. Kim, J. R. Greer, C. R. Weinberger, and W. Cai, "Surface-controlled dislocation multiplication in metal micropillars.," *Proc. Natl. Acad. Sci. U. S. A.*, vol. 105, no. 38, pp. 14304 - 14307, 2008.

[77] A. M. Minor, S. A. S. Asif, Z. Shan, E. A. Stach, E. Cyrankowski, T. J. Wyrobek, and O. L. Warren, "A new view of the onset of plasticity during the nanoindentation of aluminium.," *Nat. Mater.*, vol. 5, no. 9, pp. 697 - 702, 2006.

[78] Z. W. Shan, R. K. Mishra, S. A. Syed Asif, O. L. Warren, and A. M. Minor, "Mechanical annealing and source-limited deformation in submicrometre-diameter Ni crystals.," *Nat. Mater.*, vol. 7, no. 2, pp. 115 - 119, 2008.

[79] K. Wasmer, T. Wermelinger, a. Bidiville, R. Spolenak, and J. Michler, "In situ compression tests on micron-sized silicon pillars by Raman microscopy – Stress measurements and deformation analysis," *J. Mater. Res.*, vol. 23, no. 11, pp. 3040 - 3047, 2011.

[80] F. Östlund, K. Rzepiejewska-Malyska, K. Leifer, L. M. Hale, Y. Tang, R. Ballarini, W. W. Gerberich, and J. Michler, "Brittle-to-ductile transition in uniaxial compression of silicon pillars at room temperature," *Adv. Funct. Mater.*, vol. 19, no. 15, pp. 2439 - 2444, 2009.

[81] S. Korte, J. S. Barnard, R. J. Stearn, and W. J. Clegg, "Deformation of silicon – insights from microcompression testing at 25 - 500°C," *Int. J. Plast.*, vol. 27, no. 11, pp. 1853 - 1866, 2011.

[82] A. Dubach, R. Raghavan, J. F. Löffler, J. Michler, and U. Ramamurty, "Micropillar compression studies on a bulk metallic glass in different structural states," *Scr. Mater.*, vol. 60, no. 7, pp. 567 - 570, 2009.

[83] Y. H. Lai, C. J. Lee, Y. T. Cheng, H. S. Chou, H. M. Chen, X. H. Du, C. I. Chang, J. C. Huang, S. R. Jian, J. S. C. Jang, and T. G. Nieh, "Bulk and microscale compressive behavior of a Zr-based metallic glass," *Scr. Mater.*, vol. 58, no. 10, pp. 890 - 893, 2008.

[84] C. Q. Chen, Y. T. Pei, and J. T. M. De Hosson, "Effects of size on the mechanical response of metallic glasses investigated through in situ TEM bending and compression experiments," *Acta Mater.*, vol. 58, no. 1, pp. 189 - 200, 2010.

[85] D. Jang and J. R. Greer, "Transition from a strong-yet-brittle to a stronger-and-ductile state by size reduction of metallic glasses.," *Nat. Mater.*, vol. 9, no. 3, pp. 215 - 9, 2010.

[86] L. Jiang and N. Chawla, "Mechanical properties of Cu_6Sn_5 intermetallic by micropillar compression testing," *Scr. Mater.*, vol. 63, no. 5, pp. 480 - 483, 2010.

[87] P. R. Howie, S. Korte, and W. J. Clegg, "Fracture modes in micropillar compression of brittle crystals," *J. Mater. Res.*, vol. 27, no. 01, pp. 141 - 151, 2011.

[88] E. M. Nadgorny, D. M. Dimiduk, and M. D. Uchic, "Size effects in LiF micron-scale single crystals of low dislocation density," *J. Mat. Res.*, vol. 23, pp. 2829 - 2835, 2008.

[89] R. Soler, J. M. Molina-Aldareguia, J. Segurado, J. Llorca, R. I. Merino, and V. M. Orera, "Micropillar compression of LiF[111] single crystals: effect of size, ion irradiation and misorientation," *Int. J. Plast.*, vol. 36, pp. 50 - 63, 2012.

[90] W. W. Gerberich, W. M. Mook, C. R. Perrey, C. B. Carter, M. I. Baskes, R. Mukherjee, A. Gidwani, J. Heberlein, P. H. McMurry, and S. L. Girshick, "Superhard silicon nanospheres," *J. Mech. Phys. Solids*, vol. 51, no. 6, pp. 979 - 992, 2003.

[91] J. D. Nowak, A. R. Beaber, O. Ugurlu, S. L. Girshick, and W. W. Gerberich, "Small size strength dependence on dislocation nucleation," *Scr. Mater.*, vol. 62, no. 11, pp. 819 - 822, 2010.

[92] J.-Y. Kim and J. R. Greer, "Tensile and compressive behavior of gold and molybdenum single crystals at the nano-scale," *Acta Mater.*, vol. 57, no. 17, pp. 5245 - 5253, 2009.

[93] J.-Y. Kim, D. Jang, and J. R. Greer, "Crystallographic orientation and size dependence of tension-compression asymmetry in molybdenum nano-pillars," *Int. J. Plast.*, vol. 28, no. 1, pp. 46 - 52, 2012.

[94] D. Kiener, W. Grosinger, G. Dehm, and R. Pippan, "A further step towards an understanding of size-dependent crystal plasticity: In situ tension experiments of miniaturized single-crystal copper samples," *Acta Mater.*, vol. 56, no. 3, pp. 580 - 592, 2008.

[95] D. Kiener and A. M. Minor, "Source truncation and exhaustion: insights from quantitative in situ TEM tensile testing.," *Nano Lett.*, vol. 11, no. 9, pp. 3816 - 20, 2011.

[96] S. H. Oh, M. Legros, D. Kiener, and G. Dehm, "In situ observation of dislocation nucleation and escape in a submicrometre aluminium single crystal.," *Nat. Mater.*, vol. 8, no. 2, pp. 95 - 100, 2009.

[97] T. T. Zhu, A. J. Bushby, and D. J. Dunstan, "Size effect in the initiation of plasticity for ceramics in nanoindentation," *J. Mech. Phys. Solids*, vol. 56, no. 4, pp. 1170 - 1185, 2008.

[98] C. A. Volkert and E. T. Lilleodden, "Size effects in the deformation of sub-micron Au columns," *Philos. Mag.*, vol. 86, no. 33 - 35, pp. 5567 - 5579, 2006.

[99] J. R. Greer and J. T. M. De Hosson, "Plasticity in small-sized metallic systems: intrinsic versus extrinsic size effect," *Prog. Mater. Sci.*, vol. 56, no. 6, pp. 654 - 724, 2011.

[100] D. B. Williams and C. B. Carter, *Transmission Electron Microscopy: a textbook for materials science, Volume 3.* Springer, 2009, p. 760.

[101] G. Kresse and J. Furthmüller, "Efficiency of ab-initio total energy calculations for metals and semiconductors using a plane-wave basis set," *Comput. Mater. Sci.*, vol. 6, no. 1, pp. 15 - 50, 1996.

[102] S. Plimpton, "Fast parallel algorithms for short-range molecular dynamics," *J. Comput. Phys.*, vol. 117, no. 1, pp. 1 - 19, 1995.

[103] R. Devanathan, T. Diaz de la Rubia, and W. J. Weber, "Displacement threshold energies in β-SiC," *J. Nucl. Mater.*, vol. 253, no. 1 - 3, pp. 47 - 52, 1998.

[104] L. Verlet, "Computer 'experiments' on classical fluids. I. thermodynamical properties of Lennard-Jones molecules," *Phys. Rev.*, vol. 159, no. 1, pp. 98 - 103, 1967.

[105] R. Clausius, "XVI. On a mechanical theorem applicable to heat," *Philos. Mag. Ser. 4*, vol. 40, no. 265, pp. 122 - 127, 1870.

[106] J. Li, "AtomEye: an efficient atomistic configuration viewer," *Model. Simul. Mater. Sci. Eng.*, vol. 11, no. 2, pp. 173 - 177, 2003.

[107] "Push-to-Pull Device." [online]: Available http://www.hysitron.com/products/options-upgrades/push-to-pull-device.

[108] W. S. Williams, "Transition metal carbides, nitrides, and borides for electronic applications," *JOM*, vol. 49, no. 3, pp. 38 - 42, 1997.

[109] W. S. Williams, "Influence of temperature, strain rate, surface condition, and composition on the plasticity of transition-metal carbide crystals," *J. Appl. Phys.*, vol. 35, no. 4, p. 1329, 1964.

[110] S.-R. Jian, T.-H. Sung, J. C. Huang, and J.-Y. Juang, "Deformation behaviors of InP pillars under uniaxial compression," *Appl. Phys. Lett.*, vol. 101, no. 15, p. 151905, 2012.

[111] R. H. J. Hannink, D. L. Kohlstedt, and M. J. Murray, "Slip system determination in cubic carbides by hardness anisotropy," *Proc. R. Soc. A Math. Phys. Eng. Sci.*, vol. 326, no. 1566, pp. 409 - 420, 1972.

[112] Z. Shan, J. Li, Y. Cheng, A. Minor, S. S. Asif, O. Warren, and E. Ma, "Plastic flow and failure resistance of metallic glass: insight from in situ compression of nanopillars," *Phys. Rev. B*, vol.77, no. 155419, pp.1 - 6, 2008.

[113] M. D. Uchic, P. A. Shade, and D. M. Dimiduk, "Plasticity of micrometer-scale single crystals in compression," *Annu. Rev. Mater. Res.*, vol. 39, no. 1, pp. 361 - 386, 2009.

[114] S. I. Rao, D. M. Dimiduk, T. A. Parthasarathy, M. D. Uchic, M. Tang, and C. Woodward, "Athermal mechanisms of size-dependent crystal flow gleaned from three-dimensional discrete dislocation simulations," *Acta Mater.*, vol. 56, no. 13, pp. 3245 - 3259, 2008.

[115] S.-H. Jhi, J. Ihm, S. G. Louie, and M. L. Cohen, "Electronic mechanism of hardness enhancement in transition-metal carbonitrides," *Nature*, vol. 399, no. 6732, pp. 132 - 134, 1999.

[116] D. G. Sangiovanni, V. Chirita, and L. Hultman, "Electronic mechanism for toughness enhancement in $Ti_xM_{1-x}N$ (M=Mo and W)," *Phys. Rev. B*, vol. 81, no. 10, p. 104107, 2010.

[117] K. Niihara, "Slip systems and plastic deformation of silicon carbide single crystals at high temperatures," *J. Less Common Met.*, vol. 65, no. 1, pp. 155 - 166, 1979.

[118] R. Rao, J. E. Bradby, S. Ruffell, and J. S. Williams, "Nanoindentation-induced phase transformation in crystalline silicon and relaxed amorphous silicon," *Microelectronics J.*, vol. 38, no. 6 - 7, pp. 722 - 726, 2007.

[119] T. Juliano, Y. Gogotsi, and V. Domnich, "Effect of indentation unloading conditions on phase transformation induced events in silicon," *J. Mater. Res.*, vol. 18, no. 05, pp. 1192 - 1201, 2011.

[120] P. Valentini, W. Gerberich, and T. Dumitrică, "Phase-transition plasticity response in uniaxially compressed silicon nanospheres," *Phys. Rev. Lett.*, vol. 99, no. 17, p. 175701, 2007.

[121] Y. B. Gerbig, S. J. Stranick, D. J. Morris, M. D. Vaudin, R. F. Cook, "Effect of crystallographic orientation on phase transformations during indentation of silicon," *J. Mater. Res.*, vol. 24, no. 03, pp. 1172 - 1183, 2011.

[122] R. S. Okojie, M. Xhang, P. Pirouz, S. P. Tumakha, G. Jessen, and L. J. Brillson, "4H-to 3C-SiC polytypic transformation during oxidation," *Mater. Sci. Forum*, vol. 389 - 393, pp. 451 - 454, 2002.

[123] C. Western, R. Unit, P. Pirouz, and J. W. Yang, "Polytypic transformations in SiC: the role of TEM," *Ultramicroscopy*, vol. 51, no. 1, pp. 189 - 214, 1993.

[124] J. W. Yang and P. Pirouz, "The $\alpha \rightarrow \beta$ polytypic transformation in high-temperature indented SiC," *J. Mater. Res.*, vol. 8, no. 11, pp. 2902 - 2907, 1993.

[125] T. H. Courtney, *Mechanical behavior of materials.* McGraw-Hill, 2000, p. 733.

[126] D. Lahiri, V. Singh, G. R. Rodrigues, T. M. H. Costa, M. R. Gallas, S. R. Bakshi, S. Seal, and A. Agarwal, "Ultrahigh-pressure consolidation and deformation of tantalum carbide at ambient and high temperatures," *Acta Mater.*, vol. 61, no. 11, pp. 4001 - 4009, 2013.

[127] D. J. Rowcliffe and W. J. Warren, "Structure and properties of tantalum carbide crystals," *J. Mater. Sci.*, vol. 5, no. 4, pp. 345 - 350, 1970.

[128] D. J. Rowcliffe and G. E. Hollox, "Hardness anisotropy, deformation mechanisms and brittle-to-ductile transition in carbide," *J. Mater. Sci.*, vol. 6, no. 10, pp. 1270 - 1276, 1971.

[129] B. Moser, K. Wasmer, L. Barbieri, and J. Michler, "Strength and fracture of Si micropillars: a new scanning electron microscopy-based micro-compression test," *J. Mat. Res.*, vol. 22, pp. 1004 - 1011, 2007.